Capillary interactions in wetting: rotation of particles at interfaces and removal of particles by drops

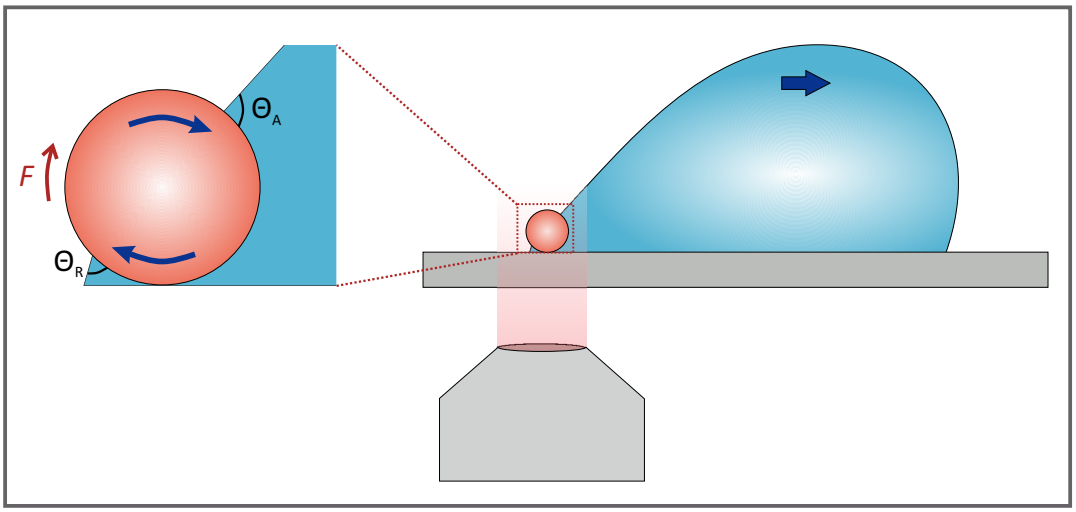

Dissertation
zur Erlangung des Grades
„Doktor der Naturwissenschaften“
am Fachbereich Physik, Mathematik und Informatik
der Johannes Gutenberg-Universität
in Mainz

Abhinav Naga

geboren in Réduit, Mauritius

Mainz, den 29 Mai 2021

Abstract

In this thesis, I have experimentally and theoretically investigated the mechanism by which a liquid drop removes a single solid particle from a surface.

To address this problem, I designed a method based on laser scanning confocal microscopy to image drop-particle collisions dynamically (speeds 10 to 10^4 $\mu m\,s^{-1}$) and to measure the horizontal force acting on the drop during these collisions. Water drops, glass particles and crosslinked polydimethylsiloxane surfaces were used in most of the experiments.

Two main collision outcomes were observed: either the particle collided with the drop and remained attached to the liquid-air interface (successful removal), or the particle entered and exited the drop (unsuccessful removal). The viscous force measured when the particle moved through the drop was negligible compared to the capillary force acting on the particle when it was attached to the liquid-air interface. Consequently, the dominant force that determines particle removal is the capillary force. A liquid-air interface will successfully remove a particle when the capillary force exceeds the resistive force that the particle has to overcome to move (roll/slide) on the surface.

To understand the difference between the forces acting on a rolling particle and a sliding particle, I theoretically modelled the capillary force for both cases. There are two main results. Firstly, a rolling particle enters a drop more easily than a non-rolling particle (up to 40% less force is required). Secondly, a particle experiences a resistive capillary torque when rolling at an interface. This torque significantly increases the rolling resistance of the particle.

The theoretical model for the resistive capillary torque is directly applicable in addressing broader questions on the motion of particles at interfaces and the mobility of moist granular matter. Moreover, the experimental method presented in this thesis can be applied to study a variety of problems in the field of wetting (and beyond), where the combination of microscopic imaging and friction force measurements is often insightful.

Contents

List of Figures

Chapter 1

Introduction

On a lotus leaf, water drops are highly mobile. They easily roll off, removing contaminants (e.g. dirt) that are present on the leaf. As a result, the leaf remains clean, even after being immersed in dirty water. The lotus leaf is an example of a self-cleaning surface [10, 81, 18, 85]. Self-cleaning surfaces are surfaces that can be cleaned by water drops, which may come from rain, dew, fog, or man-made sprays.

Over the past two decades, there has been an extensive amount of research on designing and applying self-cleaning coatings to various surfaces, such as solar panels and windows. Despite the substantial experimental evidence demonstrating that self-cleaning surfaces have an excellent ability to remain clean [75, 82, 6, 58, 49], the mechanism behind this observation remains elusive. There are several reasons for this knowledge gap. Visualising the removal of dirt by drops requires high-resolution microscopic imaging because dirt particles (henceforth called particles) are generally very small. Furthermore, it is difficult to draw general conclusions on particle removal because experimental observations tend to depend on the precise details (shape, size, type) of the particle, the surface, and the drop. Due to these challenges, most existing studies have only investigated surfaces that are heavily contaminated with particles. There is no experimental study on particle removal at a single-particle level. With heavily contaminated surfaces, the 'efficacy' of a self-cleaning surface can be determined by measuring the fraction of particles that are removed after the passage of a drop. However, the insights provided by such studies are insufficient to understand the mechanism of particle removal on a single-particle level.

In this thesis, I investigate the removal of single particles from surfaces by drops. A complete description of this problem requires knowledge of (1) how the drop interacts with the surface, (2) how the particle interacts with the drop, and (3) how the particle interacts with the surface. The interaction between a drop and a surface, and between a particle and a drop (1 and 2) are both problems that form part of a broader field of study called wetting, and in this thesis, I will focus predominantly on these two aspects.

In general, wetting is the study of how liquids interact with solids (or other immiscible liquids). Wetting includes the study of drops on solid surfaces as well as

particles at liquid-air interfaces. The region where a liquid-air interface meets a solid is particularly interesting because this region strongly influences dynamic properties, such as the mobility of the liquid relative to the solid surface and the force acting between the liquid and the solid. Wetting phenomena can be understood in terms of capillary forces, which correspond to the forces that act between a liquid and a solid. Capillary forces are due to cohesive forces between the liquid molecules and adhesive forces between the liquid and solid molecules. Since capillary forces are the key to explaining the removal of particles using drops, it is worth reviewing how the field of wetting evolved over the centuries and understanding why the term 'capillary forces' is used to describe the interaction between liquids and solids, even when there is no 'capillary' involved.

1.1 Historical overview

The earliest reports of wetting can be traced back to Leonardo da Vinci in the late fifteenth century.[1] Leonardo da Vinci observed the spontaneous rise of liquids in very thin tubes, called capillary tubes.[2] The observation of liquid rising seemed to contradict the common notion that liquids tend to their lowest possible position due to the pull of gravity. Most early studies sought to explain the cause of this contradiction. In the centuries following this observation, many highly influential scientists, including Issac Newton,[3] Albert Einstein [39], Robert Boyle [22] and Robert Hooke [61], explored the phenomenon of capillary rise. This historical focus on 'capillary force' justified the contemporary use of the term when describing the force between a liquid and a solid, despite there being no capillary involved in some cases.

During an era when concepts such as surface tension were unknown, explaining capillary rise proved challenging. In the mid-1600s Robert Boyle and Robert Hooke proposed various theories to explain capillary rise. Robert Boyle concluded that the curvature of the liquid meniscus in the tube is an important parameter in understanding this phenomenon. He based his conclusion on the observation that when a capillary tube is dipped into a water reservoir, the water meniscus has a convex shape and it rises up the tube. However, when a capillary tube is dipped into a mercury reservoir, the meniscus has a concave shape and it depresses below the level of mercury in the reservoir [22]. Robert Hooke hypothesised that capillary rise is due to reduced air pressure in small tubes [61]. He proposed that air cannot get inside very thin tubes. This would cause the air pressure inside the tube to be lower than the air pressure outside the tube. As a result, the difference in the air pressure would drive liquid up the tube. This idea was later refuted as the discovery of the existence and size of molecules demonstrated that molecules in air are much smaller

[1] This was reported by James Clerk Maxwell in [78].

[2] Capillary tubes have an inner radius of the order of the thickness of a hair.

[3] Issac Newton discussed capillary rise in Query 31 of his Opticks book, as mentioned in [88].

than even the thinnest capillary tubes, and thereby face no difficulty in getting inside the tubes.

In the early 1700s, Francis Hauskbee performed a series of systematic experiments on capillary rise both in thin tubes and between closely spaced glass plates [54, 55, 56]. He observed that the liquid rises to greater heights in thinner tubes and that the height to which the liquid rises does not differ when the tubes are in air under standard pressure or in a vacuum. Francis Hauksbee therefore established that the air pressure is not the cause of capillary rise. He hypothesised that adhesive forces between the liquid and walls of the tube are responsible. In 1719, James Jurin performed experiments to demonstrate that the height to which a given liquid rises in a capillary tube is inversely proportional to the diameter of the tube [67, 68]. James Jurin built on Francis Huaksbee's hypothesis, by adding that capillary rise depends both on the adhesive forces between the liquid and the tube walls, and on the cohesive forces within the liquid. Liquid rises up a capillary tube when the adhesive forces are stronger than the cohesive forces.

In 1751, Johann Andreas von Segner, introduced the notion of surface tension as an inherent property of a liquid.[4] Around fifty years later, Thomas Young [111] and Pierre Simon de Laplace [73] made significant progress by applying the concept of surface tension to explain a number of experimental observations, including capillary rise. Thomas Young considered the forces acting at a junction between a solid surface, a liquid and a vapour, and proposed that the (contact) angle between the liquid-vapour interface and the solid can be defined in terms of the liquid-vapour, liquid-solid and solid-vapour surface tensions (or interfacial tension). The relation between the contact angle and the three surface tensions is now widely known as Young's law. In principle, Young's law allows us to quantify the relative strength of adhesive and cohesive forces from the contact angle, which can be measured experimentally.

The analyses by both Thomas Young and Pierre Simon de Laplace were based on forces and pressures. In their time, concepts of energy were poorly understood. In the 1850s, Sadi Carnot, James Joule, Émile Clapeyron, William Thomson, Rudolf Clausius, and Hermann von Helmholtz developed the foundation of modern thermodynamics [91]. Subsequently, Athanase Dupré [37] and Willard Gibbs [50] were the first to apply these concepts to wetting. Problems that were previously solved in terms of forces were now formulated in terms of energies.

In parallel to developments in wetting, the field of fluid mechanics was also progressing rapidly. In the 18th century, Leonhard Euler constructed a theory to describe the flow of incompressible and frictionless (inviscid) fluids [62]. In 1821, Claude-Louis Navier introduced the notion of viscosity, which was a crucial factor in describing the behaviour of real liquids [62]. Throughout the 1840s, George Stokes built on the theory of Euler and Navier to describe the flow of viscous liquids and

[4] This was reported by James Clerk Maxwell in [78].

performed experiments to confirm his theory [97]. Today, the general equations of motion describing the flow of fluids are widely known as the Navier-Stokes equations, in honour of these two pioneers. By the mid-1800s, Jean Poiseuille, who was interested in modelling blood circulation in the body, provided an empirical equation to describe the flow rate of liquids in thin tubes. Poiseuille's empirical equation was later theoretically derived from the Navier-Stokes equations by Eduard Hagenbach [101]. In the early 1900s, Richard Lucas (1908) and Edward Washburn (1921) combined Poiseuille's equation with Young's law to model the kinetics of liquid rise in capillary tubes [76, 105].

In the 20th century, research in wetting diversified and fundamental work was often related to industrial applications to address questions such as: How to maximise the retention of pesticide sprays by leaves? How to maximise the amount of minerals that can be extracted by flotation? Consequently, it became increasingly important to account for effects that arise due to imperfections in real surfaces. Young's law is valid for perfectly homogeneous (ideal) solids. It predicts that the contact angle between a liquid and a solid takes a unique value. In the 1900s it became clear that this is generally not the case on real surfaces [1, 2, 9, 8, 34]. Instead, the contact angle lies within a finite range, between the so-called receding and advancing contact angles. The terms advancing (receding) contact angle is used because it corresponds to the contact angle that a liquid-air interface makes with a solid surface when it advances (recedes) on the surface. The difference between the advancing and the receding contact angles is termed contact angle hysteresis and is usually attributed to surface roughness, chemical contamination, inhomogeneities, or the presence of solutes in the liquid [33]. Contact angle hysteresis has many implications. In 1962, Furmidge, who was interested in quantifying how strongly pesticide sprays adhere to leaves, derived an expression relating contact angle hysteresis to the force required to move a drop on a solid surface [47].

In the mid-1900s, Wenzel (1936) [106] and Cassie and Baxter (1944) [27], who were interested in modelling the wetting resistance of textiles, derived models to demonstrate that the contact angle measured between liquids and solid surfaces can differ significantly deviate from the prediction obtained with Young's equation when the surface has a substantial degree of roughness. They modified Young's equation to incorporate the influence of surface roughness. The findings by Wenzel, Cassie and Baxter emphasised the relevance of the geometry of surfaces on their wetting properties. Roughness can significantly increase or decrease the apparent contact angle, depending on the chemical properties of the surface. An increase in the apparent contact angle results in a decrease in the contact area between drops and rough surfaces. A reduction in the contact area leads to a reduction in the capillary force between the drop and the solid. Therefore, chemically hydrophobic surfaces that have substantial roughness on the micro and nanoscale (such a the lotus leaf)

tend to be super water-repellent (or superhydrophobic). Surface roughness is a key factor in the design of man-made superhydrophobic surfaces.

The interaction of water with superhydrophobic surfaces has been studied intensively since the 1990s due to their exceptional ability to repel water and stay free of dirt [10]. Although most studies on superhydrophobicity are motivated by their self-cleaning properties, relatively few studies have systematically investigated the phenomenon. The removal of particles from surfaces by drops is a complex problem since it depends on the particle-drop, particle-surface and drop-surface interactions simultaneously. Numerous studies have reported that superhydrophobic surfaces make excellent self-cleaning surfaces [10, 18, 85]. It has been proposed that particle removal is possible when the capillary force between a drop and a dirt particle exceeds the adhesion force between the particle and the surface [75, 58]. While this is generally true, it overlooks several details. In particular, the following questions are still outstanding: What is the maximum capillary force that a drop can exert on a particle to remove it from a surface? What are the consequences when a particle rolls on the surface as it is removed? To answer such questions, it is important to consider particle removal on a single particle level. In this thesis, I derive analytical models to describe the forces acting on particles rolling at a liquid-air interface and experimentally investigate the removal of single particles from surfaces by drops.

1.2 Overview of thesis

In the rest of this chapter, I will introduce fundamental concepts that will be relevant to this thesis.

In chapter 2, I will describe two experimental methods that I have designed and implemented. First, I will describe how forces can be directly measured using a flexible metal blade as a force sensor on a laser scanning confocal microscope. Then, I will describe a method to measure the change in the surface tension of drops as they accumulate contaminants from a surface. These methods have been published in *Soft Matter* [80].

In chapter 3, I will investigate the behaviour of water drops on silicone (polydimethylsiloxane, PDMS) surfaces. I will show that when water drops are placed in contact with a PDMS surface, uncrosslinked PDMS chains migrate from the surface onto the drop. These uncrosslinked chains influence the effective surface tension of the drop and its contact angle with the surface.

In chapter 4, I will derive a theoretical framework to model the capillary forces acting on a particle when it rotates at an interface. Rotation at an interface has consequences: (1) a rotating particle experiences a resistive capillary torque, and (2)

the force required to detach a particle from an interface is lower when the particle rotates.

In chapter 5, I will apply the experimental methods from chapter 2 and the results from chapters 3 and 4 to investigate how drops remove single micrometre-sized particles from PDMS surfaces. I will address the following questions: How does particle removal look like on a microscopic scale? Which forces are involved during particle removal? How can we increase the chances of removing a particle from a surface using water drops?

1.2.1 Publications associated with this thesis

Some of the work presented in this thesis have led to publications in peer-reviewed journals.
The methods described in chapter 2 and some of the results presented in the first part of chapter 3 and chapter 5 have been published in:

- **A. Naga**, A. Kaltbeitzel, W. S. Y. Wong, L. Hauer, H.-J. Butt, and D. Vollmer, How a Water Drop Removes a Particle from a Hydrophobic Surface, *Soft Matter* 17, 1746 (2021).

Some of the results from the second part of chapter 3 have been published in:

- W. S. Y. Wong, L. Hauer, **A. Naga**, A. Kaltbeitzel, P. Baumli, R. Berger, M. D'Acunzi, D. Vollmer, and H.-J. Butt, Adaptive Wetting of Polydimethylsiloxane, *Langmuir* 36, 7236 (2020).

The first part of chapter 4 has been accepted for publication:

- **A. Naga**, D. Vollmer, and H.-J. Butt, Capillary torque on a particle rotating at an interface, *Accepted in Langmuir.*

The second part of chapter 4 is being prepared for publication:

- **A. Naga**, H.-J. Butt, and Doris Vollmer, Detachment force of a particle rotating at a liquid-fluid interface, *In preparation.*

1.3 Interfaces and surfaces

An *interface* is a boundary where two different phases meet. A phase is a region in space where all physical properties (density, refractive index, chemical composition) of a material are essentially uniform. At an interface, the phases can be two immiscible liquids, two different solids, a liquid and a gas, or a solid and a gas. Gas-gas interfaces do not exist because gases mix. A raindrop in air has only one interface, namely the

air-water interface. In contrast, a drop resting on a solid surface has three interfaces: an air-water interface, a solid-water interface and a solid-air interface. The term *surface* is a subset of *interface*, where one of the phases is a gas (or a vacuum) [26].

Wetting is the study of all phenomena where three distinct phases meet. The three phases can be (1) a liquid, a gas and a solid, for example a rain drop on a window, (2) two immiscible liquids and a solid, for example a water drop on a surface submerged in oil, or (3) two immiscible liquids and a gas, for example a water drop on the surface of oil.

Wetting phenomena are encountered in a variety of settings, from morning dew on plants and spider webs to bubbles in sparkling wine. Wetting is relevant in many industrial applications, such as inkjet printing, de-inking of recycled paper, waterproofing of outdoor garments and during the transport of (moist) granular matter.

1.4 Surface tension

Surface tension is one of the most important physical properties used to characterise wetting. Young (1805) formulated his law based on surface tensions. The surface tension, γ, of a liquid is a measure of the cohesive forces between the liquid molecules.

Surface tension manifests in numerous ways. Liquids rise in capillary tubes. A carefully placed metal paper clip remains at the surface of water even though metal has a higher density than water. Sand grains adhere to one another when humid. Insects, such as water striders rely on surface tension to walk on the surface of water.

Formally, surface tension is defined following either a mechanical approach or a thermodynamic approach.

1.4.1 Mechanical definition

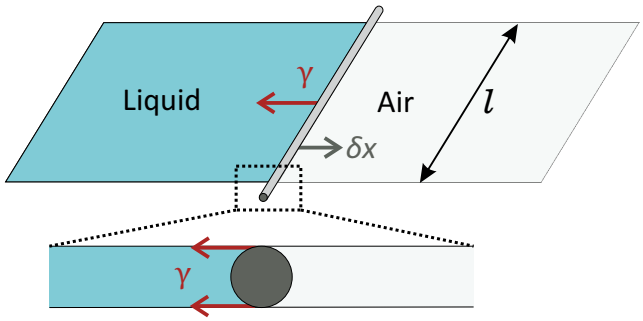

Figure 1.1: A rod separates a liquid film from a dry region. Surface tension, γ, pulls the rod towards the liquid film. To extend the film by an amount δx, work needs to be done against surface tension.

Consider a liquid film enclosed by a rectangular wire frame with a mobile rod of length l separating the liquid film from air, as shown in figure 1.1. The work, δW, required to pull the rod by an amount δx is

$$\delta W = F\ \delta x = \gamma l_{\mathrm{CL}}\ \delta x \tag{1.1}$$

Here, F is the applied force and $l_{\mathrm{CL}} = 2l$ (l is defined in figure 1.1) is the total length of the liquid-air interface in contact with the rod. The factor of two because the liquid film has a finite thickness and therefore contact between the film and the rod is a rectangle with a perimeter of $\approx 2l$. Based on this picture, surface tension is the force per unit contact length pulling the rod towards the liquid film,

$$\frac{F}{l_{\mathrm{CL}}} = \gamma. \tag{1.2}$$

Alternatively, we can think of surface tension as the work required to increase the surface area of the liquid by one unit. By pulling the rod by δx, we increase the surface area of the liquid by $\delta A = 2l\delta x$, where the factor of 2 is because the liquid has two sides, top and bottom. Therefore, the work done per unit area is

$$\frac{\delta W}{\delta A} = \gamma. \tag{1.3}$$

1.4.2 Thermodynamic definition

The Helmholtz free energy of a two-phase system separated by a planar interface is

$$dF = S\ dT - P\ dV + \sum \mu_i N_i + \gamma\ dA, \tag{1.4}$$

where S is the entropy, T is the absolute temperature, P is the pressure, V is the volume, μ_i is the chemical potential of molecules of type i, N_i is the number of molecules of type i, and A is the interfacial area. In closed system ($dN_i = 0$) at constant temperature and volume,

$$\left(\frac{\partial F}{\partial A}\right)_{T,V,N_i} = \gamma. \tag{1.5}$$

Therefore, from a thermodynamic perspective, surface tension is the change in the Helmholtz free energy per surface area at constant temperature, volume, and total amounts of all components.

1.4.3 Microscopic origin

Molecules are attracted to each other by intermolecular forces. Due to attractive intermolecular forces, it is energetically favourable for molecules to be surrounded by other molecules. Compared to molecules in the bulk, molecules at an interface share fewer bonds with other molecules (figure 1.2). Therefore, it is energetically

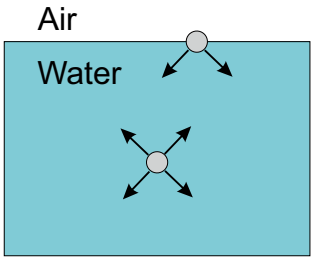

Figure 1.2: Molecules at the surface form fewer bonds than molecules in the bulk. This gives rise to surface tension.

unfavourable for molecules to be at the surface. Surface tension is due to the excess energy per area associated with molecules at the surface.

The concepts underlying surface tension can also be applied to liquid-liquid interfaces, where adhesive forces and cohesive forces determine the 'tension' between the two phases. In the context of liquid-liquid interfaces, the term *interfacial tension* is generally used instead of surface tension.

1.4.4 Laplace pressure

Surface tension leads to a pressure difference between the two sides of a curved interface. In equilibrium, the pressure difference across the interface is related to its curvature according to Laplace's equation,

$$\Delta P = \gamma \left(\frac{1}{R_1} + \frac{1}{R_2} \right). \tag{1.6}$$

where R_1 and R_2 are the principal radii of curvature of the interface (figure 1.3). ΔP is called the Laplace pressure or capillary pressure. $\Delta P > 0$ for convex surfaces, such as the surface of drops. $\Delta P < 0$ for concave surfaces, such as the surface of a water meniscus inside a capillary tube.

Derivation of the Laplace equation Consider an infinitesimal part of a curved interface (figure 1.3). Surface tension exerts a force $\gamma \delta l$ on an element of length δl at point B. The vertical projection of this force is

$$\gamma \delta l \sin \phi \approx \gamma \phi \delta l \approx \gamma \frac{d}{R_1}. \tag{1.7}$$

In the first step, $\sin \phi \approx \phi$ is because we are considering an infinitesimal region and therefore ϕ is small. The above expression also corresponds to the vertical force at point A. Similarly, the vertical projection of the force at points C and D (which lie in a plane orthogonal to the plane containing A and B) is

$$\gamma \delta l \frac{d}{R_2}. \tag{1.8}$$

Therefore, the total vertical force at points A, B, C and D is

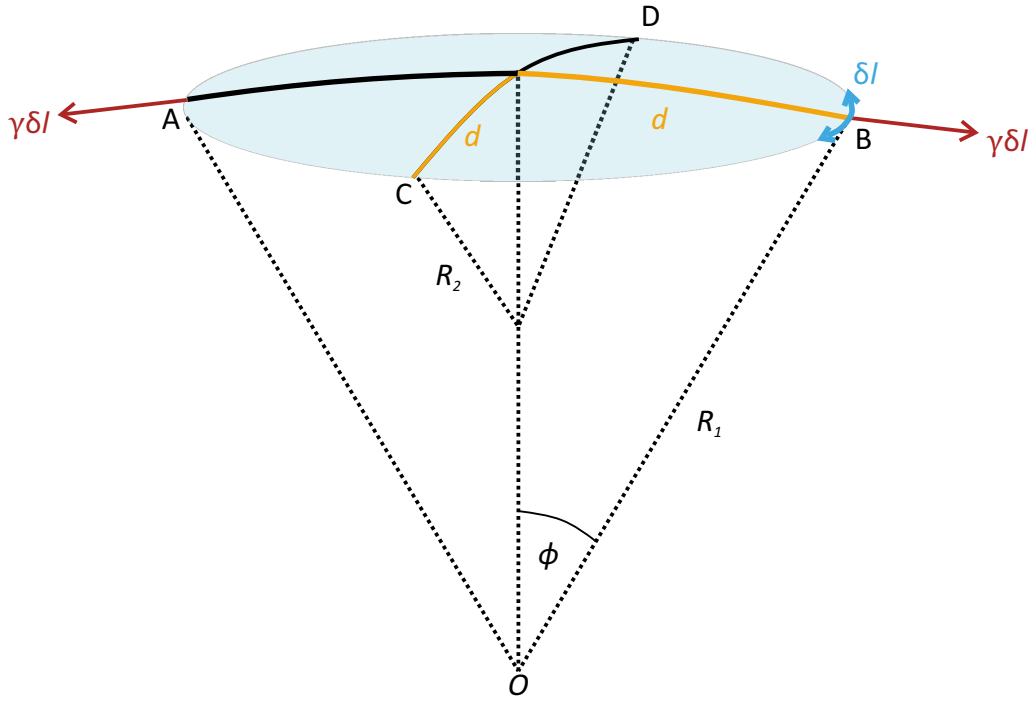

Figure 1.3: Sketch for the derivation of the Laplace equation (equation 1.6). The shaded region (blue) shows a curved liquid-fluid interface with principal radii of curvature R_1 and R_2.

$$2d\gamma\delta l\left(\frac{1}{R_1}+\frac{1}{R_2}\right). \tag{1.9}$$

This expression is independent of the choice of AB and CD and therefore can be integrated around the segment $ABCD$ to give the total vertical force

$$\pi d^2\gamma\left(\frac{1}{R_1}+\frac{1}{R_2}\right). \tag{1.10}$$

In equilibrium, this downward force is balanced by an equal upward force, which is caused by an increased pressure on the lower side of the interface. The pressure difference acts on an area πd^2, causing an upwards force $\Delta P\pi d^2$. Equating the two forces leads to equation 1.6, which is valid everywhere along the interface.

The forces arising due to surface tension are termed *capillary forces*. Capillary forces includes (1) the contribution due the direct action of surface tension at the contact between a liquid-fluid interface and a solid, and (2) the contribution due to Laplace pressure.

1.4.5 Methods to measure surface tension

There are several methods for measuring the surface tension of liquids [3]. Here, I introduce two commonly used methods: the Wilhelmy plate method and the pendant drop method.

The Wilhelmy plate method is based on the definition that surface tension is the force per unit length (equation 1.2). A thin plate is dipped into the liquid. The plate is usually made of a material that is completely wetted by the liquid (e.g. roughened platinum or filter paper) such that the surface tension points vertically downwards at the three-phase contact line. The force acting on the plate is measured with a force sensor. After subtracting the gravitational force due to the rise of the liquid meniscus, the measured force is equal to $2l\gamma$, where l is the length of the plate. Effects due to the finite thickness of the plate are assumed to be negligible since it is much smaller than its length. The same principle can also be applied to measure surface tensions using other geometries, such as rings or rods.

The pendant drop method will be introduced in detail in chapter 2. In essence, a drop is suspended from a needle. The drop size is large enough such deformations due to gravity are significant. The two factors determining the shape of the drop are surface tension and gravity. The surface tension is obtained by fitting the Laplace equation (equation 1.6) to the drop contour.

1.5 Spreading parameter

When a drop of soapy water is placed on a glass surface, it spreads. However, when a drop of water is placed on a non-stick frying pan, it takes the shape of a spherical cap. This difference can be understood in terms of the spreading parameter, S, which is defined as

$$S = \gamma_{\mathrm{SA}} - (\gamma + \gamma_{\mathrm{SL}}), \tag{1.11}$$

where γ_{SA}, γ and γ_{SL} are the solid-air, liquid-air and solid-liquid surface tensions, respectively. If $S > 0$, the liquid completely spreads on the solid to form a film, whereas if $S < 0$, it makes a finite angle with the solid surface. This concept can also be applied to determine whether a liquid will spread onto the surface of another immiscible liquid. Drops of oil with a positive spreading coefficient with respect to water completely spread on the surface of water. Oil drops with a negative spreading coefficient do not completely spread.

1.6 Static contact angle

The equilibrium angle which a liquid makes with a solid surface is termed the *contact angle*, Θ (figure 1.4). The region where the liquid-air interface meets the solid is termed the *three-phase contact line*.

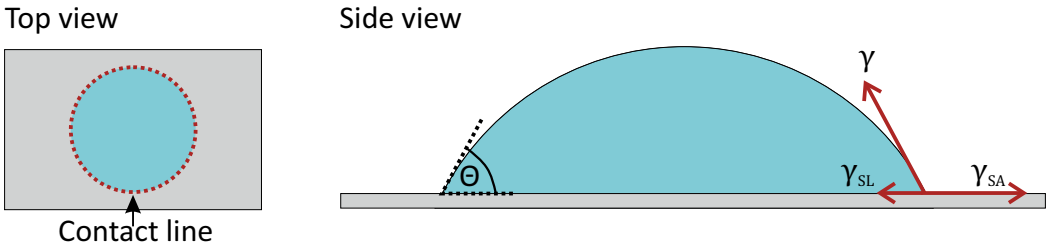

Figure 1.4: Drop on a flat surface. The three-phase contact line is drawn in red (dotted) in the top view schematic. The contact angle, Θ, is sketched in the side view schematic. The forces acting at the three-phase contact line are drawn (red arrows).

1.6.1 Flat surfaces

On smooth, flat and homogeneous surfaces, Θ can be expressed in terms of the liquid-air, solid-liquid and solid-air surface tensions by considering the forces (per unit length) acting parallel to the surface at the three-phase contact line:

$$f_{\parallel} = \gamma \cos\Theta + \gamma_{\mathrm{SL}} - \gamma_{\mathrm{SA}}, \tag{1.12}$$

where γ_{SA}, γ_{SL} and γ are the solid-air, solid-liquid and liquid-air surface tensions, respectively. In equilibrium, $f_{\parallel} = 0$, leading to Young's equation [111]:

$$\cos\Theta = \frac{\gamma_{\mathrm{SA}} - \gamma_{\mathrm{SL}}}{\gamma}. \tag{1.13}$$

The contact angle is a useful parameter to characterise the wettability of surfaces by liquids. When $\gamma_{\mathrm{SA}} > \gamma_{\mathrm{SL}}$, is it is favourable for the liquid to wet the surface and $\Theta < 90°$. When $\gamma_{\mathrm{SA}} < \gamma_{\mathrm{SL}}$, it is unfavourable for the liquid to wet the surface and $\Theta > 90°$. Surfaces which form a contact angle less than 90° with water are termed *hydrophilic* whereas surfaces which have $\Theta > 90°$ with water are termed *hydrophobic*.

Young's law only considers the horizontal force components. The vertical component of surface tension, $\gamma \sin\Theta$, acts upwards at the three-phase contact line. On soft solids, such as rubber, this causes a visible deformation, whereas on stiff solids, such as glass, the deformation is negligible.

1.6.2 Rough surfaces

1.6.2.1 Superhydrophobic surfaces

The maximum static contact angle of water on the most hydrophobic flat surface is around 120° (on fluorinated surfaces). To attain higher contact angles, surfaces need to be both chemically hydrophobic and have a significant degree of roughness. This combination can produce very high contact angles, up to almost 180°. Surfaces with contact angles greater than 150°, and high water mobility, are called superhydrophobic surfaces. A few examples of natural superhydrophobic surfaces are lotus leaves, duck

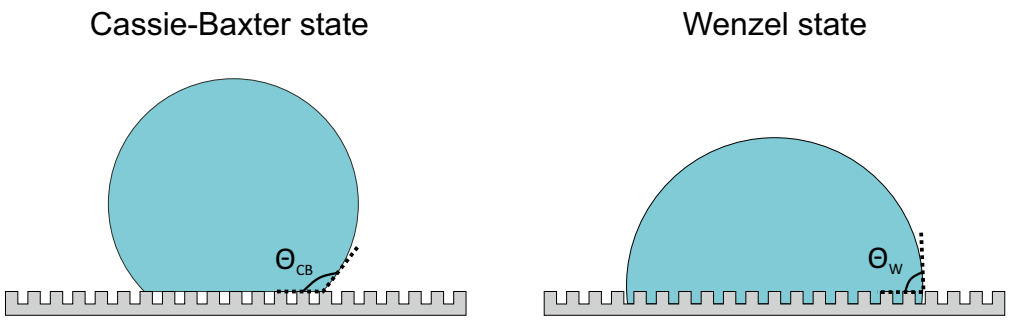

Figure 1.5: Drops on rough surfaces. The left image shows a drop in the Cassie-Baxter state. Air gaps are present underneath the drop. In the right image, the drop is in the Wenzel state and there are no air gaps underneath the drop.

feathers, cabbage leaves and broccoli. All these surfaces have a significant degree of nano and micro-scale roughness.

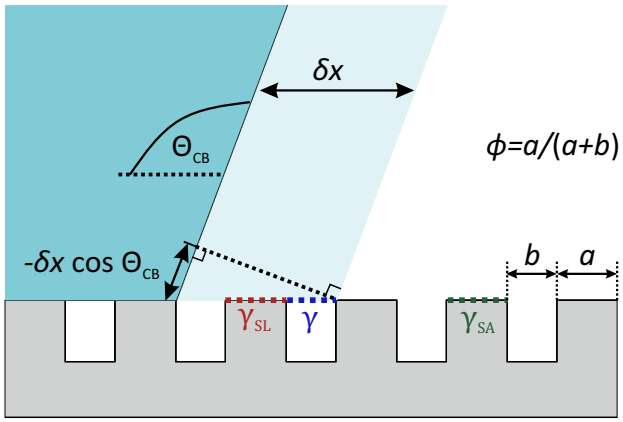

Figure 1.6: A liquid in the Cassie-Baxter state advancing by an infinitesimal amount δx.

Cassie-Baxter state When a water drop is placed on a superhydrophobic surface, there is often very little direct contact with the solid due to the presence of air gaps between the solid features. When air gaps are present beneath the drop, the drop is said to be in the *Cassie-Baxter state* [27] (figure 1.5). The macroscopic contact angle of a drop in the Cassie-Baxter state can be derived by considering the change in surface energy, δE, (per unit length of the three-phase contact line) required to move an air-water interface on a rough surface by an infinitesimal amount δx:

$$\delta E = \phi(\gamma_{\mathrm{SL}} - \gamma_{\mathrm{SA}})\ \delta x + (1-\phi)\gamma\ \delta x + \gamma \cos\Theta_{\mathrm{CB}}\ \delta x, \tag{1.14}$$

where ϕ is the area fraction of the solid that is in contact with water, $(1-\phi)$ is the area fraction occupied by the air gaps and the surface tensions have the same meaning as in the previous section. Θ_{CB} is the contact angle in the Cassie-Baxter state. Assuming that the contact line can move freely such that the system can always reach equilibrium, $\delta E = 0$ and therefore

$$\begin{aligned} \phi(\gamma_{\mathrm{SL}} - \gamma_{\mathrm{SA}}) + (1-\phi)\gamma + \gamma\cos\Theta_{\mathrm{CB}} &= 0 \\ \phi\gamma\cos\Theta + (1-\phi)\gamma + \gamma\cos\Theta_{\mathrm{CB}} &= 0 \\ \implies \cos\Theta_{\mathrm{CB}} &= (1+\cos\Theta)\phi - 1. \end{aligned} \tag{1.15}$$

In the above equation, $\gamma_{\mathrm{SA}} - \gamma_{\mathrm{SL}}$ was replaced by $\gamma\cos\Theta$ (equation 1.13), where Θ is the Young's contact angle on a flat surface made of the same material as the rough surface.

The Cassie-Baxter state is usually only a meta-stable state. As water drops evaporate on superhydrophobic surfaces, the pressure difference (Laplace pressure) between the water and the air gaps increase. Furthermore, water vapour condenses into the air gaps. Both these effects lead to the drop collapsing into the gaps. The resulting configuration is called the *Wenzel state* [106].

Wenzel state The contact angle of a drop in the Wenzel state can be obtained by considering the change in surface energy, δE, when the three-phase contact line advances by an infinitesimal distance, δx:

$$\delta E = r(\gamma_{\mathrm{SL}} - \gamma_{\mathrm{SA}})\ \delta x + \gamma\cos\Theta_{\mathrm{W}}\ \delta x, \tag{1.16}$$

where Θ_{W} is the contact angle in the Wenzel state. Assuming that the three-phase contact line can move freely such that equilibrium can always be reached, $\delta E = 0$. This leads to

$$\cos\Theta_{\mathrm{W}} = r\cos\Theta, \tag{1.17}$$

where Θ is the Young's contact angle on a flat surface made of the same material as the rough surface. By definition, $r > 1$ on rough surfaces. Therefore, $|r\cos\Theta| > |\cos\Theta|$. Since the sign of $\cos\Theta$ changes at $\Theta = 90°$, the two cases have to be considered separately. If the surface is inherently hydrophilic (Young's contact angle $\Theta < 90°$), the Wenzel contact angle will be even lower ($\Theta_{\mathrm{W}} < \Theta$) and therefore the surface will appear more hydrophilic. In contrast, if $\Theta > 90°$, the Wenzel contact angle will be higher than the Young's contact angle ($\Theta_{\mathrm{W}} > \Theta$) and the surface will appear more hydrophobic. Hence, the Wenzel state amplifies the degree of hydrophilicity or hydrophobicity. Equation 1.17 provides real solutions as long as $|r\cos\Theta| \leq 1$, otherwise it is not valid.

1.6.2.2 Liquid-infused surfaces

One way to improve the stability of the Cassie-Baxter state is to fill the air gaps with a lubricant that is immiscible with the drop [71, 108, 32]. This type of surface is called

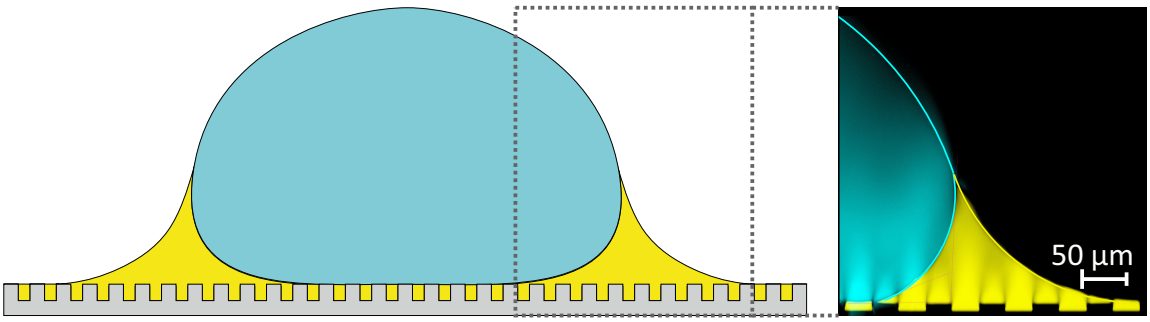

Figure 1.7: The left image shows a schematic of a drop on a liquid-infused surface. The lubricant rises around the drop to form a wetting ridge. The right image (adapted from reference [11]) was taken with laser scanning confocal microscopy. The interfaces have been drawn for clarity.

a liquid-infused surface.[5] Having a lubricant instead of air leads to a more stable Cassie-Baxter state since it reduces the condensation of water in between the gaps and reduces the Laplace pressure between the drop and the fluid gaps. A reduction in Laplace pressure is because the interfacial tension between water and lubricants is generally less than the air-water interfacial tension. Furthermore, since liquids are incompressible and more viscous than air, it is more difficult to displace a liquid lubricant than air.

While liquid-infused surfaces offer a more stable Cassie-Baxter state, they suffer from a reduction in drop mobility. Drops on liquid-infused surfaces are surrounded by a lubricant meniscus, called the *wetting ridge* (figure 1.7). A wetting ridge arises so that the lubricant-air, lubricant-drop and drop-air surface tensions balance at the lubricant-drop-air contact line. The wetting ridge causes drops to experience a significantly higher viscous dissipation on liquid-infused surfaces than on superhydrophobic surfaces.

1.7 Contact angle hysteresis

Young's equation (equation 1.13) is only valid for perfectly smooth and homogeneous surfaces. Practically, this is never the case. Even the cleanest surfaces have physical or chemical heterogeneities.

Consequently, drops on real surfaces exhibit static contact angles that lie in a finite range, $\Theta_R < \Theta < \Theta_A$, rather than displaying a single contact angle [42, 21, 23]. The range of possible static contact angles is called *contact angle hysteresis*, $\Delta\Theta = \Theta_A - \Theta_R$.

Θ_A and Θ_R are called the advancing and receding contact angles, respectively. When a drop quasi-statically moves on a surface, the contact angles at the front and

[5] In the literature, liquid-infused surfaces are also referred to as hemi-solids, slippery liquid-infused porous surfaces (SLIPS), or lubricant infused structured surfaces (LubISS).

rear sides are equal to Θ_A and Θ_R, respectively (figure 1.8).

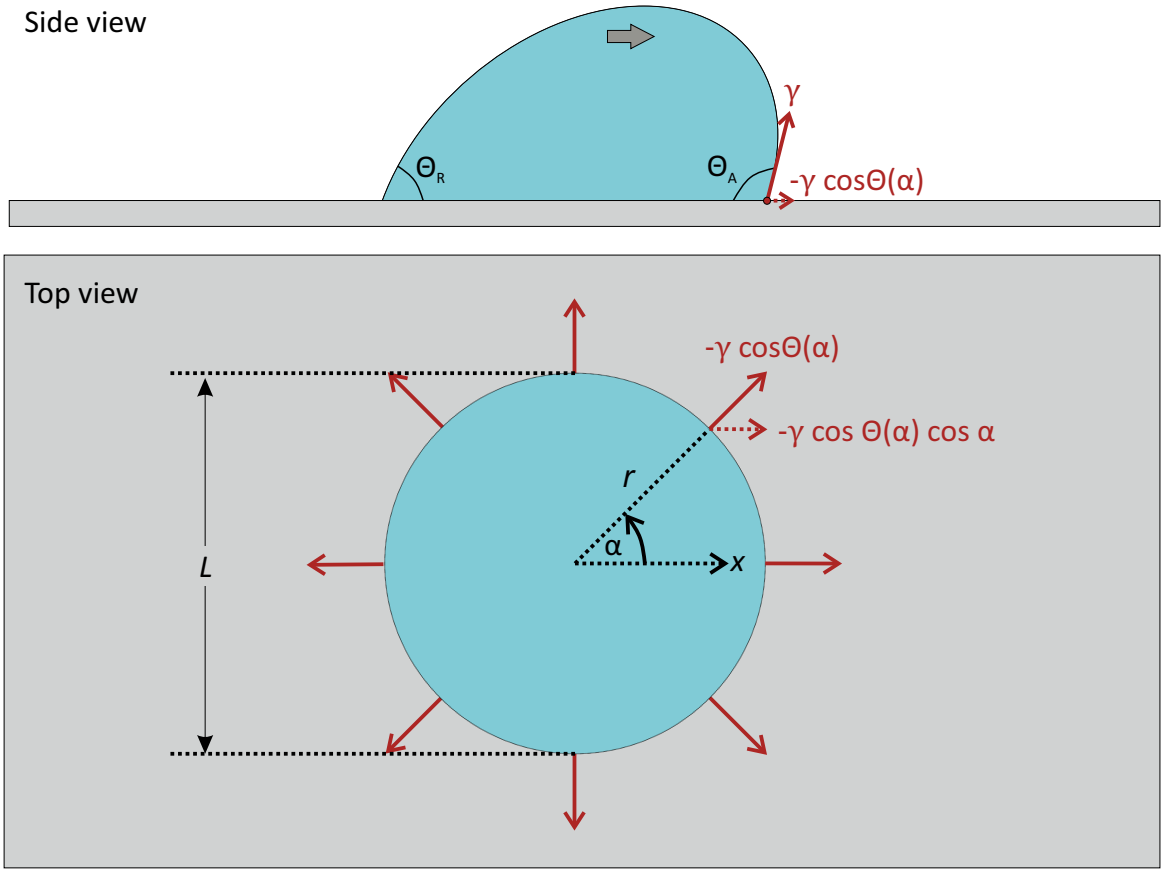

Figure 1.8: A moving drop has a contact angle equal to the advancing contact angle, Θ_A, at the front side and a contact angle equal to the receding contact angle, Θ_R, at the rear side.

Contact angle hysteresis has several consequences. It results in friction between drops and surfaces [86, 102, 48]. If real surfaces had a uniquely defined contact angle, drops would experience no friction when moving slowly (here slowly means negligible viscous drag). However, this is not the case due to contact angle hysteresis.

In chapter 4, I will derive a theoretical framework to model the consequences of contact angle hysteresis on the rotation of particles at a liquid-fluid interface.

1.7.1 Physical origin

When a liquid-air interface moves over a surface defect (physical or chemical heterogeneity) that has a different wettability to the rest of the surface, the three-phase contact line has to readjust. For example, when a receding air-water interface moves over a defect that is more hydrophilic than the rest of the surface, the three-phase contact line gets locally pinned to the defect. To overcome the defect, the interface has to deform, causing a decrease in the contact angle. If the defect exerts a pinning force f per unit length of the three-phase contact line, then

to de-pin, the contact angle has to deviate from the equilibrium contact angle, such that

$$\gamma(\cos\Theta_{\mathrm{R}} - \cos\Theta) = f, \tag{1.18}$$

where Θ is the equilibrium contact angle (without the defect), and Θ_{R} is the contact angle that needs to be reached to detach the three-phase contact line from the defect.

1.7.2 Relation to drop friction

The friction force between a drop and a surface is given by the component of the capillary force acting opposite to the direction of motion of the drop. The integral of the horizontal component of the capillary force around the three-phase contact line is

$$\begin{aligned} F_{\mathrm{drop}} &= \oint \boldsymbol{\gamma} \cdot \hat{\boldsymbol{x}}\ r(\alpha)\ d\alpha \\ &= -\int_0^{2\pi} \gamma \cos\Theta(\alpha) \cos\alpha\ r(\alpha)\ d\alpha, \end{aligned} \tag{1.19}$$

where $r(\alpha)$ is the radial distance between the centre of the contact area and the three-phase contact line at an azimuthal angle α (figure 1.8). Only the $\cos\alpha$ component of the surface tension is included in the integral because the $\sin\alpha$ components cancel due to symmetry about the axis of motion. Assuming a circular contact line with a contact angle of Θ_{A} on the front half and a contact angle of Θ_{R} on the rear half, the integral evaluates to [47, 38, 107, 83, 43, 44, 41, 86]

$$\begin{aligned} F_{\mathrm{drop}} &= -\gamma r \left(\int_{-\frac{\pi}{2}}^{\frac{\pi}{2}} \cos\Theta_{\mathrm{A}} \cos\alpha\ d\alpha + \int_{\frac{\pi}{2}}^{\frac{3\pi}{2}} \cos\Theta_{\mathrm{R}} \cos\alpha\ d\alpha \right) \\ &= 2\gamma r \left(\cos\Theta_{\mathrm{R}} - \cos\Theta_{\mathrm{A}}\right) = \gamma L \left(\cos\Theta_{\mathrm{R}} - \cos\Theta_{\mathrm{A}}\right), \end{aligned} \tag{1.20}$$

where $L = 2r$ is the contact line diameter, γ is the surface tension of the liquid, and Θ_{R} and Θ_{A} are the receding and advancing contact angles at the rear and front sides of the drop, respectively.

In general, more complex expressions can be used to describe $\Theta(\alpha)$. By measuring the contact angle around a drop at its onset of motion, ElSherbini and Jacobi (2006) showed that $\Theta(\alpha)$ follows a cubic polynomial in α. Integrating equation 1.19 with a cubic polynomial to describe $\Theta(\alpha)$ gives

$$F_{\mathrm{drop}} = k\gamma L(\cos\Theta_{\mathrm{R}} - \cos\Theta_{\mathrm{A}}), \tag{1.21}$$

where $k = 48\pi^3 \approx 0.75$ is a geometrical factor. Equations 1.21 and 1.20 are similar, except for the different pre-factors.

Equation 1.21 implies that the drops will only start to move relative to the surface when the applied force is larger than the force given by equation 1.21. The greater the contact angle hysteresis, the greater the drop friction.

1.8 Particles at interfaces

So far, I have applied general concepts such as surface tension, contact angle and contact angle hysteresis in the context of drops on surfaces. In this section, I apply the same concepts to a related problem with a different geometry, namely that of a particle at a liquid-fluid interface.[6] Particles adsorbed at interfaces are relevant in many applications including foods, pharmaceuticals, cosmetics, and minerals [28, 29, 14]. For example, in mineral processing, froth flotation is used to selectively extract valuable hydrophobic particles from hydrophilic gangue.

1.8.1 Detachment force

The strength with which a particle is attached to an interface is characterised by the detachment force. The detachment force is the force required to separate the particle from the interface. This can be done in two ways. In the case of a particle at a liquid-air interface, we can either pull the particle away from the water phase or push it into the water phase until it detaches from the interface.

When an ideal (perfectly smooth and homogeneous) particle is pulled normal to the interface, the contact angle remains constant (given by equation 1.13) while the three-phase contact line slides along the particle. During this process, the capillary force varies according to

$$\begin{aligned} F &= -\int_0^{2\pi} \gamma \sin(\phi - \Theta)\ R \sin\phi\ d\alpha \\ &= -2\pi R\gamma \sin(\phi - \Theta)\sin\phi, \end{aligned} \tag{1.22}$$

where R is the radius if the particle, Θ is the contact angle, γ is the interfacial tension and ϕ is defined in figure 1.9. The force has a maximum when

$$\begin{aligned} \frac{dF}{d\phi} &= -2\pi R\gamma \left[\cos(\phi - \Theta)\sin\phi + \sin(\phi - \Theta)\cos\phi\right] = 0 \\ \implies \phi &= \frac{\pi + \Theta}{2} \text{ or } \frac{\Theta}{2}. \end{aligned} \tag{1.23}$$

[6] The second fluid can either be a gas or another immiscible liquid.

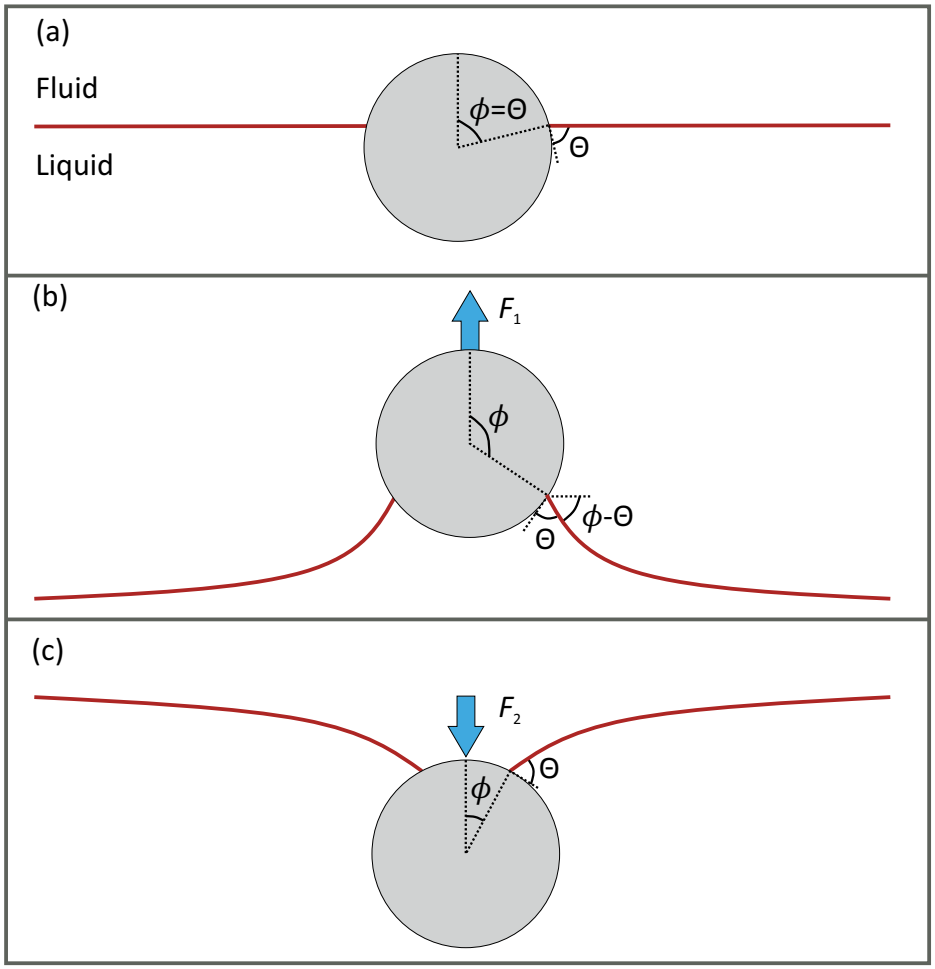

Figure 1.9: Detaching a particle from an interface. (a) Particle in equilibrium at a liquid-fluid interface. (b) Detaching the particle by pulling it upwards. (c) Detaching the particle by pushing it downwards into the liquid.

The first solution corresponds to a downwards capillary force. Therefore, the force required to overcome this force and detach the particle (upwards) away from the lower phase [figure 1.9 (b)] is

$$F_1 = 2\pi\gamma R \cos^2 \frac{\Theta}{2}, \tag{1.24}$$

This expression was first derived by Scheludko and Nikolov (1975) [95].

The second solution corresponds to the maximum upwards capillary force. Therefore, the force required detach the particle away from the upper phase [i.e. to push it into the lower phase, figure 1.9 (c)] is

$$F_2 = 2\pi\gamma R \sin^2 \frac{\Theta}{2}. \tag{1.25}$$

To derive equations 1.24 and 1.25 we have assumed that the contact line can move freely over the particle's surface. In reality, contact angle hysteresis has to be taken into account.

When the particle is pulled away from the liquid, the liquid-air interface recedes and the contact angle is given by the receding contact angle. Therefore, Θ has to be replaced by Θ_R and the expression becomes [93]:

$$F^{\text{pull}} = 2\pi\gamma R\cos^2\frac{\Theta_R}{2}. \tag{1.26}$$

Alternatively, when the particle is detached from the interface by pushing it into the liquid, the detachment force is given by [4]:

$$F^{\text{push}} = 2\pi\gamma R\sin^2\frac{\Theta_A}{2}. \tag{1.27}$$

Here, the advancing angle is used because the liquid-air interface advances on the particle as it enters the liquid.

1.9 Surface tension vs gravity

In the above sections, the influence of gravity has been ignored. In this section, I discuss when this is a valid assumption.

1.9.1 Shape of liquid surface

Consider a drop with a contact angle of around 90° on a solid surface. When the drop is small, it takes the shape of a spherical cap (figure 1.10). However, as more liquid is injected into the drop, it starts to deviate from a spherical cap until it eventually becomes a puddle. The transition from spherical cap to puddle is due to a transition from the drop shape being dominated by surface tension to it being dominated by gravity.

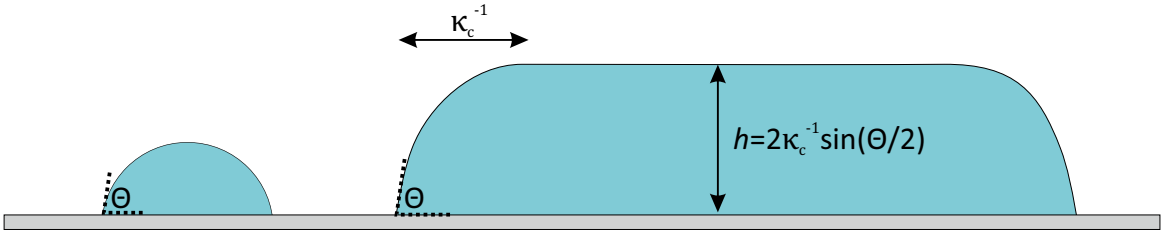

Figure 1.10: Left: Drops of radius much less than the capillary length, κ^{-1}, take the shape of spherical caps. Right: Above the capillary length, the contact angle Θ does not change but the drops flatten in the middle.

The length scale below which the Laplace pressure (surface tension) dominates the hydrostatic pressure (gravity) is referred to as the capillary length, κ_c^{-1}.[7] The

[7]From a historical point of view, the shape of interfaces was defined mathematically in terms of the curvature, κ. Since lengths can be directly measured and are easier to conceptualise, it is now more common to define a corresponding length scale by taking the reciprocal of the curvature.

Laplace pressure is proportional to γ/R (γ: surface tension of the drop, R: radius of the drop), whereas the hydrostatic pressure is proportional to $\rho g R$, where ρ is the density of the liquid and g is the gravitational acceleration.[8] The Laplace and hydrostatic pressures are equal when

$$R = \kappa_c^{-1} = \sqrt{\frac{\gamma}{\rho g}}. \tag{1.28}$$

For most common liquids, κ_c^{-1} is of the order of a few millimetres. Water in air has a capillary length of around 2.7 mm. For length scales $\ll \kappa_c^{-1}$, gravity can be assumed to be negligible and drops have constant mean curvatures. Above the capillary length ($> \kappa_c^{-1}$), gravity is dominant and it causes drops to flatten, resulting in non-constant curvatures (e.g. a puddle).

1.9.2 Particles on a liquid surface

When a few grains of some very fine powder, such as chalk, are sprinkled on the surface of water, they remain at the surface, even though the density of chalk is larger than water. However, when a large piece of chalk of the same density is placed on the same surface, it immediately sinks. This is another example where we transit from a surface tension dominated to a gravity dominated regime. Below a certain critical size, particles remain at the surface whereas, above that critical size, surface tension is insufficient to support the weight of the particle.

For a particle (radius R) that has a contact angle Θ with the liquid, the capillary force is proportional to γR. In contrast, the weight of the particle is proportional to $\Delta\rho g R^3$, where $\Delta\rho$ is the difference between the density of the particle and that of the liquid. Therefore, gravity can be neglected when $\Delta\rho g R^3 \ll \gamma R$. This corresponds to particles of radii,

$$R \ll \sqrt{\frac{\gamma}{g\Delta\rho}}. \tag{1.29}$$

This expression resembles the expression for κ_c^{-1}, except that here the density of the liquid has been replaced by the difference between the density of the solid and that of the liquid.

1.10 Thermal energy

As we have seen above, capillary forces are dominant for small particles, for which gravity can be ignored. This generally holds for particles smaller than a few micrometres. At such small length scales thermal energy has a significant influence

[8] More precisely, ρ is the difference between the density of the liquid and that of the surrounding fluid. But when the surrounding fluid is air, ρ is almost equal to the density of the liquid since the density of air is negligible in comparison.

on the dynamics of particles. Therefore, when considering the capillary force on small (nano/micro) particles at an interface, it is relevant to consider thermal energy. The equipartition theorem describes the thermal energy available to a system (e.g. a particle) that is in thermal equilibrium with its surroundings.

Equipartition theorem Very often, the energy of a system is quadratic in some variable. For example, this is the case for the kinetic energy ($E = mv^2/2$) and the potential energy of a spring ($E = kx^2/2$). Therefore, we can write the energy as a sum over n independent quadratic variables

$$E = \sum_{i=i}^{n} a_i x_i^2, \tag{1.30}$$

where $a_i > 0$ is some constant and x_i is some variable.

The probability $P(x)$ of a system having a particular energy $a_i x_i^2$ is proportional to the Boltzmann factor $e^{-\beta a_i x_i^2}$, where $\beta = 1/(k_\mathrm{B}T)$, k_B is the Boltzmann constant and T is the absolute temperature. Assuming that each x_i can take any value with equal probability, the mean energy is

$$\begin{aligned}
\langle E \rangle &= \int_{-\infty}^{\infty} \dots \int_{-\infty}^{\infty} EP(x_1, \dots, x_n)\, dx_1 \dots dx_n \\
&= \frac{\int_{-\infty}^{\infty} \dots \int_{-\infty}^{\infty} \sum_{i=1}^{n} a_i x_i^2 \exp\left\{-\beta \sum_{j=1}^{n} a_j x_j^2\right\} dx_1 \dots dx_n}{\int_{-\infty}^{\infty} \dots \int_{-\infty}^{\infty} \exp\left\{-\beta \sum_{j=1}^{n} a_j x_j^2\right\} dx_1 \dots dx_n} \\
&= \sum_{i=1}^{n} \frac{\int_{-\infty}^{\infty} \dots \int_{-\infty}^{\infty} a_i x_i^2 \exp\left\{-\beta \sum_{j=1}^{n} a_j x_j^2\right\} dx_1 \dots dx_n}{\int_{-\infty}^{\infty} \dots \int_{-\infty}^{\infty} \exp\left\{-\beta \sum_{j=1}^{n} a_j x_j^2\right\} dx_1 \dots dx_n} \\
&= \sum_{i=1}^{n} \frac{\int_{-\infty}^{\infty} a_i x_i^2 \exp\{-\beta a_i x_i^2\}\, dx_i}{\int_{-\infty}^{\infty} \exp\{-\beta a_i x_i^2\}\, dx_i} \\
&= \sum_{i=1}^{n} \frac{1}{2\beta} \\
&= \frac{n}{2} k_\mathrm{B} T.
\end{aligned} \tag{1.31}$$

Therefore, in thermal equilibrium, each quadratic 'mode' of the classical system contributes an equal amount of energy equal to $k_\mathrm{B}T/2$ to the system, such that the total mean energy of the system is equal to $n \times k_\mathrm{B}T/2$. This result is called the equipartition theorem.

1.11 Bulk flows

When a particle is surrounded by a moving fluid, it experiences a force due to the viscosity of the fluid (figure 1.11). In this section, I introduce the viscosity of a fluid and the viscous force acting on a particle that is submerged in a flowing fluid.

The *dynamic viscosity*, η, of a fluid is defined in terms of the shear stress required to create a velocity gradient normal to the direction of the shear:

$$\tau = \eta \frac{\partial u}{\partial z}. \tag{1.32}$$

Here, τ is the shear stress and $\partial u/\partial z$ is the velocity gradient. Viscosity is due to the lateral transfer of momentum between molecules colliding with one another. Water has a dynamic viscosity of 0.89 mPa s at room temperature (25 °C).

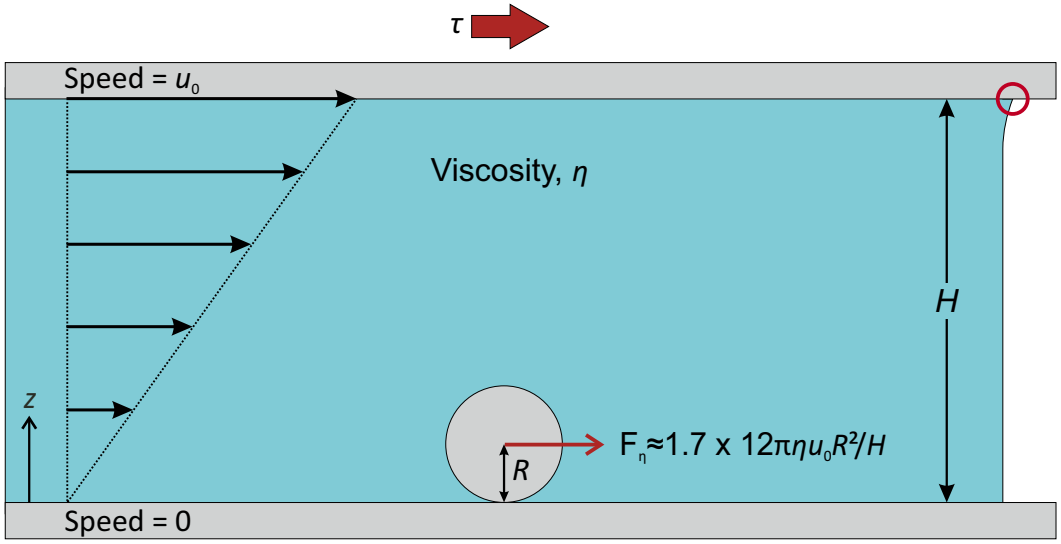

Figure 1.11: Particle in a laminar flow between two parallel plates. The bottom plate is fixed. A shear stress τ is applied on the top plate, causing a flow inside the liquid. The flow gives rise to a viscous force, F_η, on the particle.

The equation of motion (Newton's second law) for an incompressible fluid can be written in the form:

$$\frac{\partial \boldsymbol{u}}{\partial t} + \boldsymbol{u} \cdot \nabla \boldsymbol{u} = -\frac{\nabla p}{\rho} + \frac{\eta}{\rho} \nabla^2 \boldsymbol{u}. \tag{1.33}$$

Here, $\boldsymbol{u} = \boldsymbol{u}(x(t), y(t), z(t), t)$ is the velocity of the fluid at time t and position $(x(t), y(t), z(t))$. ρ is the density of the fluid, ∇p is the pressure gradient, $\nu \nabla^2 \boldsymbol{u}$ is the viscous acceleration. Any external forces, such as gravity, will appear as additive terms on the right hand side. Equation 1.33 is the Navier-Stokes equation for viscous and incompressible fluids.

The relative importance of inertial to viscous forces can be compared by introducing a typical velocity scale $\sim |\boldsymbol{u}| \sim U$ and a typical length scale of variation, $\nabla \sim 1/L$. Then,

$$\frac{|\text{inertial acceleration}|}{|\text{viscous acceleration}|} = \frac{|\boldsymbol{u}\cdot\nabla\boldsymbol{u}|}{|\nu\nabla^2\boldsymbol{u}|} \sim \frac{UL}{\nu}. \tag{1.34}$$

The non-dimensional number, UL/ν, is called the Reynolds number, Re.

When $\mathrm{Re} \gg 1$, inertial forces typically dominate, whereas when $\mathrm{Re} \ll 1$, viscous forces typically dominate. Usually, flows with low Re are laminar and flows with high Re are turbulent. All the experiments presented in this thesis involve only laminar flows.

For a steady state laminar flow (or Stokes flow),[9] equation 1.33 reduces to

$$\frac{\nabla p}{\rho} = \nu\nabla^2\boldsymbol{u}. \tag{1.35}$$

The flow and pressure fields for Stokes flow past a spherical particle are obtained by solving equation 1.35 subject to the corresponding boundary conditions (no-slip in velocity at the surface of the sphere, no flow into/out of the particle, unperturbed flow far from the sphere). The resistive force experienced by the particle is obtained by integrating the viscous stress over the surface of the particle. The result is called Stokes' law:

$$\boldsymbol{F_\eta} = 6\pi\eta R\boldsymbol{u}, \tag{1.36}$$

where R is the radius of the sphere and $\boldsymbol{u}$ is the mean velocity of the particle relative to the surrounding fluid.

When the particle is in contact with a solid surface instead of being surrounded by fluid all around, the flow profile changes due to the no-slip boundary condition at the solid surface. Consequently, Stokes's law has to be corrected by a multiplicative factor [51]:

$$F_\eta = 1.7 \times 6\pi\eta R\langle\boldsymbol{u}\rangle, \tag{1.37}$$

where $\langle\boldsymbol{u}\rangle$ is the mean velocity of the fluid relative to the particle.

1.12 Dynamic contact angles

In the previous section, I described the flow inside a liquid, ignoring the motion of the liquid-air interface. When studying moving drops, it is important to consider the motion of the three-phase contact line (highlighted by the red circle in figure 1.11). The speed at which a liquid can move is strongly limited when a three-phase contact line is present. Speed also influences the contact angle between the drop and the surface.

[9] Steady state means $\partial\boldsymbol{u}/\partial t = 0$ and laminar means that we can ignore $\boldsymbol{u}\cdot\nabla\boldsymbol{u}$

The velocity dependence of the contact angle has been the subject of numerous experimental and theoretical studies. The two most common models describing the speed dependence of the contact angles are the hydrodynamic model and the molecular-kinetic model [16, 104, 30, 17].

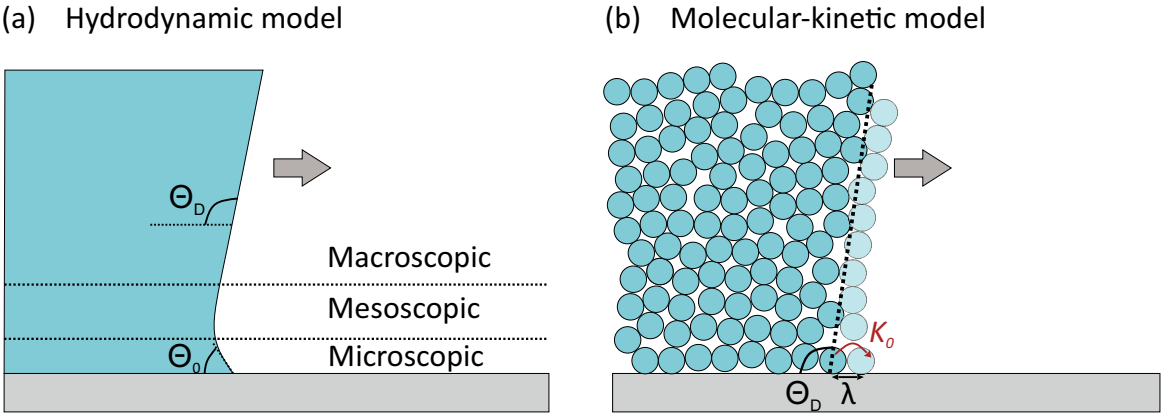

Figure 1.12: Dynamic contact angle in the (a) hydrodynamic model and (b) the molecular-kinetic model. In the hydrodynamic model, the microscopic contact angle, Θ_0, is usually assumed to be constant. The interface undergoes viscous bending on the mesoscale, causing the dynamic macroscopic contact angle, Θ_D, to differ from Θ_0. In the molecular kinetic model, Θ_0 changes with speed and is equal to Θ_D.

The hydrodynamic model assumes that the Reynolds number is small such that inertial effects can be neglected. Furthermore, the capillary number ($\mathrm{Ca} = \eta U/\gamma$, where η is the dynamic viscosity, U is the speed of the interface and γ is the surface tension) is assumed to be small such that the liquid-air interface takes its (undeformed) static shape far from the contact line [figure 1.12 (a)]. However, viscous dissipation becomes important in the mesoscopic region close to the moving three-phase contact line. This causes the liquid-air interface to bend and consequently influences the macroscopic contact angle. In the hydrodynamic model, the dynamic advancing and receding contact angles are given by

$$\Theta_\mathrm{D}^3(v) = \Theta_0^3 \pm \frac{9\eta v}{\gamma} \ln \frac{L_0}{L_i}, \tag{1.38}$$

where the $+$ corresponds to an advancing interface and the $-$ corresponds to a receding interface. L_0 is a macroscopic length scale, usually taken to be the capillary length or the size of the drop. L_i is a cut-off length introduced to remove a singularity at the contact line. L_i is usually taken to be the size of a molecule.

The molecular-kinetic model is based on the statistical mechanics of liquid molecules close to the three-phase contact line. The region close to the contact line is viewed as consisting of liquid molecules that continuously adsorb/desorb on the solid surface [figure 1.12 (b)]. When the contact line is in motion, the adsorption equilibrium is disturbed, causing the local surface tensions and consequently

the (microscopic) contact angle to change. In this model, the microscopic and macroscopic angles are equal. According to the molecular-kinetic model,

$$v = 2K_0\lambda \sinh\left\{\frac{\gamma\lambda^2}{2k_\mathrm{B}T}[\cos\Theta_0 - \cos\Theta_\mathrm{D}(v)]\right\}, \tag{1.39}$$

where K_0 is the characteristic frequency at which molecules adsorb/desorb, λ is the distance between adsorption sites, T is the absolute temperature and k_B is the Boltzmann constant. A positive (negative) value for v has to be inserted for the advancing (receding) side.

Both the hydrodynamic and molecular-kinetic models predict that Θ_A increases with speed whereas Θ_R decreases with speed. They assume that the surface properties (described by surface tensions) of the surface and the liquid do not change over time. While this is often valid, there are several cases where the assumption fails. Recently, Butt *et al.* (2018) [23] proposed a model to account for adaptation processes that may occur in a solid when it is in contact with a liquid. Adaptation causes the surface tensions to change. This phenomenon has been termed *adaptive wetting* and it will be discussed in detail in chapter 3.

1.13 Adhesion between two solids

Consider a solid A made up of molecules of type A and a solid B made up of molecules of type B. Both A and B are assumed to be electrically neutral.

Interaction energy between two molecules In a vacuum, a molecule A and a molecule B attract each other due to van der Waals forces. The potential energy of the van der Waals interaction is given by

$$w_\mathrm{AB} = -\frac{C_\mathrm{AB}}{r^6}, \tag{1.40}$$

where C_AB is a constant that depends on the properties of molecules A and B.

Interaction between two extended solids The interaction energy between a solid A and solid B (both containing a large number of molecules) can be obtained by adding up the interaction energies between all possible pairs of molecules A and B. This calculation was first performed by Hugo Hamaker (1937) [53]. For two semi-infinite planes separated by a distance D, the van der Waals potential energy per unit area is

$$w_\mathrm{adh} = -\frac{A_\mathrm{H}}{12\pi D^2}. \tag{1.41}$$

A_{H} is called the Hamaker constant and is given by $A_{\mathrm{H}} = \pi^2 C_{\mathrm{AB}} \rho_{\mathrm{A}} \rho_{\mathrm{B}}$, where ρ_{A} and ρ_{B} is the number density of the molecules in solids A and B, respectively. When the two surfaces are in contact, D is taken as the interatomic distance.

On a macroscopic level, w_{adh} is the work of adhesion. It is the energy required to separate a unit area of solid A from solid B and it can be expressed in terms of the surface energies of the two solids, γ_1 and γ_2, and the interfacial energy γ_{12} between them (figure 1.13) :

$$w_{\mathrm{adh}} = \gamma_1 + \gamma_2 - \gamma_{12}. \tag{1.42}$$

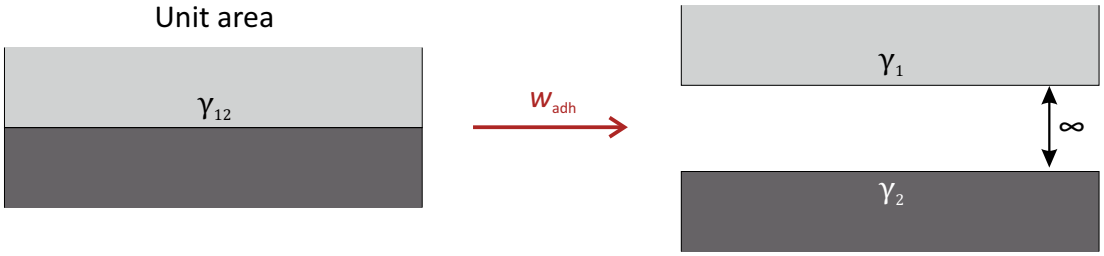

Figure 1.13: The work of adhesion is the energy per unit area required to separate the two surfaces.

For a spherical particle at a separation distance D from semi-infinite flat surface, Hamaker's calculation for the van der Waals potential energy gives

$$w_{\mathrm{particle-plane}} = -\frac{A_{\mathrm{H}} R}{6D}, \tag{1.43}$$

where, R is the radius of the particle. The corresponding force between the particle and the surface is

$$F_{\mathrm{particle-plane}} = -\frac{dw_{\mathrm{particle-plane}}}{dD} = -\frac{A_{\mathrm{H}} R}{6D^2}. \tag{1.44}$$

The above equation can be written in terms of the plane-plane work of adhesion (by substituting equation 1.41 in equation 1.44):

$$F_{\mathrm{particle-plane}} = 2\pi R w_{\mathrm{adh}}. \tag{1.45}$$

Deformable solids Equation 1.45 assumes that the particle and the flat surface are infinitely rigid such that they do not deform due to the adhesion force. In practice, real solids are never completely rigid but they deform under externally applied forces as well as adhesion forces (figure 1.14).

The theory by Johnson, Kendall, and Roberts (JKR) [66] describes the adhesion between two solids that are allowed to undergo elastic deformations. External and/or adhesion forces, F, between the two solids cause them to deform whereas the stored elastic potential energy tries to restore their unperturbed state. In mechanical

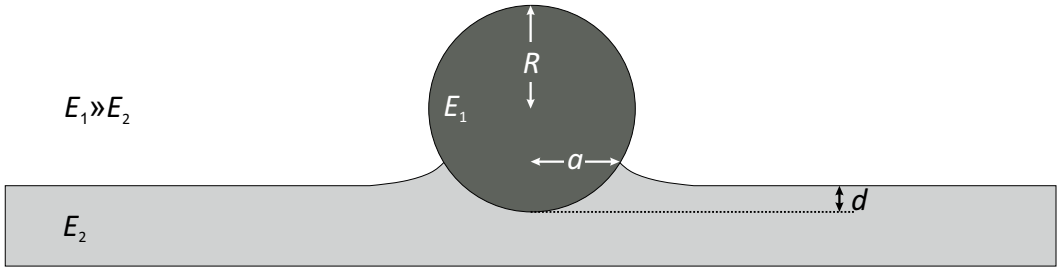

Figure 1.14: A rigid particle in contact with an elastic surface. The surface deforms due to adhesion between the two bodies, resulting in a contact radius, a, and an indentation depth, d.

equilibrium, the contact radius, a, between a spherical particle and a flat surface is given by

$$a^3 = \frac{3R}{4E^*}\left[F + 3\pi R w_{\text{adh}} \pm \sqrt{6\pi R w_{\text{adh}} F + (3\pi R w_{\text{adh}})^2}\right], \tag{1.46}$$

and the indentation is given by

$$d = \frac{a^2}{R} - \sqrt{\frac{2\pi a w_{\text{adh}}}{E^*}}, \tag{1.47}$$

where R is the radius of the particle and E^* is the reduced Young's modulus of the two materials. E^* is related to the Young's modulus of the two solids according to

$$\frac{1}{E^*} = \frac{1-\nu_1^2}{E_1} + \frac{1-\nu_2^2}{E_2}, \tag{1.48}$$

where E_1 and E_2 are the Young's modulus of the two solids, and ν_1 and ν_2 are their Poisson ratios.

The adhesion force corresponds to the maximum negative value that F can take while still providing real solutions to equation 1.46.[10] As F becomes more negative, the term under the square root becomes less positive. Real solutions are obtained as long as

$$6\pi R w_{\text{adh}} F + (3\pi R w_{\text{adh}})^2 \geq 0 \tag{1.49}$$

Therefore, the adhesion force is

$$F_{\text{adh}} = \frac{3}{2}\pi R w_{\text{adh}}. \tag{1.50}$$

F_{adh} is proportional to R, whereas the gravitational force is proportional to R^3. Therefore, for small R, $R^3 \ll R$ and F_{adh} dominates. As R gets larger, R^3 becomes larger than R and the gravitational force dominates.

[10] In this formalism, positive forces correspond to forces pressing the two solids together and negative forces correspond to forces that act to separate the two solids. Therefore, the adhesion force is the maximum negative force that can be sustained before detachment occurs.

Although values for w_{adh} have been calculated and measured for a wide range of materials, they are often of limited practical value in predicting the adhesion force (using equation 1.50) between solids under normal conditions because surfaces usually get covered with contaminants or other impurities over time when exposed to the environment. This may cause the real values of w_{adh} to deviate from their calculated values, and from their previously measured values because experiments are usually performed under ideal conditions such as in a vacuum to prevent contamination of the surfaces. Therefore, equation 1.50 should be viewed as a way to determine w_{adh} by measuring F_{adh} rather than as a way to predict F_{adh} from w_{adh}.

Influence of humidity In a humid environment, water vapour condenses at the contact between hydrophilic particles and hydrophilic surfaces [110, 45, 25]. The presence of a water meniscus can significantly affect the adhesion force.

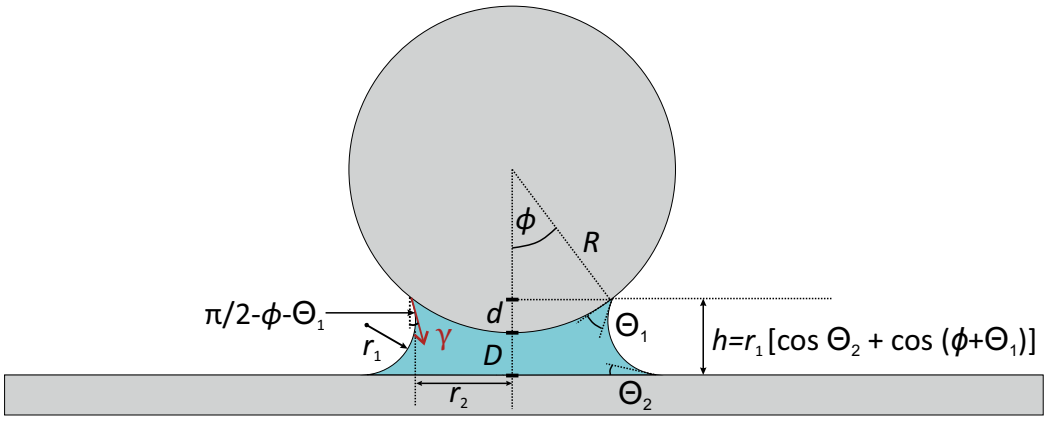

Figure 1.15: A particle of radius R surrounded by a liquid meniscus of height h. The segments with radii r_1 and r_2 (in the azimuthal direction) are assumed to be circular. Although the real shape of the interface is a nodoid or an unduloid rather than a circle, the circular approximation is valid for most practical cases. Numerical calculations showed that the difference between the mean curvatures calculated using the circular approximation and the exact geometry is less than 6.5% when $\phi \leq 10^\circ$ and $\Theta_1 \leq 60^\circ$ [84].

The capillary adhesion caused by the water meniscus has two contributions. The first contribution is due to the action of surface tension at the three-phase contact line on the particle: $2\pi R\gamma \sin\phi \sin(\phi + \Theta_1)$ (refer to figure 1.15 for the geometrical parameters). The second contribution is due to the pressure difference (Laplace pressure) between water inside the meniscus and air outside of the meniscus. When evaluated at the thinnest part of the meniscus, the Laplace pressure is $\Delta P = \gamma(1/r_2 - 1/r_1)$.[11] The Laplace pressure acts over an effective horizontal area $\pi R^2 \sin^2\phi$ and

[11]The two radii of curvature of the meniscus are obtained by fitting circular arcs to the air-water interface. It is evident that the precise shape of the interface is not circular because this leads to inconsistent values of Laplace pressure when choosing different points along the interface. For example, when the Laplace pressure is evaluated at the three-phase contact line on the particle (instead of at the thinnest region), the Laplace pressure is $\Delta P = \gamma(1/R\sin\phi - 1/r_1)$ (instead of

therefore gives rise to a downwards vertical force of $\pi R^2 \sin^2\phi \Delta P$. Adding these two force contributions gives an adhesion force of

$$F_{\gamma,\ \mathrm{adh}} = 2\pi R \sin\phi\gamma \sin(\phi + \Theta_1) - \pi R^2 \gamma \sin^2\phi \left(\frac{1}{r_2} - \frac{1}{r_1}\right). \tag{1.51}$$

Typically, $r_1 \ll r_2$ and $r_1 \ll R$. Therefore, the term proportional to $1/r_1$ in the Laplace pressure term dominates and equation 1.51 simplifies to

$$F_{\gamma,\ \mathrm{adh}} = \frac{\gamma}{r_1}\pi R^2 \sin^2\phi. \tag{1.52}$$

To express $F_{\gamma,\ \mathrm{adh}}$ in terms of the separation distance D, $\sin^2\phi$ is expressed as

$$\sin^2\phi = 1 - \cos^2\phi = 1 - \left(\frac{R-d}{R}\right)^2 = 1 - \left(\frac{R-h+D}{R}\right)^2 \approx 2\left(\frac{h-D}{R}\right).$$

The last approximation is valid for $h + D \ll R$. Substituting the above relation into equation 1.52 gives

$$F_{\gamma,\ \mathrm{adh}} = 2\pi\gamma R \left(\frac{h-D}{r_1}\right). \tag{1.53}$$

Based on the geometry, h can also be expressed in terms of the contact angle Θ_1 between the liquid and the particle and the contact angle Θ_2 between the liquid and the flat surface:

$$h = r_1[\cos\Theta_2 + \cos(\phi + \Theta_1)]. \tag{1.54}$$

By substituting the above equation into equation 1.53, $F_{\gamma,\ \mathrm{adh}}$ can also be written as

$$F_{\gamma,\ \mathrm{adh}} = 2\pi\gamma R \left[\cos\Theta_2 + \cos(\phi + \Theta_1) - \frac{D}{r_1}\right]. \tag{1.55}$$

When the particle is in contact with the surface, $D = 0$ and therefore,

$$F_{\gamma,\ \mathrm{adh}} = 2\pi\gamma R \left[\cos\Theta_2 + \cos(\phi + \Theta_1)\right]. \tag{1.56}$$

Depending on the types of materials that are in contact, humidity may sometimes decrease the total adhesion force, despite the capillary adhesion. A decrease in the adhesion force may occur if the particle and the surface initially carried opposite electrostatic charges. Since water is a good conductor, it reduces/eliminates adhesion due to electrostatic forces. Therefore, the total adhesion force decreases in cases where the initial electrostatic attraction is greater than the capillary adhesion.

$(1/r_2 - 1/r_1)$). However, the radius r_1 is usually much smaller than the second radius. Therefore, no matter where the Laplace pressure is evaluated, $\Delta P = -1/r_1$ is a good approximation as long as $r_1 \ll r_2$. Therefore, the circular approximation is generally a good assumption when $r_1 \ll r_2$. The advantage of using the circular approximation is that it leads to analytical results.

1.14 Friction between two solids

Friction is the force that opposes relative lateral motion between two surfaces. In general, the friction force, F_F, between two solids is given by

$$F_F = \mu N, \tag{1.57}$$

where μ is called the coefficient of friction and N is the normal reaction. N has contributions due to gravity (when the object is on a horizontal surface) and due to the adhesion force, F_{adh}, described above. For small particles, the gravitational force is negligible compared to the adhesion force and therefore,

$$F_F \approx \mu F_{\text{adh}}. \tag{1.58}$$

In general, the coefficient of friction is significantly smaller for a rolling object compared to a sliding object.

Chapter 2

Experimental methods

In this chapter, I will describe the main experimental methods that will be used to obtain the results presented in later chapters. I will focus on two methods that I have designed and implemented during my PhD.

The first method involves using an inverted laser scanning confocal microscope to directly measure friction forces. Over the past decade, laser scanning confocal microscopy has proved to be a powerful tool in various fields, including soft matter physics, chemistry and biology. The main advantage of confocal microscopy over other types of optical microscopy is that it provides well-resolved three-dimensional information, including at the interface between different phases, as long as the phases have similar refractive indices. So far, confocal microscopy has been used primarily for imaging. In section 2.2, I will demonstrate how confocal microscopy can also be used to measure friction forces. The combination of confocal imaging and friction force measurements is useful to study a range of problems where it is valuable to image processes with microscopic resolution as well as quantify the forces associated with these processes. I will use this method to study how drops remove particles from surfaces in chapter 5.

The second method, called the *surface pendant drop method*, involves measuring the surface tension of drops as they accumulate contaminants from a surface. The surface pendant drop method is an adaptation of the standard pendant drop method (section 1.4.5). With the surface pendant drop method, the drop is suspended from a surface instead of from a syringe needle. It is known that when drops are placed on certain types of surfaces, molecules on the surface readjust to the presence of the drops. This has been termed *adaptive wetting* [23]. In the case of water drops on silicone (PDMS) surfaces, uncrosslinked molecules migrate from the surface to the drop-air interface, resulting in a change in the surface tension of the drop. In chapter 3, I will apply the surface pendant drop method to measure the change in the surface tension of drops over time when they are placed in contact with silicone surfaces.

2.1 Laser Scanning Confocal Microscopy (LSCM)

LSCM is inspired by two techniques: fluorescence microscopy and confocal microscopy. Fluorescent microscopy was invented in 1904 and has been used to image antibodies in biological cells since the 1970s [5].

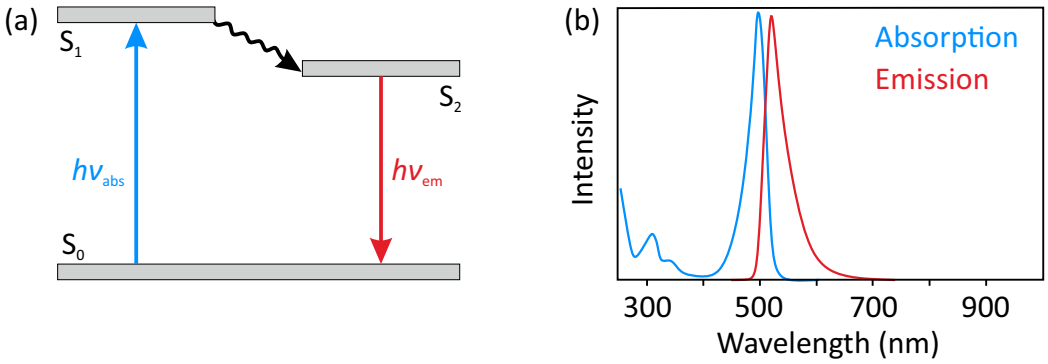

Figure 2.1: (a) Jablonski diagram showing the excitation of an electronic state S_0 to a state S_1 through absorption of a photon of energy $h\nu_{\text{abs}}$. S_1 exists for a finite time (typically 1 ns to 10 ns) before partially dissipating energy to reach a state S_2. Fluorescent light is emitted when S_2 relaxes to S_0. (b) An example of an absorption and emission spectrum of a typical fluorophore (Atto 488 from Atto-Tec).

Fluorescence microscopy In fluorescence microscopy, monochromatic light is incident on a sample containing a fluorescent marker. Fluorescent markers are molecules whose electrons are excited to a high energy state by absorbing light of a certain frequency. The excited electrons subsequently relax (within $< 1 \times 10^{-7}$ s [57]) to their ground electronic state by emitting photons (figure 2.1). Typically, the energy of the emitted photons is less than the energy of the absorbed photons - a phenomenon called Stoke's shift. The remaining part of the energy is typically dissipated in the form of vibrational or rotational relaxations of the molecule [57]. In fluorescence microscopy, parts of a sample are selectively marked with fluorescent markers. Fluorescence microscopy allows very small regions (such as proteins in cells) to be detected as long as fluorescent markers can be added to these regions. By labelling the relevant regions in a sample with fluorescent molecules, it is possible to image the region of interest while intentionally ignoring the rest of the sample.

A simplified schematic of a fluorescent microscope is shown in figure 2.2. A light source emits monochromatic light (blue rays) onto a dichroic mirror. The dichroic mirror is chosen such that it reflects the emitted light (blue) but allows fluorescent light (red) to pass through. The objective lens focuses the incident light onto the sample (point A). Fluorescent molecules at point A are excited and they subsequently emit fluorescent light (red) in all directions. Part of the emitted fluorescent light travel back onto the objective and through the dichroic mirror, reaching a second lens that focuses the light onto a detector.

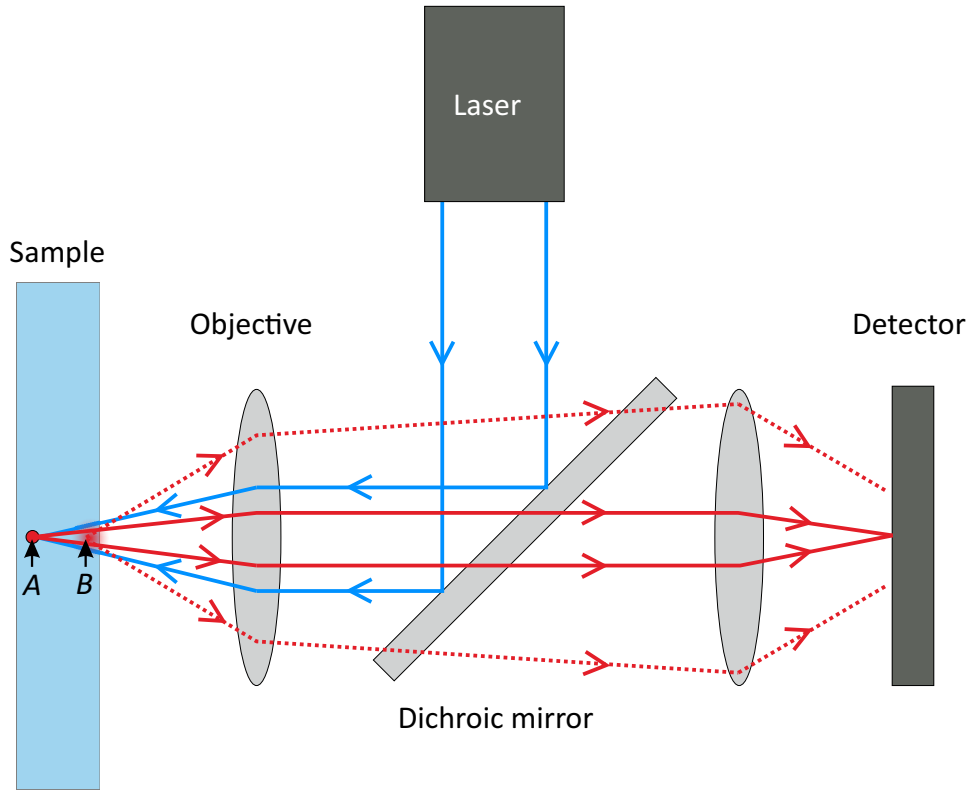

Figure 2.2: Beam path in fluorescence microscopy. Point A lies in the focal plane of the objective lens and rays emerging from A converge onto the detector. However, the incident light also illuminates regions that are not in focus (e.g. point B). Fluorescence signal from point B also reaches the detector but appears out-of-focus.

The main drawback of fluorescence microscopy is that the out-of-focus parts of the fluorescent signal give rise to a uniform out-of-focus background [5]. For example, fluorescent molecules at point B in figure 2.2 are also excited by the incident light. They emit fluorescent light that reaches the detector as an out-of-focus spot. Therefore, is not possible to distinguish features in the focal plane from those in the background clearly. Furthermore, fluorescent markers may experience photobleaching, which is particularly problematic for long experiments.[1]

Confocal microscopy Confocal microscopy was invented in 1955 by Minsky [79]. However, the term 'confocal' was only introduced two decades later by Brakenhoff *et al.* (1979) to describe a microscope that focuses light onto a single spot in a sample and detects light only from the illuminated spot [5]. Microscopes combining fluorescence microscopy and confocal microscopy were commercialised in the 1980s.

In confocal microscopy, the out-of-focus light can be blocked by inserting a pinhole at a position optically conjugate to the focussed spot, as shown in figure 2.3. With this addition, it is possible to eliminate the background light and therefore image a localised spot, without obtaining out-of-focus light from the rest of the sample.

[1]Photobleaching occurs when a fluorescent marker undergoes a photon-induced chemical alteration and permanently loses the ability to fluoresce.

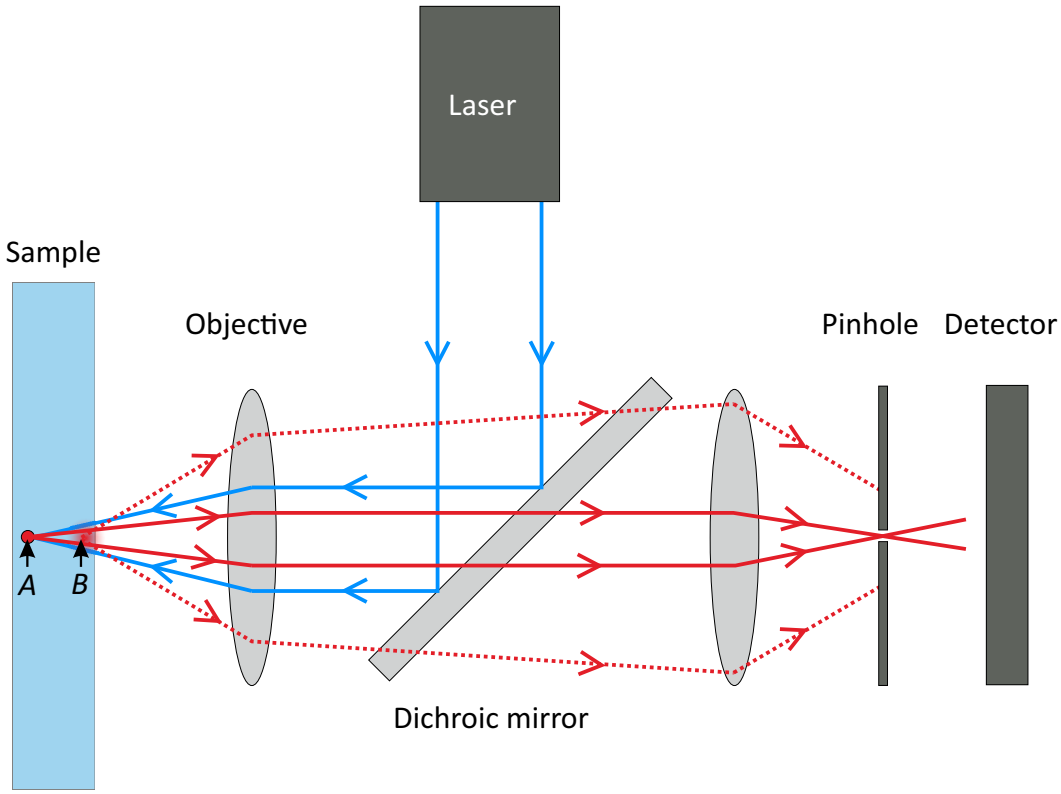

Figure 2.3: Beam path in confocal fluorescence microscopy. The pinhole filters out out-of-focus light rays (e.g. from point B).

Since a confocal microscope can only image a single point at a time, the sample has to be 'scanned' (hence the name LSCM) in order to image an extended region. Scanning is performed either by moving the sample or by moving the laser beam (e.g. using rotating mirrors) to focus the incident light beam on different points. Most modern systems use the latter approach since it generally allows faster image acquisition. The fluorescent signal emitted from each spot is then combined using computer software to construct an image of the scanned region. Since the laser scans across the sample one point at a time, obtaining an extended image is relatively slow compared to methods such as high-speed microscopy. LSCM works optimally when the sample under observation has a uniform refractive index. A mismatch between the refractive indices of different parts of the sample gives rise to unwanted reflections and refractions.

All the confocal images presented in this thesis were taken with a Leica TCS SP8 inverted laser scanning confocal microscope, which has a lateral resolution of around 200 nm and an axial resolution of around 1 µm. Inverted means that the sample is viewed from below (figure 2.4) instead of from above, as is the case with conventional microscopes. Imaging from below is often beneficial to study the behaviour of drops on surfaces since it enables us to image the three-phase contact line. Imaging the contact line is difficult with a conventional upright microscope since the laser beam has to travel through the curved drop-air interface, which causes significant refraction and

therefore leads to a distorted image of the contact line. With the Leica TCS SP8, it is possible to image in reflection mode and multiple fluorescence modes simultaneously. For instance, if different features of a sample are labelled with different fluorescent markers, the fluorescence signal from each feature can be captured independently. Then, a final image is constructed by overlaying all the detected signals. This is particularly useful for problems that have multiple phases, such as a water drop on a liquid-infused surface.

A typical scanning frequency is around 1000 lines per second. Therefore, to scan an area of $205\,\mu m \times 205\,\mu m$ it takes $1024/1000 \approx 1\,s$ when using a pixel size of 200 nm. This estimate can be faster or slower depending on the exact pixel size, scanning speed and magnification. In this thesis, I have used different types of objective lenses, depending on the experiment. Table 2.1 provides details (magnification, numerical aperture [2], ...) of all the objective lenses that were used in this thesis.

Table 2.1: List of objective lenses. The name of the lens contains the magnification and the numerical aperture. For example, 20x/0.75 means that the objective lens has a magnification of 20 times and a numerical aperture of 0.75. FWD is the free working distance.

Name of objective lens	FWD (mm)	Immersion medium
Leica HC PL APO IMM CORR CS2 20x/0.75	0.68	Oil/glycerol
Leica HCX PL APO CS 10x/0.40	2.20	Dry
Leica PL FLUOTAR 2.5x/0.07	9.2	Dry

2.2 Measuring forces with LSCM

Force measurements are valuable in describing physical processes since they allow us to quantitatively test theories and to find trends and patterns. In this section, I describe how horizontal forces can be measured with an inverted LSCM using a blade clamped directly above the objective lens. The combination of forces and confocal imaging allows us to image samples with microscopic resolution and to directly measure friction forces (resolution 200 nN) *in situ*.

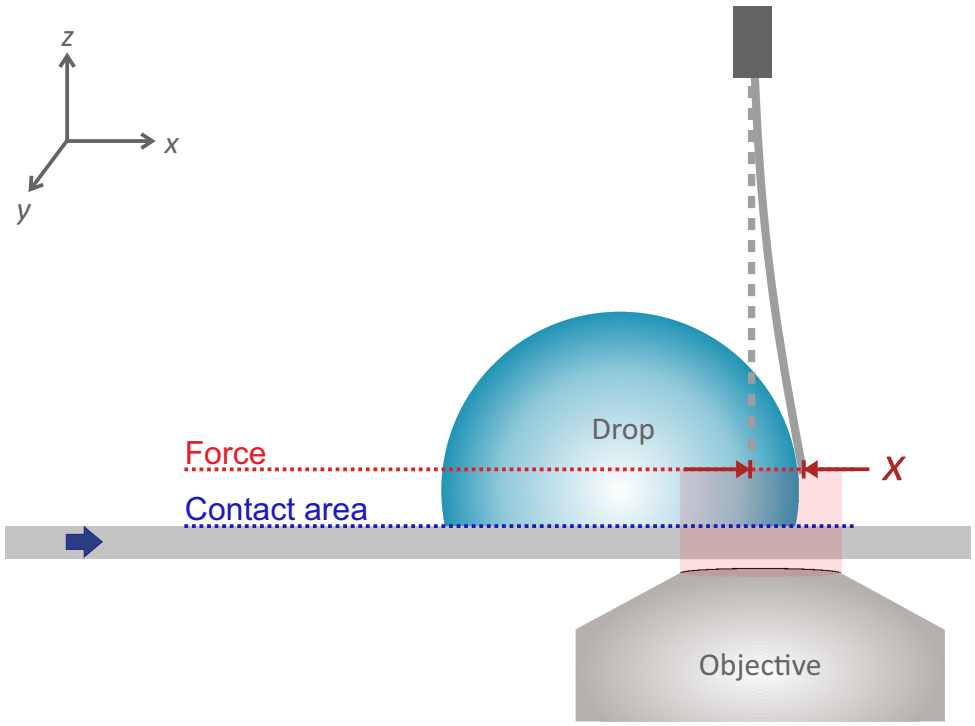

Figure 2.4: Setup for measuring forces with LSCM. The focal plane is set at the bottom edge of the blade (red dotted line) when measuring forces. When imaging the drop-surface contact area, the focal plane is set at the blue dotted line.

2.2.1 Basic principle

The basic idea of using LSCM to measure horizontal forces is sketched in figure 2.4. A rectangular blade is clamped directly above the objective lens. The clamp is mounted on a support that is connected to a micromanipulator. The micromanipulator is used to precisely position the blade. The free working distance of the objective has to be sufficiently large such that it can focus on the bottom edge of the blade, which is usually around 1 mm above the objective.[3]

After positioning the blade, such that its lower edge is in focus, the laser is set to scan from left to right at a given frequency (up to 8 192 Hz). When the laser beam hits the bottom edge of the blade, some of the light is reflected towards the objective. The reflected light is captured by the detector and the position of the blade is obtained. When a force is applied to the blade, it deflects from its equilibrium position. For small deflections, the position of the bottom edge can be monitored continuously. By recording the deflection of the blade, the force causing the deflection can be obtained using Hooke's law,

[2]The numerical aperture is given by NA $= n \sin \alpha$, where n is the refractive index of the immersion medium and α is the maximum half-angle of the cone of light that can enter or exit the lens. A larger NA results in a higher spatial resolution (resolution $\propto 1/\mathrm{NA}$). Immersion objectives generally have larger numerical apertures than dry objectives.

[3]Objectives with large working distances typically have lower resolutions. Therefore, the objective should be chosen such that it has just about enough (but not too much excess) free working distance. I used the 10x objective (table 2.1) which was a good compromise.

$$F = kx, \tag{2.1}$$

where k is the spring constant of the blade and x is the deflection of the bottom edge from its equilibrium position. Therefore, the force acting at the bottom edge can be obtained as a function of time, provided that the spring constant is known.

2.2.2 Spring constant

The blade has to be carefully chosen depending on the system under investigation. The bottom edge of the blade must stay within the field of view of the objective at all times during a measurement. Therefore, the blade has to be sufficiently stiff such that the maximum horizontal deflection is less than the field of view (figure 2.5). Furthermore, the deflection in the vertical direction must be smaller than the focal depth of the objective lens. Otherwise, the reflected signal will move out of the focal plane. However, having a spring that is too stiff is also detrimental because it may result in deflections that are too small, therefore compromising on measurement precision.

Optimally, the blade must be chosen such that (1) the vertical deflection is less than the focal depth of the objective lens and (2) the horizontal deflection is as large as possible but less than the field of view of the objective.

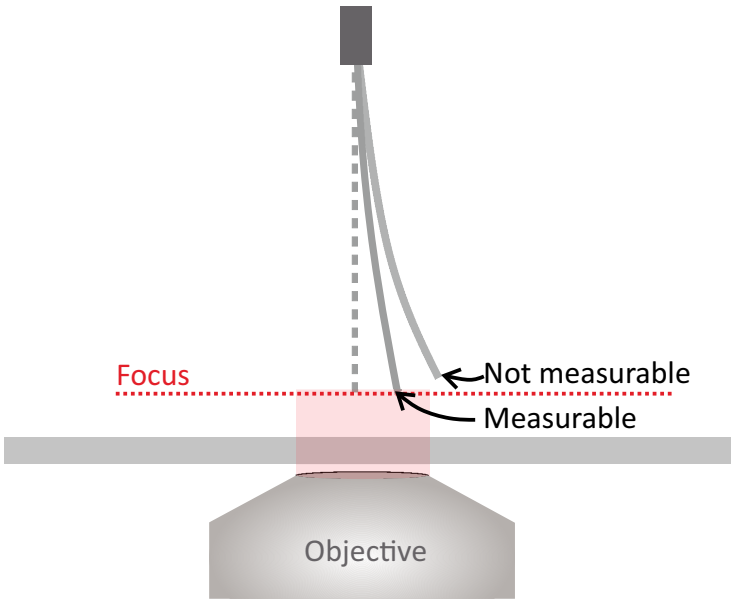

Figure 2.5: Deflections that are too large cannot be measured because the bottom edge of the blade either moves above the focus (dotted red line) or out of the field of view of the objective (or both).

It is crucial that the spring constant of the blade is accurately calibrated. In the following, I will describe two methods to determine the spring constant and the uncertainties associated with each method.

2.2.2.1 Spring constant from the blade's dimensions

The spring constant of a rectangular blade is related to its dimensions according to [24]

$$k = \frac{Ewh^3}{4l^3}, \tag{2.2}$$

where E is the Young's modulus of the blade, w is the width, h is the thickness, and l is the length (excluding the part that is clamped). This formula is valid when the blade is clamped at one end and the force applied at the opposite end. Since the blade's spring constant is highly sensitive on its length and thickness (cubic dependence), the spring constant can be tuned over a wide range by adjusting these parameters. It is important that the blade has a uniform width and thickness throughout its entire length. Otherwise, the blade cannot be assumed to be rectangular and determining the spring constant becomes a lot more complicated.

I used commercially available stainless steel feeler gauge tapes ($E = 200\,\mathrm{GPa}$) from Orion as the blade. Feeler gauge tapes were chosen since they have a highly uniform thickness, which is measured and provided by the manufacturer. The tapes can be cut precisely into different lengths and widths using a sheet metal guillotine. In the experiments presented in this thesis, I used blades of thicknesses between 40 µm and 70 µm, widths between 3 mm and 5 mm, and lengths between 5 cm and 10 cm.

When measuring an *a priori* unknown force, it is convenient to start with a short (stiff) blade, and successively increasing its length until the deflection of the blade can be measured clearly with the microscope.

Uncertainty using blade dimensions Using equation 2.2 to calculate the spring constant leads to a fractional uncertainty of

$$\begin{aligned}
\frac{\Delta k}{k} &= \sqrt{\left(\frac{\Delta E}{E}\right)^2 + \left(\frac{\Delta w}{w}\right)^2 + \left(3\frac{\Delta h}{h}\right)^2 + \left(3\frac{\Delta l}{l}\right)^2} \\
&= \sqrt{\left(\frac{10\,\mathrm{GPa}}{200\,\mathrm{GPa}}\right)^2 + \left(\frac{0.1\,\mathrm{mm}}{5\,\mathrm{mm}}\right)^2 + \left(3\frac{1\,\mu\mathrm{m}}{40\,\mu\mathrm{m}}\right)^2 + \left(3\frac{0.1\,\mathrm{mm}}{50.0\,\mathrm{mm}}\right)^2} \\
&= \sqrt{25.00 + 4.00 + 56.25 + 0.36}\ \% \approx 9\%.
\end{aligned} \tag{2.3}$$

Here, I have used parameters corresponding to a blade with the following specifications: $E = (200 \pm 10)\,\mathrm{GPa}$ (stainless steel), $w = (5.0 \pm 0.1)\,\mathrm{mm}$, $h = (40 \pm 1)\,\mu\mathrm{m}$ and $l = (50.0 \pm 0.1)\,\mathrm{mm}$. l, w and h were measured with a digital vernier caliper having a precision of 0.1 mm.

2.2.2.2 Spring constant from the natural frequency

The spring constant of the blade can also be determined from its natural frequency of oscillations. The natural frequency of oscillations can be measured using the confocal microscope. The bottom edge is displaced by a small amount from its equilibrium position and then released. The resulting oscillations are recorded and the frequency, f, of the oscillations is extracted. The spring constant is then calculated from this frequency using the relation [24]

$$k = 0.243 m\omega^2, \tag{2.4}$$

where m is the mass of the blade protruding from the clamp and $\omega = 2\pi f$. This formula assumes a rectangular blade with uniform mass distribution.

Uncertainty with the frequency method To estimate the fractional uncertainty in the spring constant, it is useful to first rewrite equation 2.4 as

$$k = 0.243 M \frac{l}{L}\left(\frac{2\pi}{T}\right)^2, \tag{2.5}$$

where M and L are the total mass and total length of the blade, respectively (including the part that it clamped). l is the suspended length (excluding the part that is clamped), and T is the time period of the oscillations. The fractional uncertainty is given by

$$\begin{aligned}
\frac{\Delta k}{k} &= \sqrt{\left(\frac{\Delta M}{M}\right)^2 + \left(\frac{\Delta L}{L}\right)^2 + \left(\frac{\Delta l}{l}\right)^2 + \left(2\frac{\Delta T}{T}\right)^2} \\
&= \sqrt{\left(\frac{0.1\,\mathrm{mg}}{72.3\,\mathrm{mg}}\right)^2 + \left(\frac{0.1\,\mathrm{mm}}{100.0\,\mathrm{mm}}\right)^2 + \left(\frac{0.1\,\mathrm{mm}}{50.0\,\mathrm{mm}}\right)^2 + \left(2\frac{0.000\,1\,\mathrm{s}}{0.085\,4\,\mathrm{s}}\right)^2} \\
&\approx \sqrt{0.02 + 0.01 + 0.04 + 0.05}\ \% = 0.3\%.
\end{aligned} \tag{2.6}$$

For the above estimate, I have used a blade with the following parameters: $M = (72.3 \pm 0.1)\,\mathrm{mg}$, $L = (100.0 \pm 0.1)\,\mathrm{mm}$, and $l = (50.0 \pm 0.1)\,\mathrm{mm}$. M was measured with an electronic weighing scale with a precision of 0.1 mg. The uncertainty in the time period of oscillations is proportional to the absolute temporal resolution, ΔT_0, of the microscope (1 ms or better). The natural frequency (11.7 Hz for this blade) was obtained by averaging over multiple oscillations. When averaging over n oscillations, the temporal resolution is $\Delta T = (\Delta T_0)/n$. In the above estimate, I have averaged over 10 oscillations, and therefore $\Delta T = 0.001/10 = 0.000\,1\,\mathrm{s}$.

The uncertainty in determining the spring constant using the frequency method is less than 0.5%, which is much less than the uncertainty involved when using equation 2.2 to calculate the spring constant (9%). To minimise the fractional uncertainty in k, the spring constant should be determined from its natural frequency.

2.2.3 Uncertainty in force measurements

So far, we have only considered the uncertainty involved in determining the spring constant. To obtain the total fractional uncertainty in the force calculated from Hooke's law (equation 2.1), we also have to consider the uncertainty in the displacement. The fractional uncertainty arising from using Hooke's law to calculate forces is

$$\frac{\Delta F}{F} = \sqrt{\left(\frac{\Delta k}{k}\right)^2 + \left(\frac{\Delta x}{x}\right)^2}, \tag{2.7}$$

where $\Delta x/x$ is the fractional uncertainty in the measured deflection. Δx is given by the pixel size of the image, and x depends on the magnitude of the applied force and the spring constant of the blade.

The maximum value that x can take, $x_{\max}$, is given by the field of view of the objective lens. In general, objective lenses that have better resolution (smaller Δx) also have a smaller range (smaller $x_{\max}$). Therefore, it is not trivial which objective lenses give the smallest fractional uncertainty in the measured deflection. It turns out that $\Delta x/x$ is independent of the objective lens used when the spring constant of the blade is carefully chosen such that the maximum measured deflection spans the entire field of view of the objective. This can be understood as follows. Δx is determined by pixel size, that is $\Delta x = x_{\max}/N$, where N is the number of pixels in a length $x_{\max}$. If the blade is appropriately chosen such that the deflection spans almost the entire field of view of the objective,[4] then

$$\frac{\Delta x}{x} = \frac{\frac{x_{\max}}{N}}{x_{\max}} = \frac{1}{N}. \tag{2.8}$$

With the Leica TCS SP8, the maximum value that N can take is 8192 and this is independent of the type of objective lens used. Therefore, the lowest fractional uncertainty that can be obtained is $\Delta x/x = 1/8192 \approx 0.01\%$, independent of the objective lens. The fractional uncertainty in x is negligible compared to the fractional uncertainty in k.

2.2.4 Noise level

Random fluctuations occur due to ambient vibrations and air drafts in the vicinity of the setup. These random fluctuations can be quantified by measuring fluctuations

[4] In practice, I do not use the entire range, but around half to three-quarters of it. But this does not significantly affect the estimate in equation 2.8.

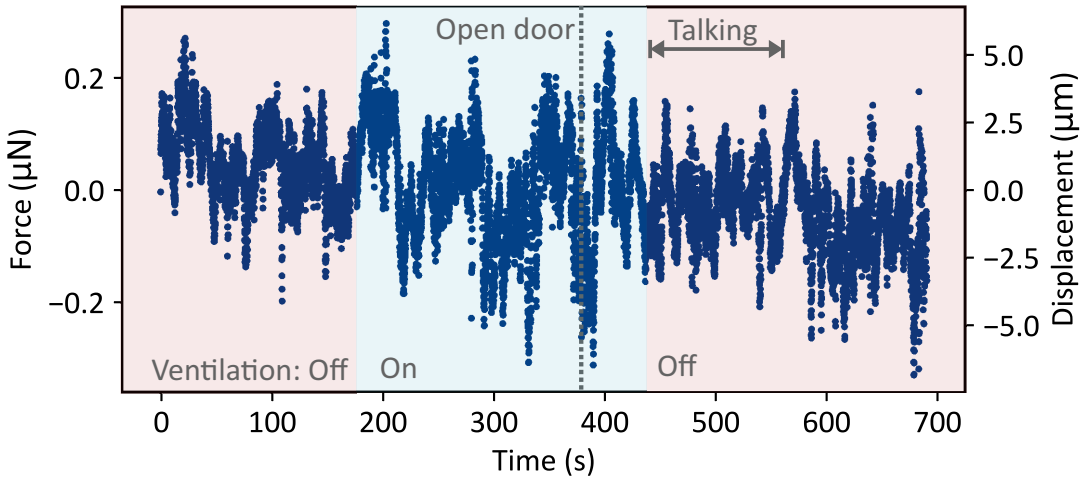

Figure 2.6: Random noise due to ambient vibrations. The standard deviation of the noise is 0.1 µN.

in the displacement of the bottom edge of a freely handing blade (figure 2.6). The standard deviation of the noise was 0.1 µN, which is negligible compared to the forces measured in this thesis. Therefore, the random noise due to ambient vibrations can be safely neglected. However, these fluctuations will become important when using low-friction surfaces, such as superhydrophobic or liquid-infused surfaces. When measuring drop friction on extremely low-friction surfaces, the random noise can be minimised by enclosing the setup in a draft-free environment.

2.2.5 Applying the method to study drop dynamics

A typical measurement When measuring the friction force between a drop and a surface, the drop is positioned on the surface, in front of the blade (figure 2.7, position 0). Then, the surface is set in motion and the drop moves together with the surface until it reaches the blade. Upon initial contact, the blade is attracted to the drop as the liquid partially spreads on the blade. This 'snap-in' is seen as a sharp dip in the force curve (point 1-2). In principle, snap-in force would be zero when using a perfectly superhydrophobic blade (contact angle of 180° with the drop).

After snap-in, the drop continues to move together with the surface, pressing against the blade. As a result, the force increases, reaching a maximum at point 4. At point 4, the distortion of the drop reaches a maximum and the force is equal to the static friction, F_S [48]. Beyond point 4, the drop starts moving in steady state relative to the surface and its shape relaxes to a less distorted state. The force plateaus to steady value, termed the kinetic friction, F_K [48].

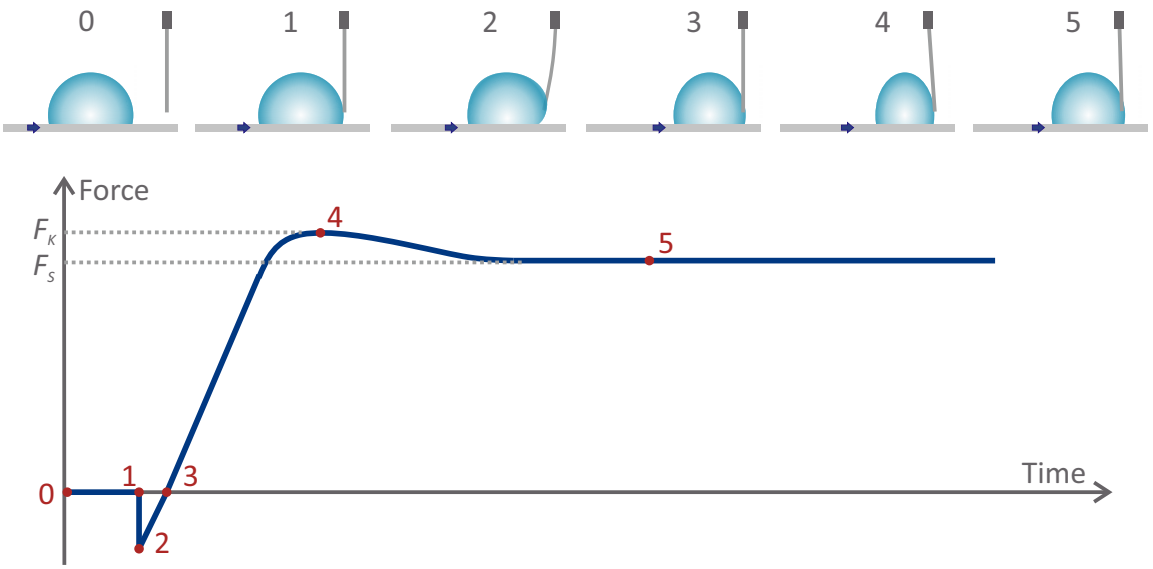

Figure 2.7: Schematic of a typical force curve on an ideal surface. Note that in some cases, F_S can be equal to F_K.

Motion at constant speed During all the force measurements, the drop is fixed by the blade while the surface moves at constant speeds between $1\,\mu m\,s^{-1}$ and $2\,cm\,s^{-1}$. The motion of the surface is controlled using a LabVIEW program.[5] Moving the surface while keeping the drop fixed is equivalent to moving the drop while keeping the surface stationary. These two scenarios are related by a Galilean transformation, and therefore the same force needs to be applied in both cases.

Moving the surface while keeping the drop fixed is advantageous since it allows the force to be monitored over an extended time. The blade's position can only be imaged if it remains within the field of view of the stationary objective lens. If the surface is fixed and the blade (and drop) is moved, then the blade will eventually move out of the field of view of the objective lens (after 1.55 mm for the 10x objective). But by fixing the blade (and drop) above the objective lens and moving the surface, it is possible to record the blade's deflection continuously.

The concept of fixing the drop while moving the surface to measure drop friction has been reported by previous studies. Pilat *et al.* (2012) [86] and Gao *et al.* (2018) [48] used a glass capillary to hold the drop and a home-built laser system to measure the deflection of the blade, whereas Daniel *et al.* (2017) [31] used an acrylic capillary to hold the drop and a camera to measure the deflection. The notable advantage of the setup that I have introduced over existing setups is that with the LSCM setup, it is also possible to microscopically image the three-phase contact line from below during motion. Microscopic imaging combined with force measurements will be particularly insightful when investigating particle removal in chapter 5.

[5]Thanks to Alexander Saal for writing the LabVIEW program.

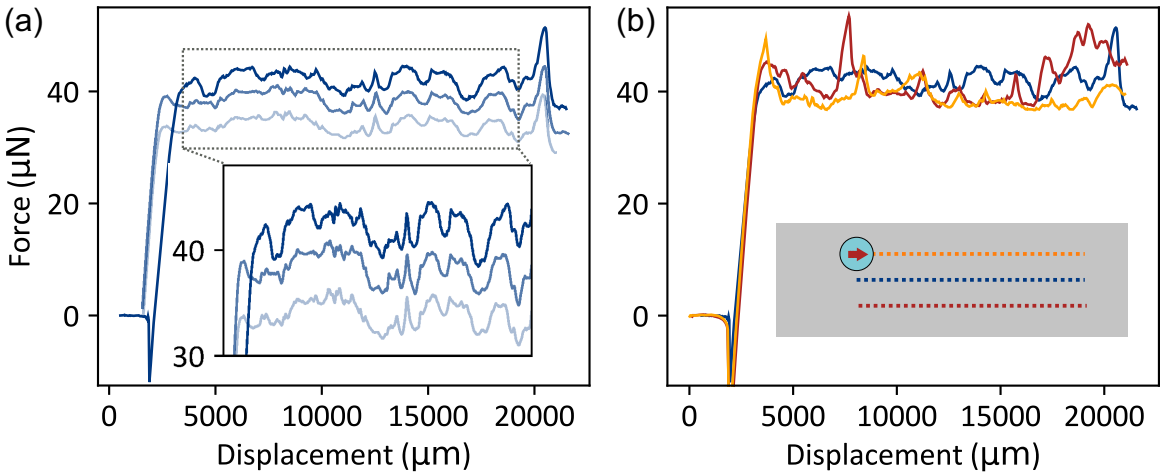

Figure 2.8: Friction force between a water drop and a PDMS surface. (a) Force required to move a 3 µL water drop at 200 µm s^{-1}. The three measurements were performed along the same track, with the same drop. The topmost curve corresponds to the first run and the bottommost curve correspond to the third run. The decrease in the force between the successive runs is due to a decrease in drop volume due to evaporation. (b) Force required to move a 3 µL water drop along three different tracks on the PDMS surface. A fresh drop was used for each measurement.

Reproducibility of measurements I performed two types of experiments to test the reproducibility of the setup. In the first type of experiment, the drop was held by the blade while the surface moved at 200 µm s^{-1} for $\approx$ 100 s. Then, the surface was moved backwards to bring the drop back to its starting position and the experiment was repeated with the same drop along the same track. The shape of the force curves was highly reproducible [figure 2.8 (a)]. The fluctuations due to surface inhomogeneities were consistent for all the runs, demonstrating that the force resolution is sufficient for studying PDMS surfaces.

In the second type of test experiment, a drop was moved along different tracks on the surface [figure 2.8 (b)]. Each run was performed using a fresh drop at a speed of 200 µm s^{-1}. Each track had a different distribution of surface inhomogeneities, which resulted in force curves that looked noticeably different. However, the average force was consistent for all the force curves. Note that the fluctuations due to surface inhomogeneities (few µN) are much more significant than the noise level due to ambient vibrations (0.2 µN, figure 2.6), thus validating the previous claim that the ambient noise can be neglected (section 2.2.4).

2.2.6 Practical considerations

There are a number of additional factors that need to be considered when using a blade to measure forces. The most important ones are described below.

2.2.6.1 Compromise between spatial and temporal resolution

Although the best spatial resolution in the deflection is obtained by choosing the largest number of pixels (N in equation 2.8), this is usually not be the optimal setting. When selecting the optimal value for N, the temporal resolution also has to be considered. For a fixed scanning speed, the temporal resolution is inversely proportional to the spatial resolution. Therefore, when studying problems that require a high temporal resolution, it is preferable to reduce the spatial resolution.

In general, using the highest spatial resolution is not necessary because even for relatively low spatial resolutions, the fractional uncertainty in the deflection tends to be negligible for most practical purposes.[6] For example, a 50 times reduction in the spatial resolution from the highest setting of 8192 pixels leads to a fractional uncertainty of only $\Delta x/x \approx 50/8192 \approx 2\%$, which is negligible for most practical purposes. For a fixed scanning speed, this loss in spatial resolution is compensated by a 50 times increase in temporal resolution. For most all cases, a 50 times increase in temporal resolution is a lot more valuable than a 2% improvement in spatial resolution.

2.2.6.2 Effect of finite drop size

The spring constant determined using the methods presented in section 2.2.2 is valid when the force is applied precisely at the bottom edge of the blade. When pushing drops, the force, F_{drop}, acting on the blade is not localised at the bottom edge, but is distributed over circular/elliptical area. Consequently, the moment produced by F_{drop} is smaller than if it was localised exactly at the bottom edge. Therefore, the apparent force measured by the blade is

$$F_{\text{app}} = F_{\text{drop}} \frac{l - r}{l}, \tag{2.9}$$

where l is the length of the blade. r is the distance between the bottom edge of the blade and the position where the force exerted by the drop on the blade is centred. This effect introduces an additional error (in addition to equation 2.7) in the force measurements:

$$\frac{\Delta F}{F} = \frac{r}{l} \approx \frac{1 \text{ mm}}{50 \text{ mm}} = 2\%. \tag{2.10}$$

Here, I have taken r to be equal to the radius of a typical drop used in a drop friction experiment. Therefore, the measured force is systematically lower than the actual force. However, the difference is only 2%, which is negligible for the purpose of this thesis.

[6] This statement applies when using a highly sophisticated laser system like the one in the Leica TCS SP8 microscope. The argument might not hold when using devices that offer lower spatial resolutions.

The total systematic uncertainty in the force measurements is $\approx 2\%+2\%+0.3\% \approx 4\%$, where the contributions are due to (1) the uncertainty in measuring the deflection of the blade, (2) the error due to the finite drop size, and (3) the uncertainty in determining the spring constant. As an example, the friction force that a drop (volume 5 µL) experiences when moving on a PDMS surface is typically between 50 µN and a few 100 µN, depending on the speed. Therefore, the systematic uncertainty in the force is $\Delta F \approx 2\,\mu\text{N}$ (for $F = 50\,\mu\text{N}$).

2.2.6.3 Long and relatively thick blades are better

Thick blades (*e.g.* thickness 40 µm-70 µm) have the advantage of remaining straight after being cut into the right dimensions. In contrast, thin blades (thickness $< 40\,\mu\text{m}$) tend to coil, are less sturdy and are more prone to getting damaged when being mounted on the microscope.

However, thicker blades also have higher spring constants (equation 2.2). A higher spring constant results in a lower deflection for the same applied force since $x = F/k$. To ensure that the deflection is sufficiently large to be measured precisely, the spring constant can be tuned by increasing the length of the blade. The longer the blade, the smaller the systematic error due to the finite drop size effect (equation 2.9). The longest blade that can be mounted in the limited space on the Leica TCS SP8 microscope is around 10 cm.

2.2.6.4 Blade width

When measuring drop friction with the confocal microscope, zero force corresponds to the position of the blade before it makes contact with the drop. To obtain the position of zero force and the drop friction in a single measurement, the width of the blade should be wider than the drop, and the drop, laser and blade should be aligned appropriately. The reason for this can be understood by considering a typical drop friction measurement.

Initially, the drop starts a few millimetres in front of the blade. The objective lens focuses on the bottom edge of the blade. Then, the recording starts and the sample starts moving at constant speed. When the blade and drop make contact, there are two possibilities: (1) the drop gets in the way of the laser beam [figure 2.9 (a)], or (2) the drop does not disrupt the optical path of the laser beam [figure 2.9 (b)].

If scenario (1) occurs, the optical path of the laser is disrupted due to the difference between the refractive index of the drop and that of air. When the laser travels through the drop instead of air, the apparent position of the bottom edge of the blade shifts out of focus, causing the reflection signal to disappear. In this case, the position of the blade cannot be monitored continuously. If the width of the blade is less than the diameter of the drop, scenario (1) is unavoidable. In this case, the zero position has to be calibrated beforehand, without the drop. Once the zero position is

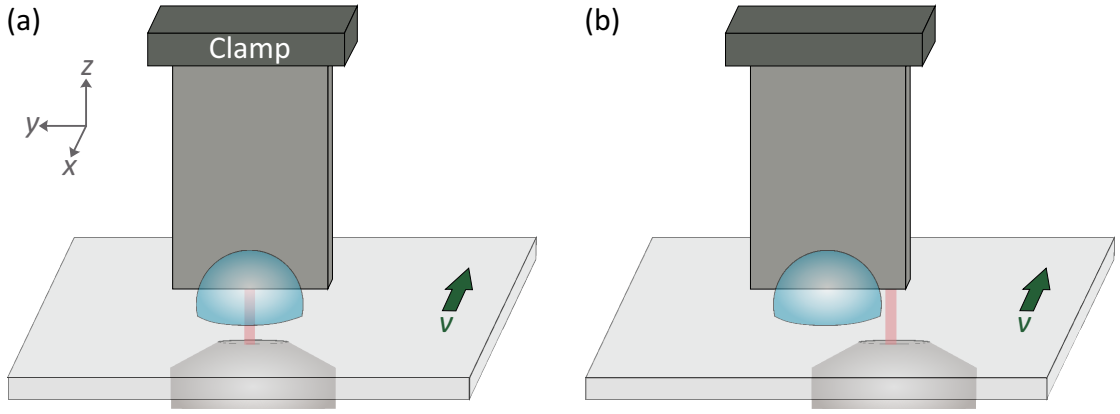

Figure 2.9: In this schematic, the drop is being pushed by the blade while the surface moves into the plane of the paper (along $-x$). (a) If the laser is positioned such that it goes through the drop, the reflection signal disappears when the drop makes contact with the blade since the refractive index of the drop differs from that of air. (b) In contrast, the deflection can be measured continuously when the drop and the laser are aligned such that the laser does not go through the drop.

recorded, the drop is brought in contact with the blade and the focus is readjusted. Finally, the measurement is started by moving the stage at constant speed.

In contrast, with scenario (2), the position of the blade can be recorded continuously because the the laser travels through a single medium (air) throughout the entire measurement. To achieve scenario (2), the width of the blade has to be greater than the diameter of the drop and the drop has to be appropriately aligned such that it does not get in the way of the laser beam.

When using blades wider than the diameter of the drop, the drop and the blade should carefully be aligned such that the drop is centred on the blade [figure 2.9 (b)]. This ensures that there are no twisting effects, which could result in erroneous measurements. However, twisting effects were negligible for the blades that I used, even when the drop was not centred exactly at the middle of the blade.

2.2.6.5 Influence of blade on force measurements

The surface properties (hydrophobicity/hydrophilicity) of the blade influence the shape of the drop and therefore the contact width between the drop and the surface. Since drop friction is proportional to the contact width (equation 1.21), different types of blades will provide different absolute values for the friction force. For consistent comparison, it is crucial that the surface properties of the blade remain constant throughout all measurements. However, this can be experimentally challenging when using polydimethylsiloxane (PDMS) surfaces. As I will describe in the next chapter, water drops get covered by a layer of PDMS as they move relative to a PDMS surface. Consequently, some of the PDMS is also transferred to the blade, causing it to become more hydrophobic. There are two ways to overcome this problem.

One approach is to chemically functionalise the blade with PDMS, such that the blade is already hydrophobic before the measurements. The second approach is to normalise the measured friction force by the drop-surface contact width. The normalised force is independent of the drop's size and of the contact area between the drop and the blade (equation 1.21). Obtaining the contact width is straightforward when using the LSCM setup. Each measurement is performed twice: first focusing on the blade edge to measure the force, and then on the drop-surface contact to measure the width.

2.3 Surface pendant drop method

Drops may adsorb contaminants when they are in contact with solid surfaces. The presence of contaminants on the surface of a drop may cause its surface tension to change. To investigate how fast and by how much the surface tension of a drop changes when it is placed in contact with a surface, I developed the surface pendant drop method. Before describing this method, I will give an overview of the standard pendant drop method.

2.3.1 Background on the standard pendant drop method

With the standard pendant drop method, a drop is suspended vertically from a syringe needle. The shape of the drop is governed by the gravitational force and the capillary force acting on the drop. The surface tension of the liquid is determined by fitting the Laplace equation (equation 1.6) to the drop's profile [13]. The Laplace equation (including gravity) is given by

$$\gamma\left(\frac{1}{R_1}+\frac{1}{R_2}\right)=\Delta P\equiv\Delta P_0-\Delta\rho g z, \tag{2.11}$$

where R_1 and R_2 are the principle radii of curvature of the drop, $\Delta P=P_{\text{drop}}-P_{\text{air}}$ is the Laplace pressure across the drop-air interface, and $\Delta\rho=\rho_{\text{drop}}-\rho_{\text{air}}$ is the density difference between the drop and the surrounding phase (air). $\Delta\rho g z$ is the hydrostatic pressure. $g=9.81\,\text{m}\,\text{s}^{-2}$ is the acceleration of free-fall. $\Delta P_0=2\gamma/R_0$ is the Laplace pressure evaluated at the drop's apex ($z=0$), where R_0 is the radius of curvature at the apex. Since the drop is axisymmetric, the radii of curvature is given by [13]

$$\left(\frac{1}{R_1}+\frac{1}{R_2}\right)=\frac{z'}{x(1+z'^2)^{1/2}}+\frac{z''}{(1+z'^2)^{3/2}}, \tag{2.12}$$

where $z'=dz/dx$ and $z''=d^2z/dz^2$. Inserting equation 2.12 into equation 2.11 gives

$$\gamma\left(\frac{z'}{x(1+z'^2)^{1/2}}+\frac{z''}{(1+z'^2)^{3/2}}\right)=2\frac{\gamma}{R_0}-\Delta\rho g z$$

$$\frac{\bar{z}'}{\bar{x}(1+\bar{z}'^2)^{1/2}}+\frac{\bar{z}''}{(1+\bar{z}'^2)^{3/2}}=2-Bo\ \bar{z}, \tag{2.13}$$

where $Bo=\Delta\rho g R_0^2/\gamma$ is the dimensionless Bond number, $\bar{z}=z/R_0$ and $\bar{x}=x/R_0$. Equation 2.13 is fitted to the contour of a pendant drop (imaged experimentally), with Bo as a fitting parameter. The value of Bo which provides the best fit to the drop contour is extracted. Finally, γ can be calculated, provided that $\Delta\rho$ is known.

Practical considerations Typically, a shadow image of the drop is taken using a camera. The drop's contour is extracted from the image using an edge detection algorithm. The resolution of the camera, the pixel-to-length calibration and the effectiveness of the edge detection algorithm determine the accuracy of the calculated surface tension. To minimise the measurement uncertainty in γ due to the fitting procedure, the drop volume V_d should be as close as possible to the maximum volume at which it detaches from the needle:

$$V_\mathrm{max}\approx\frac{\pi D_\mathrm{n}\gamma}{\Delta\rho g}, \tag{2.14}$$

where D_n is the diameter of drop at the tip of the needle. This expression is only approximate (although a good one) because in reality the drop does not always detach exactly at the needle tip. Instead, it ruptures at its thinnest position, which can be below the tip. The % relative standard deviation in determining γ scales as $\%RSD\sim(V_\mathrm{max}/V_\mathrm{d})^2$ [13].

2.3.2 Surface pendant drop setup

The surface pendant drop method is an alteration of the standard pendant drop method. The drop is suspended from a surface rather than from a needle (figure 2.10). I describe a typical experiment below.

Holes of diameter 2 mm are drilled into the surface. The surface is then placed on two supports as shown in figure 2.10. It is positioned such that a syringe tip lies directly above the hole. The outer diameter of the syringe tip (1.8 mm) is almost equal to, but slightly smaller, than the hole (2 mm).

Automated step-by-step procedure For consistent drop deposition, the following procedures were automated using a Krüss Drop Shape Analyzer (DSA100). The drop volumes listed below are relevant for water drops on PDMS surfaces. The settings need to be adjusted depending on the specific system under investigation.

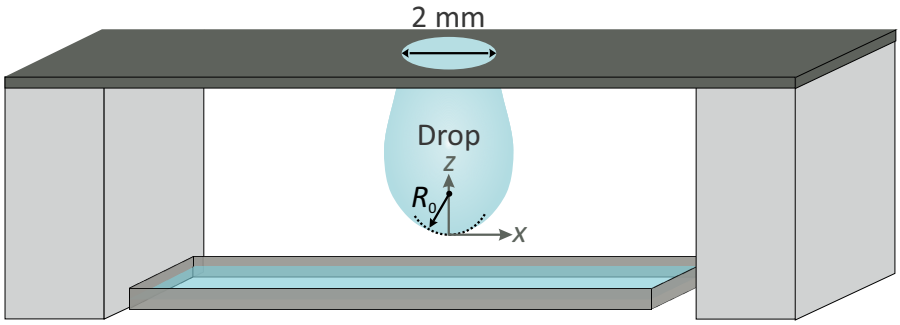

Figure 2.10: Schematic of the surface pendant drop setup. The drop's three-phase contact line is pinned at the hole. The drop's contour is monitored over time and the surface tension is extracted by fitting the Laplace equation (equation 2.13) to the drop's contour. The water bath at the bottom is added to slow down the evaporation of water drops.

1. The syringe tip is lowered through the hole until it is a few millimetres below the surface.

2. 25 µL of ultrapure water is dosed at $3\,\mu L\,s^{-1}$.

3. After waiting for 10 s for any vibrations from the dosing to subside, the surface tension is measured, with the drop hanging from the syringe tip. This is to check whether the initial surface tension of the water drop corresponds to the expected value of $72\,mN\,m^{-1}$.

4. The syringe is moved upwards until the drop touches the surface.

5. The drop volume is increased to 38 µL at $5\,\mu L\,s^{-1}$. 38 µL corresponds to the maximum drop volume that can be supported by a contact line having a diameter of 2 mm, assuming that the effective surface tension of the drop decreases to $\approx 60\,mN\,m^{-1}$. Since larger drops lead to more precise surface tension measurements, the drop has to be as large as possible, but smaller than the critical size at which it falls.

6. The surface tension is measured at a frequency of 1-10 Hz. The chosen frequency depends on how fast the change in surface tension is expected to take.

7. At the end of the experiment, the syringe tip is pulled out of the drop. The surface tension of the drop is measured again, without the tip attached to it. This is to check if the presence of the syringe tip was influencing the measurement.

The surface pendant drop method is suitable for liquids that do not significantly wet the surface. If the liquid completely spreads on the surface, it will not be possible to keep the drop pinned since it will spread past the hole.

2.4 Summary

In section 2.2, I presented a method to measure horizontal forces using an inverted laser scanning confocal microscope. With this method, it is possible to image dynamic processes with microscopic resolution (300 nm lateral, 1 µm axial) and to measure friction forces with a resolution of 200 nN (limited by noise). This method will be used to investigate how drops remove particles from surfaces in chapter 5.

In section 2.3, I introduced the surface pendant drop method to quantify how fast and by how much the surface tension of drops change as they accumulate contaminants from a surface. This method will be used in the next chapter.

Chapter 3

Wetting of silicone surfaces

In this chapter, I investigate the static and dynamic wetting properties of water on silicone elastomers.

Silicone elastomers are widely used for medical implants, sealants, lab-on-a-chip studies and cell cultures. In the field of wetting, they are often used as model surfaces. In general, silicone elastomers consist of a silicone backbone with two organic side chains ($-R_2Si-O-SiR_2-$, where R is an organic group). I used polydimethylsiloxane (PDMS), which contains methyl groups as side chains. PDMS is known for being hydrophobic, unreactive, stable, and resistant to a wide temperature range. Most PDMS elastomers are gels, which consist of a crosslinked polymer matrix containing a small fraction of uncrosslinked chains. Uncrosslinked chains refer to polymers chains that are not covalently bonded to the crosslinked matrix.

In many applications, PDMS surfaces come into contact with liquids. It has been hypothesised that when the spreading parameter of PDMS on the liquid is positive, the uncrosslinked chains separate from the crosslinked matrix and contaminate the liquid [63, 64, 109]. This phenomenon will influence highly precise experiments and applications where contamination is strictly undesirable. However, so far, there is no direct visualisation of the effect and no direct measurement quantifying how fast uncrosslinked chains accumulate on drops that are in contact with the surface. These are explored in this chapter.

The knowledge gained in this chapter will be relevant in chapter 5, where PDMS surfaces will be used as model surfaces to study the removal of particles using drops.

3.1 Materials

3.1.1 PDMS surfaces

PDMS surfaces were prepared by mixing Sylgard 184 (from Dow Chemical Company) in a ratio of 10 parts base to 1 part crosslinker. In some of the batches, fluorescent dye was added during mixing so that the PDMS could be imaged using laser scanning confocal microscopy. The mixture was then degassed as follows. A pump was

connected to a sealed oven (at room temperature) to create a vacuum. As the air pressure in the oven reduced, air bubbles in the mixture grew and floated to the top. Then, an inlet was opened to allow air to flow into the oven. The sudden increase in air pressure caused the bubbles to burst quickly. The process of pumping air out of the oven followed by the sudden opening of the inlet was repeated (usually around 3 times) until no more bubbles were seen in the PDMS mixture. Meanwhile, glass slides were rinsed with isopropanol, ethanol and water, then dried with a nitrogen gun. This step ensures that the glass slides are free from impurities such as fingerprints. The dry glass slides were placed in a 300 W oxygen plasma oven at 30 to 40 Pa for 5 min. The degassed mixture was spin-coated onto the clean glass slides at 1000 rpm for 60 s. Finally, the coated slides were placed in an oven (preheated) at 80 °C for 2 h or 15 h to allow the polymer chains to form a crosslinked network. The resulting thickness of the PDMS layer was around 50 µm. Note that, even after 15 h, not all the PDMS chains get crosslinked, but around 5% (by weight) remain uncrosslinked [109].

3.1.2 PDMS surfaces with added lubricant

Lubricated PDMS surfaces containing 5% added lubricant were prepared by mixing 5.00 g of Slygard 184 base, 0.50 g of crosslinker and 1.83 g (5%) of PDMS lubricant in a glass vial for 2 min. Two types of lubricants were used: a trimethyl siloxy terminated PDMS with a viscosity of 1000 cSt (from Alfa Aesar) and trimethyl siloxy terminated PDMS with a viscosity of 200 cSt (from Xiameter PMX-200, Dow). For the surface containing 25% lubricant, 5.50 g of lubricant was added instead of 1.83 g. The mixtures were degassed and spin-coated onto glass slides, as described in section 3.1.1. Finally, the coated glass slides were placed in an 80 °C oven (pre-heated) for 2 h.

3.2 Cloaking of static drops

Drops covered with a thin layer of an immiscible lubricant are said to be ‘cloaked’. Cloaking is thermodynamically favourable when the spreading parameter of the lubricant on the drop is positive (section 1.5). The spreading parameter of PDMS on water is

$$S = \gamma_{\mathrm{WA}} - \gamma_{\mathrm{LA}} - \gamma_{\mathrm{WL}} \approx (73 - 20 - 40)\ \mathrm{mN\ m^{-1}} = 13\,\mathrm{mN\,m^{-1}}.$$

Here, γ_{LA}, γ_{WL}, and γ_{WA} are the PDMS lubricant-air, water-PDMS lubricant, and water-air interfacial tensions, respectively. Since $S > 0$, water drops are expected to become cloaked when they are placed on surfaces containing uncrosslinked PDMS chains. In general, cloaking has several consequences. For example, on liquid-infused surfaces, cloaking is one of the causes of lubricant depletion, which consequently leads to a loss of functionality.

In the following, I will provide the first direct experimental proof of the cloak layer using laser scanning confocal microscopy. Then, I will use the surface pendant drop method described in section 2.3 to quantify the kinetics of cloaking on PDMS surfaces.

3.2.1 Direct observation

The cloak layer is not visible to the naked eye or to regular optical cameras due to its very small thickness and due to the lack of contrast between the drop and the lubricant. Advanced techniques such as interference microscopy, scanning electron microscopy or laser scanning confocal microscopy are required. Here, I used the latter.

On a liquid-infused surface containing PDMS oil as lubricant, drops were surrounded by both a wetting ridge and a cloak (figure 3.1). In this case, the wetting ridge was clearly visible (height $\approx 100\,\mu m$). However, a prominent wetting ridge is not required for there to be a cloak. On a PDMS (elastomer) surface, there is no visible wetting ridge, but a cloak is still present (figure 3.2).[1]

3.2.2 Kinetics

Although it is possible to nicely image fully cloaked drops using laser scanning confocal microscopy, it is tricky to use the technique to accurately quantify how long it takes for the cloak to form. However, since the surface tension of a drop is expected to change during cloaking [32, 94, 70, 64], the time taken for the drop to become cloaked can be determined by measuring its surface tension over time. Therefore, the kinetics of cloaking can be quantified using the surface pendant drop method described in section 2.3. In the following, I will describe experiments conducted using the surface pendant drop method and interpret the results.

With a PDMS surface without added lubricant, no change in surface tension was observed over 30 min.

With a surface containing 5% of added PDMS lubricant (200 cSt), the surface tension decreased by $\approx 8\,mN\,m^{-1}$ after around 15 min [blue dots in figure 3.3 (c)]. At the beginning of the measurements (time = 0), there is no PDMS on the drop's surface and therefore the initial surface tension corresponds to the value expected for pure water ($73\,mN\,m^{-1}$). Thereafter, uncrosslinked PDMS chains migrate from the PDMS surface to the air-water interface, thus reducing its surface tension to a final value of around $65\,mN\,m^{-1}$.

When a PDMS surface containing 25% of added lubricant (200 cSt) was used, the surface tension decreased by the same amount. However, the decrease was much

[1] No visible wetting ridge was seen within the vertical resolution of the confocal microscope (around 1 µm). However, a sub-microscopic wetting ridge should still be present.

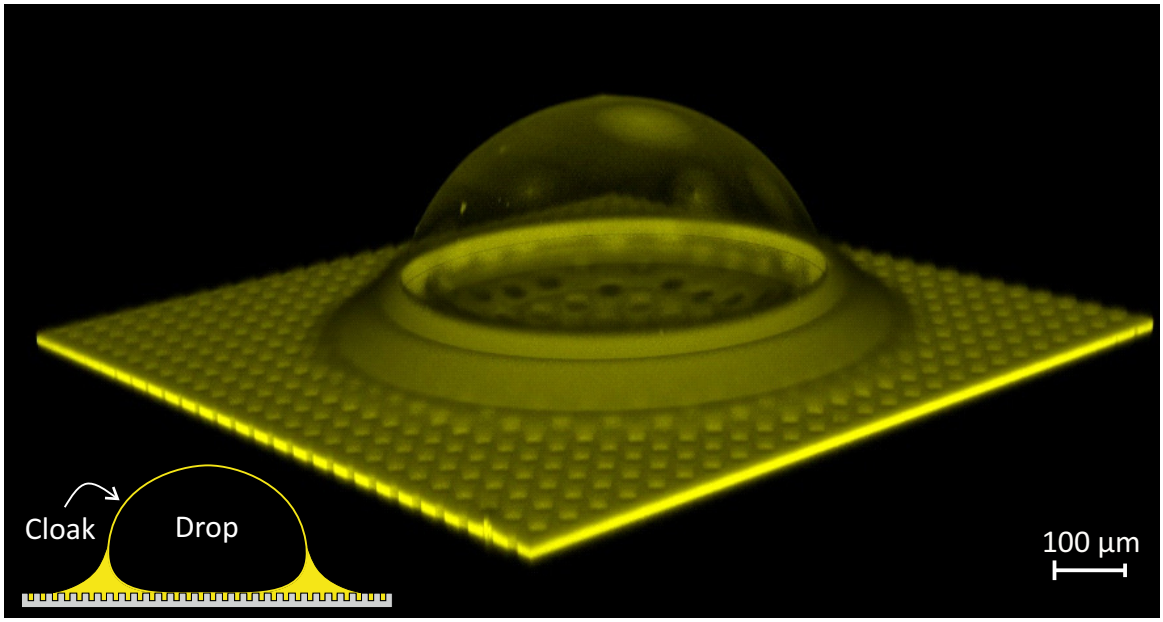

Figure 3.1: Cloaked drop on a liquid-infused surface. The solid surface consisted of an array of cylindrical pillars (diameter: 30 µm, height: 10 µm, centre-to-centre spacing: 60 µm). Only fluorescence from the lubricant (viscosity 1000 cSt) is shown in yellow. The drop contained 57% of glycerol and 43% water (by weight). Glycerol was added for two reasons: to suppress evaporation and to match the refractive index of the drop to that of PDMS. A ratio of 57:43 was chosen since it results in a refractive index of 1.41, which is equal to the refractive index of PDMS. Matching the refractive indices leads to better image quality since optical artefacts are reduced. The addition of glycerol to the drop does not change the sign of the spreading parameter.

faster, taking less than 20 s to reach the final plateau [green points in figure 3.3 (c)]. As the surface tension decreased, the drop became increasingly elongated. The corresponding evolution of the drop contour is shown in figure 3.3 (b), where the blue line corresponds to the contour before cloaking and the green line corresponds to the contour after cloaking.

When a PDMS surface containing a more viscous lubricant was used, it took longer for the surface tension to decrease. For example, when 25% of a 350 cSt lubricant was added instead of 25% of 200 cSt lubricant, it took around three times longer for the surface tension to decrease (figure 3.4).

Three main conclusions can be drawn from these experiments: (1) The addition of lubricant speeds up the cloaking process, (2) for the same amount of lubricant, cloaking is slower when a more viscous lubricant is used, and (3) the surface tension of a water drop cloaked with PDMS is around 65 mN m^{-1}. Interestingly, the surface tension remained constant for a finite amount of time before starting to decrease. This demonstrates that the surface tension is only affected when there is a sufficiently large amount of PDMS chains on the drop.[2]

[2]With the surface pendant drop method, only the average surface tension of the drop can be

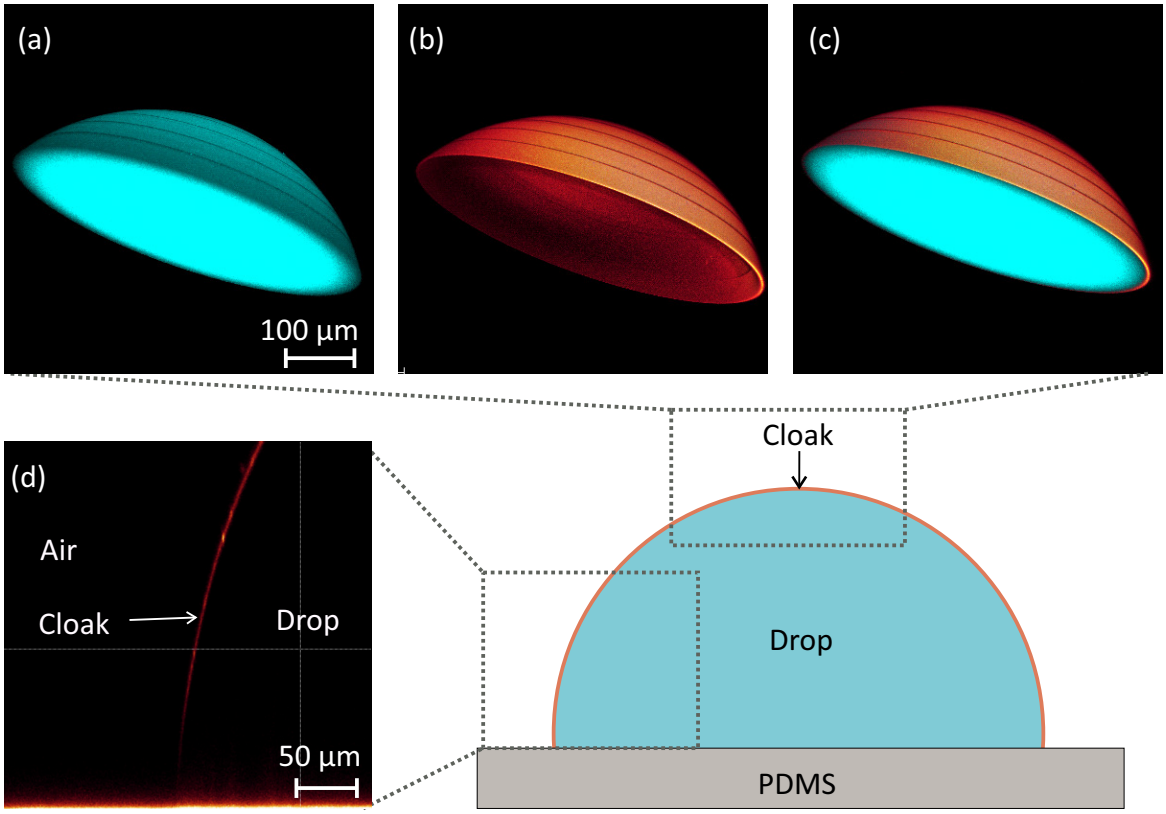

Figure 3.2: A cloaked drop (57% glycerol, 43% water) on a PDMS surface. The image was taken using confocal microscopy around 30 min after placing the drop on the surface. (a)-(c) Three-dimensional image of the top part of the drop. (a) shows fluorescence signal from the drop only, (b) shows fluorescence from PDMS only, and (c) is an overlay of (a) and (b). (d) is a side view showing fluorescence from PDMS. Note the absence of a prominent wetting ridge.

A related but more widely studied problem is the spreading of oil films on water. The surface of a cloaked drop is similar to the surface of a water bath that is covered by an oil film (e.g. in a Langmuir-Blodgett trough) because in both cases, there is a water-oil interface and an oil-air interface separated by an oil film. Indeed, The final surface tension a cloaked drop (65 mN m^{-1}) is comparable to the surface tension of a water bath covered by a flat silicone monolayer (63 mN m^{-1}) [74]. Below, I will review the topic of thin oil films on water and then apply the knowledge in the context of cloaking.

Background knowledge on oil films on water The study of oil films on the surface of water has been of interest since the 18th century (at least), with pioneering contributions from Benjamin Franklin (1774), Agnes Pockels (1891) and Lord Rayleigh (1899). Franklin [46] reported that when oil is dropped on the surface

obtained. Local changes in surface tension due to small PDMS patches on the drop's surface cannot be quantified. Therefore, we should only expect to see a change in surface tension when the drop is surrounded by a significant amount of PDMS.

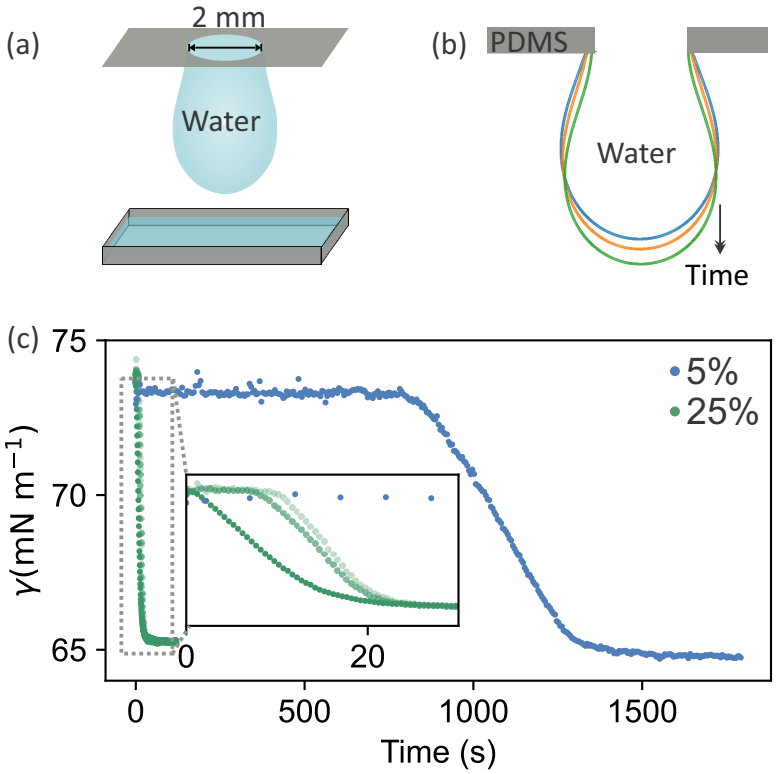

Figure 3.3: Change in surface tension of a water drop as it gets cloaked by PDMS (200 cSt). (a) Schematic of a drop hanging from a PDMS surface. The contact line is pinned by a hole. A water bath is placed below the drop to slow down evaporation. (b) Evolution of the drop profile during cloaking. (c) Change in surface tension of the drop over time on PDMS surfaces containing 5% of added lubricant (blue) and 25% of added lubricant (green).

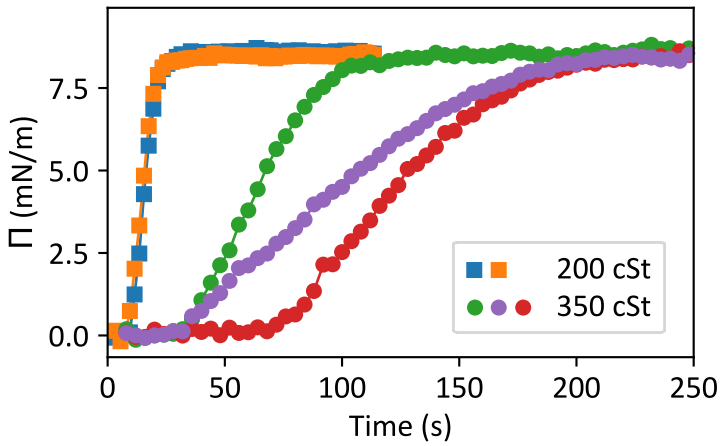

Figure 3.4: Change in surface pressure, $\Pi(t) = \gamma(t) - \gamma(0)$, over time during cloaking of water drops on two types of PDMS surfaces. Both surfaces contained 25% of lubricant. The only difference was that the lubricant had different viscosities. The blue and orange squares correspond to a 200 cSt lubricant, whereas the green, purple and red circles correspond to a 350 cSt lubricant. It took noticeably longer for drops to become cloaked on the 350 cSt surface.

.

of a large reservoir of water, such as a lake, it quickly spreads and calms down the waves over an extended area. Pockels [89] and Rayleigh [90] systematically varied the concentration of oil on the surface of water and measured the surface tension of the interface. Pockels demonstrated that the surface tension is independent of the oil concentration below a critical concentration. However, above that critical concentration, the surface tension becomes sensitive to the concentration of oil present on the surface.

Highly precise measurements of the surface tension of water as a function of the surface concentration of PDMS oil were performed in the 1990s by Lee *et. al* [74]. They showed that below a surface concentration of $C \approx 0.6\,\mathrm{mg\,m^{-2}}$,[3] PDMS has no influence on the surface tension of water, which remains equal to that of pure water. However, the surface tension decreased when C was increased to $C_{\mathrm{th}} \approx 0.75\,\mathrm{mg\,m^{-2}}$. By using ellipsometry to measure the thickness of the oil layer, they showed that the water surface was only partially covered by PDMS patches below C_{th}. But when the surface concentration of oil reached C_{th}, the water surface was completely covered by a PDMS monolayer. As the surface concentration of oil was increased even further, the molecules stacked up to form multilayers. However, the surface tension did not change further once the first complete monolayer had formed.

Mathematically, the influence of oil on the surface tension of an air-water interface can be described in terms of the surface pressure. When a very small amount of oil (a monolayer) spreads over the surface of a pure liquid, the surface tension of the liquid is reduced to

$$\gamma = \gamma_0 - \Pi, \tag{3.1}$$

where γ_0 is the surface tension of the bare liquid, and Π is the surface pressure. An intuitive way to think about the surface pressure is to consider the work required to change the area of the interface (e.g. in a Langmuir-Blodgett trough) by an amount dA:

$$dW = \gamma\ dA = \gamma_0\ dA - \Pi\ dA. \tag{3.2}$$

Here, $\gamma_0\ dA$ corresponds to the contribution from the bare interface and $\Pi\ dA$ is the contribution due to the monolayer. Therefore, $\Pi\ dA$ is the two-dimensional analogue of the work $P\ dV$ in bulk thermodynamics. A typical plot of Π against A at constant temperature (called a surface pressure isotherm) is sketched in figure 3.5. At low surface concentrations (large A), the oil molecules in the monolayer are effectively in a 'gaseous state' and the surface pressure is close to zero. As the surface area decreases, the surface concentration of oil molecules increases to form the so-called 'liquid expanded' and 'liquid condensed' phases. This results in an increase in the

[3] $0.6\,\mathrm{mg\,m^{-2}}$ is equivalent to adding a $0.6\,\mu\mathrm{L}$ drop of oil to an area of $1\,\mathrm{m^2}$.

surface pressure. Further compression leads to a solid phase, and finally, a collapsed phase when the surface pressure reaches a maximum (or equivalently, when the area per molecule reaches a minimum). In the collapsed state, molecules stack up and form multilayers. Even though the collapse state leads to the lowest surface tension and corresponds to the minimum energy state, it cannot usually be reached when oil allowed to spread freely onto a liquid without any forced compression. This is because the condensed phases are usually metastable states and the system generally settles at these metastable states.

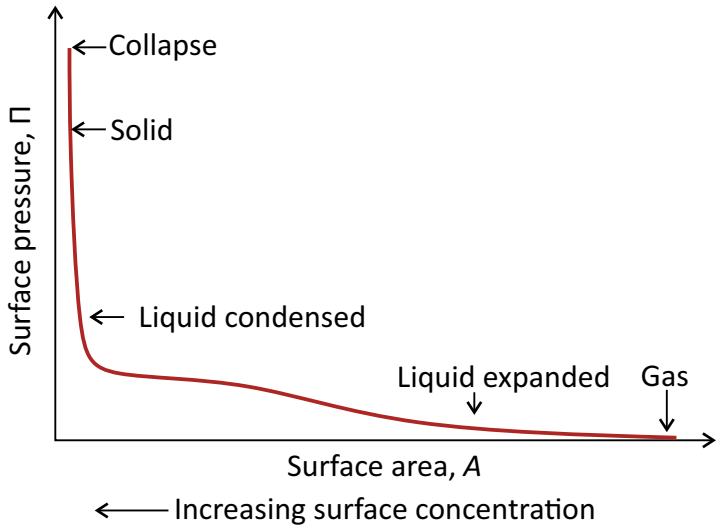

Figure 3.5: Surface pressure isotherm, redrawn from page 10 in reference [72].

Explaining the shape of the surface tension against time curve In the following, I will apply the concepts that I have introduced above to explain the different stages involved as water drops become cloaked on PDMS surfaces.

Since PDMS is insoluble in water, uncrosslinked chains cannot reach the air-water interface by diffusing through the bulk of the drop. The only possible pathway for PDMS to reach the surface of the drop is by migrating directly from the three-phase contact line to the air-water interface.

Following the results of Lee *et al.* presented above, the surface tension of the drop is not expected to change until the surface concentration of PDMS becomes large enough, such that the drop is covered by an almost complete PDMS monolayer. This explains why there is an initial plateau in the measurements shown in figure 3.3 (c). Initially, the PDMS chains that are on the surface of the drop are in the 'gas' phase (figure 3.5) and the surface pressure is zero. As the surface concentration of PDMS increases, the surface pressure increases and the surface tension of the drop decreases according to equation 3.1. Furthermore, Lee *et al.* showed that once a complete monolayer is formed, a further increase in the surface concentration of PDMS does not decrease the surface tension further. The cloaking experiments in figure 3.3 are

consistent with this description since the surface tension did not decrease further once the final plateau (at $65\,\mathrm{mN\,m^{-1}}$) was reached.

We can therefore draw two further conclusions on the cloaking process. First, the time taken for the surface tension of the drop to decrease depends on the time taken for a complete PDMS monolayer to form around the drop. Thus, by measuring the surface tension of the drop, we directly quantify the rate at which a PDMS monolayer forms around the drop. Second, the rate at which the monolayer forms increases as the fraction of uncrosslinked PDMS chains increases (figure 3.3) and decreases when the molecular weight (viscosity) of the PDMS chains increases (figure 3.4).

Mechanism and rate-limiting step The mechanism by which PDMS chains migrate from the PDMS surface to the air-water interface can be divided into two steps. In step 1, the PDMS chains diffuse from the bulk of the PDMS matrix to the three-phase contact line. Then, in step 2, these chains move from the contact line to the air-water interface. Which step is the rate-limiting step?

Step 1 depends on how fast uncrosslinked PDMS chains move within the PDMS matrix and therefore depends on the viscosity of the lubricant as well as the structure of the crosslinked PDMS matrix. In contrast, step 2 only depends on the viscosity of the lubricant because once the chains have reached the three-phase contact line, they only need to migrate to the air-water interface without having to travel through the crosslinked matrix.

Varying the amount of lubricant while keeping the viscosity constant (3.3) influences step 1, but not step 2. Since the surface tension took longer to change on the surface containing a lower fraction of lubricant, we can deduce that step 1 is rate-limiting. If step 2 was the rate-limiting step, the surface tension would have decreased equally fast on both surfaces. Therefore, the time taken for PDMS chains to reach at the three-phase contact line is longer than the time taken for them to move from the contact line to the air-water interface.

3.3 Contact angles of water on PDMS

When drops move on solid surfaces, they experience a friction force due to pinning of the three-phase contact line and due to dissipation (primarily at the contact line, section 1.12) arising from the no-slip boundary condition between the solid and the drop. In general, the friction force depends on the surface tension of the drop and on the advancing and receding contact angles (Θ_A and Θ_R) between the drop and the surface (equation 1.21).

In this section, I present measurements of the contact angles of water on PDMS surfaces, focussing on the influence of uncrosslinked PDMS chains on Θ_A. The model

by Butt *et al.* (2018) [23], which assumes that the surface adapts to the drop, provides the best fit to the data.

3.3.1 Advancing contact angle

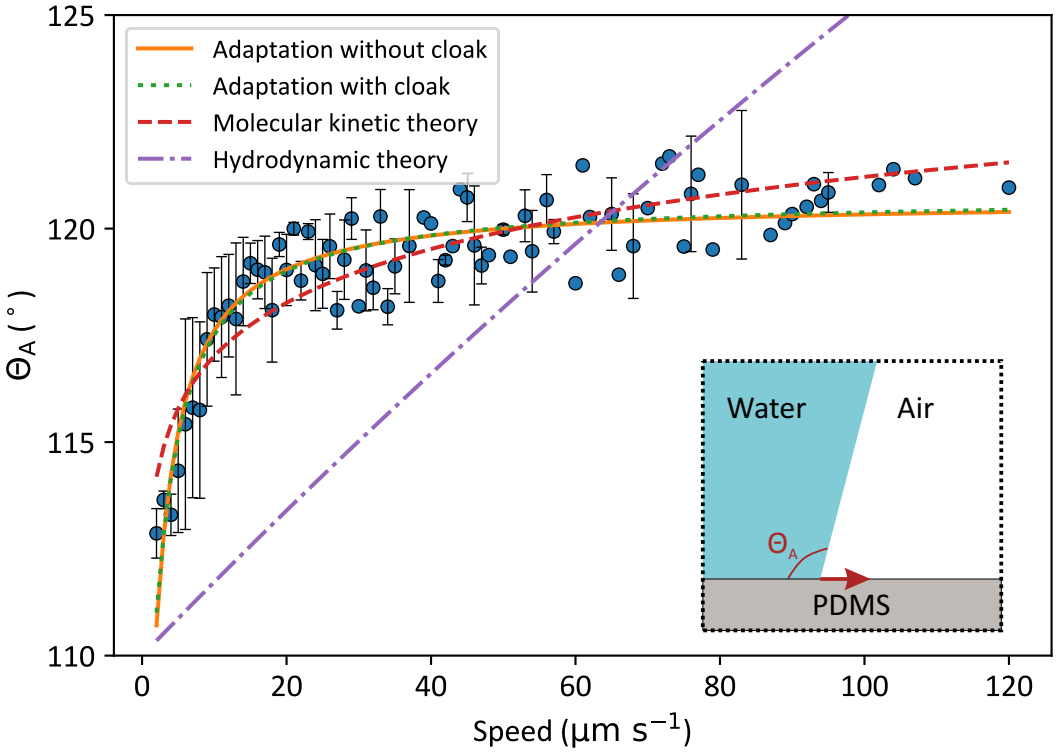

Figure 3.6: Contact angle of an advancing air-water interface on a PDMS surface as a function of the contact line speed. The data points are from [109]. The adaptation models are given by equation 3.7. 'Adaptation without cloak' assumes that $\gamma_{LV} = 73\,\mathrm{mN\,m^{-1}}$ and uses the following fitting parameters: $\nu = 2.2\,\mu\mathrm{m\,s^{-1}}$ and $\Delta\gamma_{SL} = -17\,\mathrm{mN\,m^{-1}}$. 'Adaptation with cloak' assumes that $\gamma_{LV} = 65\,\mathrm{mN\,m^{-1}}$ and uses the following fitting parameters: $\nu = 2.8\,\mu\mathrm{m\,s^{-1}}$ and $\Delta\gamma_{SL} = -13\,\mathrm{mN\,m^{-1}}$. The molecular kinetic theory is given by equation 1.39 with fitting parameters $\lambda = 2\,\mathrm{nm}$ and $K_0 = 86\,\mathrm{Hz}$. The hydrodynamic theory is given by equation 1.38 with $\ln(L_0/L_i) = 2.7 \times 10^5$ as the fitting parameter. $\gamma = 73\,\mathrm{mN\,m^{-1}}$ was used for the molecular kinetic and hydrodynamic theories. In all the models, I have used $\Theta_0 = 110°$ as the equilibrium (static) contact angle.

The experimental data presented in this section have been published in a study by Wong *et al.* (2020) [109], in which I was involved. I contributed to interpreting and modelling the data. In the following, I will summarise the experiments and the model that we used to interpret the data. The following discussion also includes considerations that have not been described in [109] because some of the arguments only occurred as afterthoughts, while I was writing this thesis. However, these afterthoughts strengthens the hypothesis that we proposed in [109].

Experiment A water drop was deposited on a PDMS surface [4] using a syringe. The drop was expanded by injecting water into the drop at a constant volumetric flow rate. As the volume of the drop increased, the three-phase contact line advanced. Θ_A was measured during this process. Each measurement is performed using a fresh drop on a fresh spot on the surface.

Results Θ_A is plotted as a function of the speed of the contact line in figure 3.6. At low speeds, Θ_A was around 112°. Θ_A increased with speed up to around 120° at a speed of $100\,\mu m\,s^{-1}$.

Interpretation The increase in Θ_A with speed is hypothesised to be due to two effects. First, there is a rearrangement of uncrosslinked PDMS chains in the PDMS matrix, which leads to a change in the solid-water interfacial tension. Second, the water molecules can only hop with a finite frequency (according to the molecular kinetic theory, section 1.12), thus resulting in a speed-dependent contact angle. In the following, I will elaborate on these processes, starting with the first effect.

Model for adaptation of the solid The model by Butt *et al.* (2018) [23] quantitatively describes how the contact angle changes as the solid surface adapts to the presence of the liquid. As a first order approximation (described by a single time scale), the rate at which γ_{SL} changes is given by

$$\frac{d\gamma_{SL}}{dt} = -\frac{\gamma_{SL} - \gamma_{SL}^{eq}}{\tau}. \tag{3.3}$$

Here γ_{SL}^{eq} is the final (equilibrium) surface tension of the solid-liquid interface (i.e. $\gamma_{SL}(t \to \infty)$ and τ is the so-called adaptation timescale, which is determined by how fast uncrosslinked chains can reach the three-phase contact line. Integrating equation 3.3 leads to

$$\gamma_{SL}(t) = \gamma_{SL}^{eq} + \Delta\gamma_{SL} \exp(-t/\tau). \tag{3.4}$$

Here $\Delta\gamma_{SL} = (\gamma_{SL}^{0} - \gamma_{SL}^{eq})$ is the difference between the initial and equilibrium solid-liquid interfacial tensions.

To see how changes in γ_{SL} influences the contact angle, we substitute equation 3.4 into the Young's equation (equation 1.13) to obtain

$$\cos\Theta(t) = \frac{\gamma_{SA} - \gamma_{SL}^{eq} + \Delta\gamma_{SL} \exp(-t/\tau)}{\gamma} \tag{3.5}$$

$$= \cos\Theta_0 + \frac{\Delta\gamma_{SL}}{\gamma_{LA}} \exp(-t/\tau), \tag{3.6}$$

[4] Sylgard 184, 10 parts base to 1 part crosslinker, as described in section 3.1.1 (crosslinked over 15 h at 80 °C).

where $\cos\Theta_0 = (\gamma_{SA} - \gamma_{SL}^{eq})/\gamma$ and γ is the drop-air interfacial tension. Θ_0 is the equilibrium contact angle between the drop and the surface when the system is given enough time to equilibrate.

To model the experiments in figure 3.6, it is instructive to write $\cos\Theta$ in terms of the speed of the contact line, v, rather than in terms of the time, t, that the contact line has spent in contact with the surface. t can be written in terms of v by introducing a length scale, l, which we call the peripheral length. The peripheral length can be understood as the size of the region (around the contact line) that influences the contact angle. Only uncrossliked chains that are within a distance l from the contact line influence the contact angle. Chains that are further than l have a negligible influence on the contact angle. To obtain $\cos\Theta$ in terms of v, we substitute $t = l/v$ in equation 3.6:

$$\cos\Theta(v) = \cos\Theta_0 + \frac{\Delta\gamma_{SL}}{\gamma_{LA}} \exp(-\nu/v), \tag{3.7}$$

where $\nu = l/\tau$ is the characteristic velocity at which the uncrosslinked chains readjust.

We can now use equation 3.7 to fit the experimental data points in figure 3.6 directly. The green and orange curves are the fits obtained using equation 3.7 with $\Theta_0 = 110°$, which corresponds to the contact angle when the drop is allowed to rest on the surface for a long time. The orange curve assumes that the drop's surface is not cloaked with PDMS and therefore has a surface tension equal to that of pure water, $\gamma = 73\,\mathrm{mN\,m^{-1}}$. The green dotted curve assumes that the drop's surface is fully cloaked with PDMS and therefore has a surface tension equal to $\gamma = 65\,\mathrm{mN\,m^{-1}}$. Both the orange and green curves provide good fits to the data. They both predict that the solid-liquid interfacial tension decreases when the surface is given enough time to adapt to the presence of the drop ($\Delta\gamma_{SL} = -17\,\mathrm{mN\,m^{-1}}$ for the orange curve and $\Delta\gamma_{SL} = -13\,\mathrm{mN\,m^{-1}}$ for the green curve).

Why does the presence of the water drop cause γ_{SL} to change? We hypothesise that a decrease in γ_{SL} is due to the rearrangement of PDMS chains from the bulk of the PDMS matrix to the vicinity of the contact line. Why do the chains rearrange? This is due to two effects: (1) there is vertical stress which pulls the PDMS surface (including uncrosslinked chains) upwards at the three-phase contact line,[5] (2) it is favourable for the PDMS chains to rearrange under the drop in order to lower the surface energy. For example, this could involve the readjustment of the uncrosslinked (mobile) chains such that their hydrophilic groups face the water drop.

Even though the measured trend can be explained by a variation in γ_{SL}, this does not necessarily mean that this is the only interpretation. To show why γ_{SL} is most likely the dominant parameter controlling the change in contact angle, I consider

[5] A vertical stress is due to the vertical component of the drop-air interfacial tension, see section 1.6.

other possible explanations below and discuss why they do not provide an adequate description.

Why not γ_{SA}? How can we know that the variation in contact angle is caused by γ_{SL} and not by γ or γ_{SA}? After all, as uncrosslinked chains migrate to the contact line, it is likely that γ and γ_{SA} also change in the vicinity of the contact line. Note that if γ and γ_{SA} change at all, they will decrease (rather than increase) because the system will always try to equilibrate to a lower energy state.

Since a decrease in γ_{SA} (at constant γ and γ_{SL}) causes the contact angle to increase (according to Young's equation), γ_{SA} cannot explain the observed trend. If γ_{SA} changed significantly in the peripheral length region, we would have observed the opposite trend to what is shown in figure 3.6. The contact angle at low speeds would have been higher than those at high speeds.

Why not γ? There are two reasons why the variation of the contact angle cannot be explained by a change interfacial tension of the liquid-air interface (cloaking). The first reason is that a decrease in γ at constant γ_{SA} and γ_{SL} causes the contact angle to increase. Therefore, if cloaking was responsible, the contact angle at low speeds should be higher than that at high speeds. This is opposite to what is observed experimentally. The second reason is that a $8\,\mathrm{mN\,m^{-1}}$ decrease in γ (due to cloaking, section 3.2.2) produces a negligible change in the contact angle.[6] This can be seen in figure 3.6, where the green (dotted) and orange (solid) curves barely differ. Hence, cloaking cannot explain the $> 5^\circ$ change in the macroscopic contact angle.

Viscoelastic dissipation in the wetting ridge Wetting ridges are usually a dominant source of dissipation and may therefore influence the contact angle. To check for the presence of a wetting ridge, we imaged the contact line using confocal microscopy with a resolution of 1 µm. However, no wetting ridge was seen [figure 3.2 (d)]. This demonstrates that the size of the wetting ridge is smaller than 1 µm. Due to its negligible size, the wetting ridge is unlikely to be a significant factor affecting the contact angle.

Hydrodynamic and molecular kinetic theories Can the trend in the contact angle be explained using the hydrodynamic theory or the molecular kinetic theory which both predict a speed-dependent contact angle, but assume that the properties of the solid do not change? From figure 3.6, the hydrodynamic theory (equation 1.38)

[6]Note that the cloaking timescale measured in section 3.2.2 cannot be used to estimate how fast γ changes in the context presented here. In section 3.2.2, the time taken for the entire drop to be cloaked was measured, whereas here only a small region of the air-water interface (close to the contact line) is relevant.

clearly fails at explaining the measured trend. Hence, we can discount the viscous properties of the liquid as a possible explanation.

In contrast, the molecular kinetic theory (equation 1.39) provides a good fit to the data, with fitting parameters $\lambda = 2\,\text{nm}$ and $K_0 = 86\,\text{Hz}$. The value of λ agrees with typical values that have been reported by other studies. However, typical values reported for K_0 are of the order of $1 \times 10^9\,\text{Hz}$ to $1 \times 10^{10}\,\text{Hz}$ for water, which significant differ from the 86 Hz that we obtained from the fit [17].

Conclusion Both the adaptive wetting theory and the molecular kinetic theory provide good fits to the experimental data. However, it is possible to show that adaptation (of γ_{SL}) is the true cause of the measured trend by performing the following experiment.

A drop was expanded on the surface. Then, the drop was removed from the surface and a second drop was injected at the same spot and at the same speed. For the first drop, $\Theta_{\text{A}} \approx 120^\circ$ when the speed was above $\approx 20\,\mu\text{m}\,\text{s}^{-1}$. When the time between removing the first drop and creating the second drop was only a few minutes (5 min in the experiment), Θ_{A} was only 112° for the second drop (even at high speeds). But when the surface was allowed to rest for 120 min between removing the first drop and creating the second drop, the contact angle rose back to 120°.

This experiment cannot be explained using the molecular kinetic theory, which predicts that the contact angle should be the same for both the first and second drops, as long as the contact line speed is the same in both cases. In contrast, the experiment can be interpreted based on the adaptive wetting theory. The first drop causes uncrosslinked PDMS chains to move to the top of the PDMS matrix (at the water-PDMS interface). When the drop is removed, the uncrosslinked chains remain on top for a certain amount of time. Hence, when the second drop is expanded on the same spot within 5 min, γ_{SL} starts at the 'adapted value' and therefore the contact angle is 112°. When the duration between removing the first drop and placing the second drop is 120 min, there is sufficient time for the uncrosslinked chains to diffuse back into the bulk of the PDMS matrix and the contact angle rises back to 120°.

3.3.2 Receding contact angle

The measured receding contact angles was between $80^\circ \leq \Theta_{\text{R}} \leq 100^\circ$, where higher angles correspond to longer contact times (or slower receding speeds).

3.4 Summary

Silicone (PDMS) elastomers consist of a crosslinked matrix containing a small fraction of uncrosslinked polymer chains. These uncrosslinked chains rearrange in the crosslinked matrix when water drops are placed on the surface. The accumulation

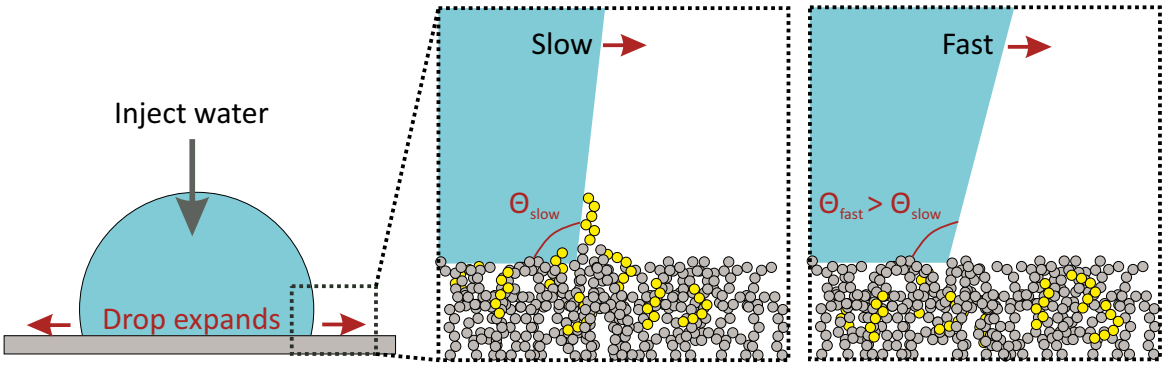

Figure 3.7: Microscopic picture of advancing air-water interface on PDMS. Each chain represents a PDMS chain. The grey chains correspond to polymers that are crosslinked to one another whereas the yellow chains correspond to uncrosslinked polymers that are free to move around. When the interface advances slowly (slower than the adaptation velocity), the PDMS chains have time to reorganise and free chains migrate to the contact line.

of uncrosslinked PDMS chains at the air-water interface reduces the surface tension of the drop. The time taken for the air-water interface to become completely covered by uncrosslinked PDMS chains depends on the molecular weight of the chains and on the fraction of uncrosslinked chains present in the elastomer. It takes longer for drops to become cloaked when the chains have a higher molecular weight and when there is a smaller fraction of uncrosslinked chains in the elastomer.

Uncrosslinked PDMS chains also influence the contact angle of water on silicone elastomers. It takes a finite amount of time (defined by the adaptation speed) for uncrosslinked chains to reach the three-phase contact line. When a water-air interface advances faster than the adaptation speed, the chains do not have sufficient time to reach the contact line. In contrast, when the interface advances slowly, the uncrosslinked chains have enough time to reach the contact line, causing the advancing contact angle to be lower (112° compared to 120°).

Chapter 4

Capillary force on rotating particles

The capillary force between particles and liquid-fluid interfaces has been widely studied, both experimentally and theoretically. Various works have focused on the capillary adhesion between moist particles (e.g. in a sandcastle) and on the force required to overcome the capillary adhesion between liquids and particles [95, 87, 4, 93, 25]. However, the effect of rotation on the capillary force remains largely unexplored despite its potential relevance in addressing question such as: Why does granular matter flow more slowly when moist?

In this chapter, I investigate the capillary force acting on particles when they rotate at an interface, focusing on the following questions: How much torque is required to rotate a particle at an interface? Does rotation increase or decrease the force required to detach a particle from an interface? How do the shape of the contact line and the variation of the contact angle around the contact line influence the detachment force? The findings of this chapter will be important in chapter 5, to understand the influence of rolling on the removal of particles from surfaces using water drops.

4.1 Why does rotation influence the capillary force?

An ideal (perfectly smooth and homogeneous) solid has a unique contact angle with respect to a liquid. This contact angle is given by Young's law (equation 1.13). Therefore, when an ideal particle rotates at a liquid-air interface, the interface does not deform as long as it has time to reach equilibrium [figure 4.1 (a)].

However, all real solids (including particles) exhibit contact angle hysteresis (section 1.7). Therefore, when a (real) particle rotates relative to a liquid-air interface, the contact angle on the side that rolls (into) out of the liquid must be equal to the (advancing) receding contact angle, (Θ_A) Θ_R [figure 4.1 (b)].

This asymmetry gives rise to two effects. First, it causes a torque that opposes the rotation (will be discussed section 4.2). I will call this torque the 'resistive capillary

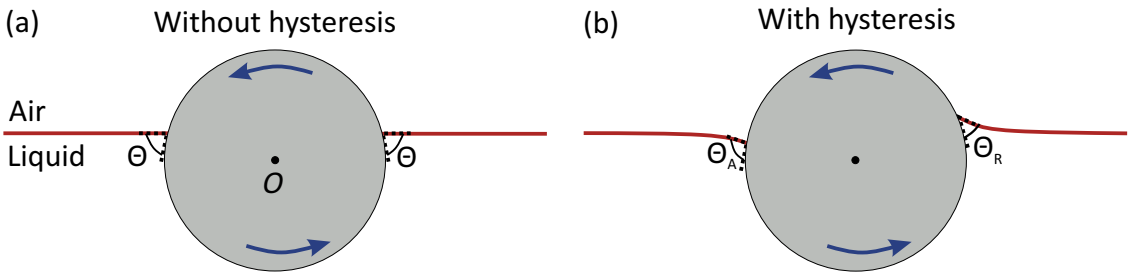

Figure 4.1: Particle (grey) rotating at a liquid-air interface (red), ignoring gravitational effects. (a) Without contact angle hysteresis, the interface remains flat and symmetric since the contact angle has a unique value, Θ. (b) With contact angle hysteresis, the interface becomes asymmetric. On the right, the angle is equal to the receding contact angle, Θ_R, whereas on the left, it is equal to the advancing contact angle, Θ_A.

torque'. Second, it influences the force required to detach the particle from the interface (will be discussed in section 4.3).

4.2 Resistive capillary torque

In this section, I derive an expression for the resistive capillary torque and discuss its consequences.

4.2.1 Derivation

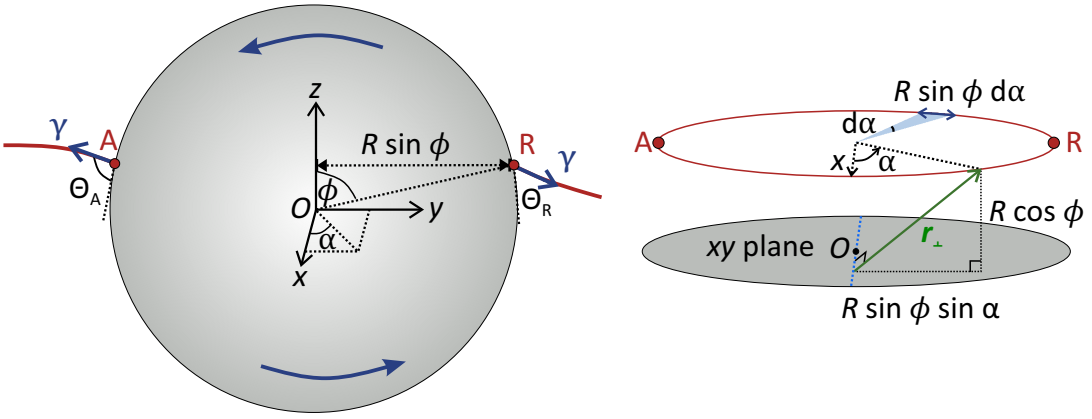

Figure 4.2: Particle rotating at an interface. Left: Schematic of particle rotating about a horizontal axis going through its centre. The contact line is marked by the points A and R. Right: The circular contact line is drawn in red. The blue dotted line shows the rotational axis.

As model system, I consider a spherical particle at a liquid-fluid interface. In general, the second fluid can be any gas or any liquid which is immiscible with the first liquid. In the following, I will refer to the second fluid as 'air'. The aim of this section is to calculate torque required to rotate the particle about the x-axis which

goes through its centre (figure 4.2).[1] When the particle rotates counterclockwise, the liquid-air interface recedes (advances) on the right (left) side of the axis of rotation. This asymmetry gives rise to a torque about the axis of rotation,

$$\boldsymbol{M} = \oint_{\mathrm{CL}} \boldsymbol{r}_\perp \times \boldsymbol{\gamma}\, dl, \tag{4.1}$$

where $\boldsymbol{r}_\perp$ is the perpendicular vector from the rotational axis to the three-phase contact line (red circle in figure 4.2, right), $\times$ denotes the vector cross product, and $dl = R\sin\phi\, d\alpha$ is the differential contact line length. The contour integral is around the contact line (CL), which is assumed to be circular. $\boldsymbol{\gamma}$ acts at the contact line and makes an angle $\Theta(\alpha)$ with the particle, where $\Theta(\alpha)$ is the contact angle at an azimuthal angle α. In spherical coordinates, $\boldsymbol{\gamma}$ is given by

$$\boldsymbol{\gamma} = \gamma\sin\Theta(\alpha)\ \hat{\boldsymbol{r}}\ +\ \gamma\cos\Theta(\alpha)\ \hat{\boldsymbol{\phi}}, \tag{4.2}$$

where $\hat{\boldsymbol{r}}$ is the radial unit vector from the centre of the sphere and $\hat{\boldsymbol{\phi}}$ is the polar unit vector defined from the z-axis. $\boldsymbol{r}_\perp$ can most easily be expressed in terms of the cartesian unit vectors:

$$\boldsymbol{r}_\perp = R\sin\phi\sin\alpha\ \hat{\boldsymbol{y}} + R\cos\phi\ \hat{\boldsymbol{z}}. \tag{4.3}$$

In order to evaluate the cross product in equation 4.1, $\boldsymbol{\gamma}$ is first expressed in cartesian coordinates using the following transformation:

$$\begin{pmatrix} \hat{\boldsymbol{r}} \\ \hat{\boldsymbol{\phi}} \\ \hat{\boldsymbol{\alpha}} \end{pmatrix} = \begin{pmatrix} \sin\phi\cos\alpha & \sin\phi\sin\alpha & \cos\phi \\ \cos\phi\cos\alpha & \cos\phi\sin\alpha & -\sin\phi \\ -\sin\alpha & \cos\alpha & 0 \end{pmatrix} \begin{pmatrix} \hat{\boldsymbol{x}} \\ \hat{\boldsymbol{y}} \\ \hat{\boldsymbol{z}} \end{pmatrix}. \tag{4.4}$$

After applying the transformation to equation 4.2, $\boldsymbol{\gamma}$ can be written in terms of the cartesian unit vectors:

$$\boldsymbol{\gamma} = \gamma \begin{pmatrix} \sin\Theta(\alpha)\sin\phi\cos\alpha + \cos\Theta(\alpha)\cos\phi\cos\alpha \\ \sin\Theta(\alpha)\sin\phi\sin\alpha + \cos\Theta(\alpha)\cos\phi\sin\alpha \\ \sin\Theta(\alpha)\cos\phi - \cos\Theta(\alpha)\sin\phi \end{pmatrix}. \tag{4.5}$$

Here, the first, second and third rows correspond to the $\hat{\boldsymbol{x}}$, $\hat{\boldsymbol{y}}$ and $\hat{\boldsymbol{z}}$ components, respectively. Now, the cross product in equation 4.1 can be evaluated:

[1] In figure 4.2, the advancing and receding sides (points A and R) are drawn on the same horizontal level. This does not lead to any loss in generality, even if in reality R may be higher than A [59], because the coordinate system can always be rotated such that these two points have the same z-coordinate.

$$\boldsymbol{r}_\perp \times \boldsymbol{\gamma} = \gamma R \begin{pmatrix} 0 \\ \sin\phi\sin\alpha \\ \cos\phi \end{pmatrix} \times \begin{pmatrix} \sin\Theta(\alpha)\sin\phi\cos\alpha + \cos\Theta(\alpha)\cos\phi\cos\alpha \\ \sin\Theta(\alpha)\sin\phi\sin\alpha + \cos\Theta(\alpha)\cos\phi\sin\alpha \\ \sin\Theta(\alpha)\cos\phi - \cos\Theta(\alpha)\sin\phi \end{pmatrix}$$

$$= \gamma R \begin{pmatrix} -\cos\Theta(\alpha)\sin^2\phi\sin\alpha - \cos\Theta(\alpha)\cos^2\phi\sin\alpha \\ \sin\Theta(\alpha)\sin\phi\cos\phi\cos\alpha + \cos\Theta(\alpha)\cos^2\phi\cos\alpha \\ -\sin\Theta(\alpha)\sin^2\phi\sin\alpha\cos\alpha - \cos\Theta(\alpha)\sin\phi\cos\phi\sin\alpha\cos\alpha \end{pmatrix}$$

$$= \frac{\gamma R}{2} \begin{pmatrix} -2\cos\Theta(\alpha)\sin\alpha \\ 2\sin\Theta(\alpha)\sin\phi\cos\phi\cos\alpha + 2\cos\Theta(\alpha)\cos^2\phi\cos\alpha \\ -\sin\Theta(\alpha)\sin^2\phi\sin 2\alpha - \cos\Theta(\alpha)\sin\phi\cos\phi\sin 2\alpha \end{pmatrix}. \tag{4.6}$$

Integrating the $\hat{\boldsymbol{x}}$ component of $\boldsymbol{r}_\perp \times \boldsymbol{\gamma}$ around the contact line gives

$$M_x = -\gamma R^2 \int_0^{2\pi} \cos\Theta(\alpha)\sin\phi\sin\alpha \; d\alpha. \tag{4.7}$$

The $\hat{\boldsymbol{y}}$ component of the integral is

$$M_y = \gamma R^2 \int_0^{2\pi} [\sin\Theta(\alpha)\sin\phi\cos\phi + \cos\Theta(\alpha)\cos^2\phi]\sin\phi\cos\alpha \; d\alpha = 0. \tag{4.8}$$

M_y evaluates to zero because the terms in α are $\sin\Theta(\alpha)\cos\alpha$ and $\cos\Theta(\alpha)\cos\alpha$, which both evaluate to zero when integrated from 0 to 2π. These terms integrate to zero because $\sin\Theta(\alpha)$ and $\cos\Theta(\alpha)$ are even functions about the yz plane whereas $\cos\alpha$ is an odd function. Hence, their product is an odd function and therefore the integral is zero.

The $\hat{\boldsymbol{z}}$ component of the integral is

$$M_z = -\frac{\gamma R^2}{2} \int_0^{2\pi} [\sin\Theta(\alpha)\sin^2\phi + \cos\Theta(\alpha)\sin\phi\cos\phi]\sin\phi\sin 2\alpha \; d\alpha = 0. \tag{4.9}$$

M_z evaluates to zero because the terms in α are $\sin\Theta(\alpha)\sin 2\alpha$ and $\cos\Theta(\alpha)\sin 2\alpha$, which are both odd functions about the yz plane.

Intuitively, $M_y = 0$ and $M_z = 0$ are expected due to symmetry of the surface tension vector about the yz plane. Any surface tension component which produces a moment along the $+y$ or $+z$ direction is cancelled by an equal and opposite component pointing along $-y$ or $-z$, respectively. Thus, the only non-zero torque component is M_x. Since the capillary torque opposes rotation, M_x is negative. In the following, I will focus on the magnitude of the torque, $\left|\vec{\boldsymbol{M}}\right| = M = -M_x$ and I will refer to $-M_x$ as M.

Evaluating M (equation 4.7) further requires knowledge of the contact angle variation around the contact line, $\Theta(\alpha)$. $\Theta(\alpha)$ is expected to be analogous to the

contact angle variation around a moving drop with a circular contact line. In both cases, the contact angle has a maximum (advancing angle) on one side and a a minimum (receding angle) on the opposite side. Several models have been proposed to describe the variation of the contact angle between these two extremities (for a drop). Dimitrakopoulos and Higon [36] used a step function, Korte and Jacobi [69] assumed $\Theta(\alpha)$ to be linear, Extrand and Kumagai [44] assumed that $\cos\Theta(\alpha)$ is linear, and ElSherbini and Jacobi [40] experimentally demonstrated that both $\Theta(\alpha)$ and $\cos\Theta(\alpha)$ can be fitted by a cubic polynomial. It turns out that these different assumptions lead to results that only differ by a numerical pre-factor.

For simplicity, I first consider a circular contact line divided between an advancing and a receding side with the following contact angle dependence:

$$\Theta(\alpha) = \begin{cases} \Theta_{\mathrm{R}}, & 0 < \alpha < \pi \\ \Theta_{\mathrm{A}}, & \pi < \alpha < 2\pi. \end{cases} \tag{4.10}$$

For this case, equation 4.7 can be written as

$$\frac{M}{\gamma R^2} = \int_0^{\pi} \cos\Theta_{\mathrm{R}} \sin\phi \sin\alpha \; d\alpha + \int_{\pi}^{2\pi} \cos\Theta_{\mathrm{A}} \sin\phi \sin\alpha \; d\alpha$$

$$= 2\sin\phi(\cos\Theta_{\mathrm{R}} - \cos\Theta_{\mathrm{A}}). \tag{4.11}$$

When more realistic and complex expressions are used to describe $\Theta(\alpha)$, the resulting expression is similar to equation 4.11, but with a different pre-factor:

$$\frac{M}{\gamma R^2} = 2K\sin\phi(\cos\Theta_{\mathrm{R}} - \cos\Theta_{\mathrm{A}}). \tag{4.12}$$

$K = 1/\pi \approx 0.32$ when $\cos\Theta(\alpha)$ is assumed to be linear in α (appendix A.1.1) and $K = 24/\pi^3 \approx 0.77$ when $\cos\Theta(\alpha)$ is assumed to be cubic in α [see figure 4.3 (a) and appendix A.1.2]. The results are summarised in table 4.1. I will use $K = 24/\pi^3$ throughout this thesis because the cubic contact angle variation is both smooth and continuous, and therefore likely to be the most realistic.

Table 4.1: K factors in equation 4.12 for different contact angle variations, assuming a circular contact line.

$\Theta(\alpha)$	K
Step	1
$\cos\Theta(\alpha)$ linear in α	$1/\pi \approx 0.32$
$\cos\Theta(\alpha)$ cubic in α	$24/\pi^3 \approx 0.77$

Alternatively, equation 4.12 can be written as

$$\frac{M}{\gamma R^2} = 4K \sin\phi \sin\Theta \sin\frac{\Delta\Theta}{2}, \tag{4.13}$$

where $\Theta = (\Theta_A + \Theta_R)/2$ is the mean contact angle and $\Delta\Theta = \Theta_A - \Theta_R$ is the contact angle hysteresis. The following trigonometric identity was used to arrive at equation 4.13 from equation 4.12:

$$\cos A - \cos B = -2 \sin\frac{A+B}{2} \sin\frac{A-B}{2}. \tag{4.14}$$

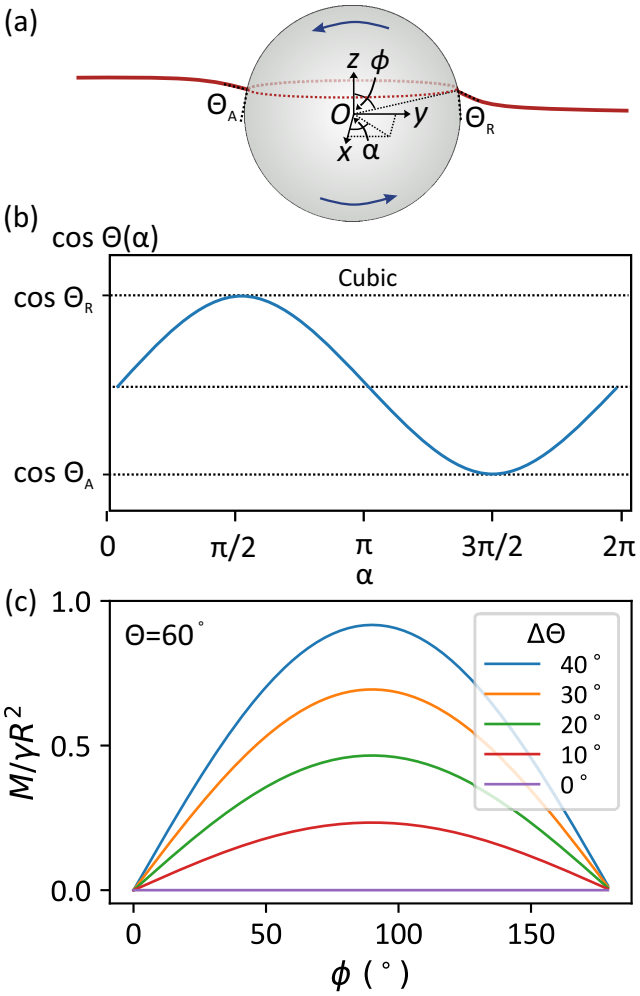

Figure 4.3: (a) Particle rotating at an interface. The contact line is assumed to be circular. (b) Function describing the variation of the contact angle around the contact line. (c) Capillary torque acting on a sphere [average contact angle, $\Theta = (\Theta_A + \Theta_R)/2 = 60°$] as a function of the polar angle, ϕ. The capillary torque increases with contact angle hysteresis, $\Delta\Theta = \Theta_A - \Theta_R$, as shown by the different curves.

Figure 4.3 (b) shows a plot of $M/\gamma R^2$ as a function of ϕ, using $\Theta = 60°$ as an example. M has a maximum at $\phi = 90°$ because the length of the contact line is largest at this position. The torque tends to zero as ϕ tends to 0° and 180° since the length of the contact line goes to zero at these two extremities. As the contact angle hysteresis increases, the capillary torque also increases since a higher $\Delta\Theta$ causes a more asymmetric interface.

4.2.2 Special cases and implications

To gain further insight into the implications of the capillary torque, I consider two special cases: (1) when the particle rotates about its static equilibrium position, and (2) when the particle is surrounded by a liquid meniscus on a flat surface. Furthermore, I demonstrate that capillary torque is important when describing particles in Brownian motion at an interface and when considering the rolling of wet particles on surfaces.

4.2.2.1 Particle rotating about its equilibrium position

This configuration [figure 4.4 (a)] is relevant to describe particles adsorbed at the surface of a lake, at the surface of a bubble (e.g. in flotation [28]), or at the surface of droplets in a Pickering emulsion [29, 100].

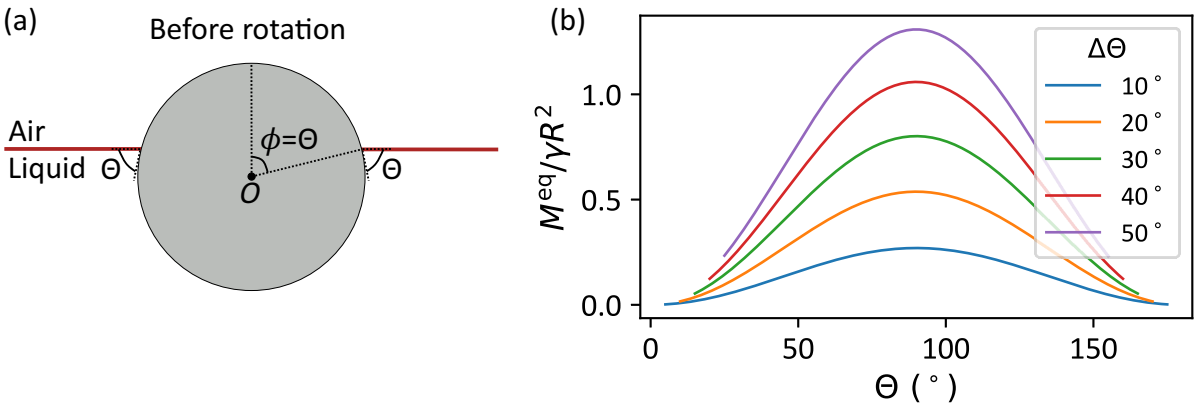

Figure 4.4: (a) Static particle in equilibrium at a liquid-air interface ($\phi = \Theta$). (b) Capillary torque as a function of the average contact angle when the particle rotates about its initial equilibrium position.

When an external force is applied, particles do not rotate unless the applied torque exceeds the resistive capillary torque. The resistive torque on a particle rotating about its equilibrium configuration is obtained by substituting $\phi = \Theta$ in equation 4.13:

$$M^{\mathrm{eq}} = 4\gamma K R^2 \sin^2\Theta \sin\frac{\Delta\Theta}{2}. \tag{4.15}$$

M^{eq} is symmetric around $\Theta = 90°$ and it increases with contact angle hysteresis [figure 4.4 (b)]. I have restricted the results to a maximum contact angle hysteresis of $\Delta\Theta = 50°$, since the assumptions about the shape of the contact line might no longer be appropriate for very large $\Delta\Theta$.

Practically, most particles are mildly hydrophilic to mildly hydrophobic (mean contact angle between around 30° to 90° with water). Special treatments, such as plasma cleaning or the addition of nanoscale roughness, are usually required to achieve lower or higher average contact angles with water. Therefore, for most practical cases,

the torque required to rotate a particle about its equilibrium position at an air-water interface is of the order of γR^2 [figure 4.4 (b)].

4.2.2.2 Brownian motion at an interface

In thermal equilibrium, small particles exhibit Brownian motion. When particles are in Brownian motion at an interface, the translational motion is constrained to the two-dimensional interface [20, 35]. Furthermore, I will show that particles at an interface do not rotate as they would do when fully dispersed in the liquid. Rotation becomes negligible since it is opposed by capillary torque.

Here, I quantify this effect by calculating the root mean square angle through which thermal energy rotates a particle at an interface. As an example, consider a hydrophobic particle $\Theta = 90^\circ$ resting in equilibrium (half-submerged) at a horizontal air-water interface. In the complete absence of external forces, $\phi = \Theta = 90^\circ$, along the entire contact line. When small rotational forces are applied, the contact line on the particle will remain pinned unless the angular rotation against the interface is greater than half the contact angle hysteresis. At room temperature, thermal energy will attempt to cause the particle to vibrate and rotate. When thermal energy rotates the particle counterclockwise by a small angle ϑ about the x axis, the contact angle on the right side becomes $\Theta - \vartheta$ and the contact angle on the left becomes equal to $\Theta + \vartheta$. Therefore, the magnitude of the capillary torque resisting the thermal rotation is obtained by substituting $\Delta\Theta = 2\vartheta$ (and $\Theta = 90^\circ$) in equation 4.15:

$$M = 4\gamma R^2 \sin\vartheta. \tag{4.16}$$

Since ϑ is expected to be small,[2] $\sin\vartheta \approx \vartheta$. Hence, the work required to oppose capillary torque and rotate the particle by ϑ about the x axis is

$$W = \int_0^\vartheta M \; d\vartheta' = 4\gamma R^2 \int_0^\vartheta \vartheta' \; d\vartheta'$$

$$= 2\vartheta^2 \gamma R^2. \tag{4.17}$$

As W is quadratic in ϑ, the equipartition theorem (section 1.10) can be applied. According to the equipartition theorem, the thermal energy accessible to each rotational degree of freedom is $k_\mathrm{B}T/2$, where k_B is the Boltzmann constant and T is the absolute temperature. Since capillary torque influences rotation about the x and the y axes, there are two degrees of freedom for rotation against the interface. Therefore, the average potential energy associated with rotating the particle against the interface is $\langle W \rangle = k_\mathrm{B}T$. As a result, the root mean square angular displacement caused by Brownian motion is

[2] I will later show that this is indeed a valid assumption.

$$\sqrt{\langle \vartheta^2 \rangle} = \frac{1}{R}\sqrt{\frac{k_\mathrm{B}T}{2\gamma}}. \tag{4.18}$$

For a nanoparticle of radius 50 nm at an air-water interface ($\gamma = 73\,\mathrm{mN\,m^{-1}}$, $T = 300\,\mathrm{K}$), we obtain $\sqrt{\langle \vartheta^2 \rangle} \approx 0.2°$.[3] Since all real particles have a contact angle hysteresis, $\Delta\Theta \gg 0.2°$, thermal energy is insufficient to overcome contact line pinning and cause the particle to rotate relative to the interface. Hence, thermal fluctuations can only rotate the particle with a root mean square angle of around 0.2° about its equilibrium position. Every time thermal fluctuations rotate the particle, the pinned contact line will restore it back to the equilibrium configuration, thus preventing any continuous rotation.

4.2.2.3 Particle surrounded by a meniscus

When a hydrophilic particle is placed in contact with a hydrophilic surface in air, a water meniscus forms around the contact region due to the condensation of water vapour from the atmosphere [figure 4.5 (a)] [110, 25]. Capillary condensation leads to an increase in the normal adhesion force between particles and surfaces due to capillary forces acting through the water meniscus. The presence of a small meniscus between particles (e.g. moist sand grains) or between a particle and a flat surface also influences their rolling friction. One of the factors that contributes to the rolling friction is the capillary torque. When the contact line diameter between the particle and the meniscus is d (as sketched in figure 4.5), the resistive capillary torque that needs to be overcome to roll the particle is obtained by substituting $2R\sin\phi = d$ in equation 4.12:

$$M = \gamma K d R(\cos\Theta_\mathrm{R} - \cos\Theta_\mathrm{A}). \tag{4.19}$$

In figure 4.5 (b), $M/\gamma dR$ (equation 4.19) is plotted against the mean contact angle for different contact angle hysteresis. The capillary torque increases with contact angle hysteresis and is symmetric about $\Theta = 90°$. For any contact angle hysteresis, the maximum corresponds to a mean contact angle of 90°, because in this case the tangential component of surface tension opposes rotation on both the advancing and receding sides. This is not the case for other values of Θ. For instance, when $\Theta_\mathrm{A} = 50°$ and $\Theta_\mathrm{R} = 30°$, the tangential component of surface tension still opposes rotation on the receding side but acts in the direction of rotation on the advancing side. Therefore, the overall resistive torque is lower than when $\Theta = 90°$.

Equation 4.19 is also valid for a particle rolling on a thin liquid film, for example in experiments performed by Bico *et al.* [15], and by Schade and Marshall [92]. However, capillary torque is only one of several contributing factors to the resistive force acting

[3] This confirms the assumption about ϑ being small.

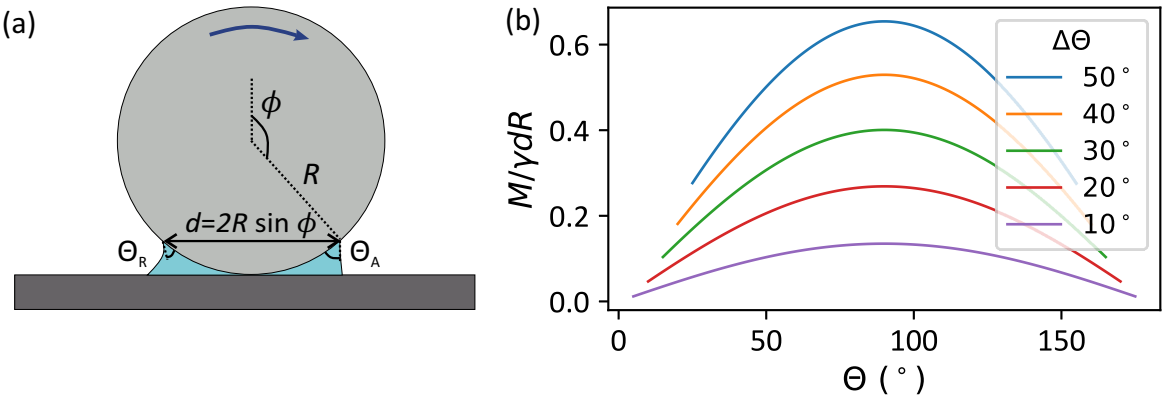

Figure 4.5: (a) Particle surrounded by a meniscus on a flat surface. (b) Resistive capillary torque experienced by a particle rolling on a flat surface when there is a small meniscus between the particle and the surface.

on a sphere rolling on a thin liquid film. For a full description, the solid-solid rolling friction, which arises due to deformation losses and due to the energy required to peel the rear contact between the two solid surfaces, has to be included. Furthermore, the viscous forces and Laplace pressure distribution inside the meniscus have to be considered [77]. The relative importance of each of these contributions depends on the material properties (viscosity, surface roughness, viscoelastic properties, surface energies) of the particle, the flat surface and the liquid meniscus.

Interestingly, capillary torque implies that the onset at which a particle begins to roll on a wet inclined surface occurs at a finite angle of inclination, even when there is no solid-solid rolling friction between the particle and the surface. To gain intuition on how significant the capillary torque is, consider a particle on a flat surface tilted by an angle α to the horizontal. How large does the particle have to be for it to begin rolling down the inclined surface? The onset of rolling occurs when the driving torque due to the particle's weight becomes equal to the capillary torque. The torque produced by the weight of the particle is $mgR\sin\alpha$ (m: mass, $g = 9.81\,\mathrm{m\,s^{-2}}$: gravitational acceleration, R: particle's radius) whereas the capillary torque is given by equation 4.19. Rolling only starts when

$$mgR\sin\alpha > \gamma K d R(\cos\Theta_\mathrm{R} - \cos\Theta_\mathrm{A})$$

$$\implies R > \left[\frac{3\gamma K d(\cos\Theta_\mathrm{R} - \cos\Theta_\mathrm{A})}{4\pi\rho g\sin\alpha}\right]^{\frac{1}{3}}. \tag{4.20}$$

Here, I have expressed m in terms of the volume of the particle ($4\pi R^3/3$) and its density, ρ. As an example, a glass particle ($\rho \approx 2\,500\,\mathrm{kg\,m^{-3}}$) surrounded by a small water meniscus (with $d = R/5$, $\Theta_\mathrm{A} \approx 45°$ and $\Theta_\mathrm{R} \approx 10°$ [65]) on a surface tilted by $\alpha = 30°$ only starts rolling if its radius is larger than $\approx 250\,\mu\mathrm{m}$. Even though I have

assumed that the capillary torque is the only source of resistance in this example, the calculated radius is still larger than the radius above which a dry particle would usually start rolling down a dry flat surface (a dry 100 µm glass bead easily rolls down an inclined glass slide).

Capillary torque could also be a significant factor that contributes to reducing the mobility of moist granular matter. When dry, granular matter flows easily, as exemplified by sand flowing in an hourglass. In contrast, humid sand hardly flows and can even be moulded into various stable structures, such as sandcastles. Unlike dry particles, moist particles are connected by microscopic liquid bridges [60]. Several mechanisms have been identified to explain the reduced mobility of moist granular matter. First, the liquid bridges increase the normal adhesion between the particles [25], which in turn causes an increase in friction [19]. Second, the bridges form an extended network, resulting in a stiff structure [98]. A third factor is due to viscous dissipation within the liquid bridges [60]. However, none of these contributions consider the resistive capillary torque. Capillary torque also contributes to reducing the mobility of humid granular matter and is significant when the torque driving the motion of the moist particles is less than $\approx \gamma R^2$.

4.2.3 Unifying the results

The expression for the capillary torque acting on a particle rotating at the surface of a liquid (equation 4.12) is similar to that for the capillary torque acting on a particle surrounded by a small meniscus on a flat surface (equation. 4.19). Interestingly, when normalised by the contact line diameter and the particle's radius, these expressions are equivalent to the expression describing the friction force (per width) experienced by a drop moving on a flat surface (equation 1.21). For all three cases (figure 4.6), the effective force is

$$\frac{F}{L} = k(\cos\Theta_{\mathrm{R}} - \cos\Theta_{\mathrm{A}}), \tag{4.21}$$

where, L is the diameter of the contact line and $k = 24/\pi^3$ for a cubic contact angle variation. The prefactor k may vary depending on the precise contact line geometry and contact angle variation. For the rotating particles, the effective force in equation 4.21 corresponds to a tangential force applied along the circumference of the particle.

We can take advantage of the similarity of the scenarios sketched in figure 4.6 to indirectly determine the capillary torque (experimentally). Several methods have been developed to measure drop friction on various surfaces. In contrast, it is unusual, as well as practically challenging, to measure the torque required to rotate a small particle at an interface. Therefore, an estimate for the capillary torque that a particle made of material B would experience when it rotates at the interface between liquid

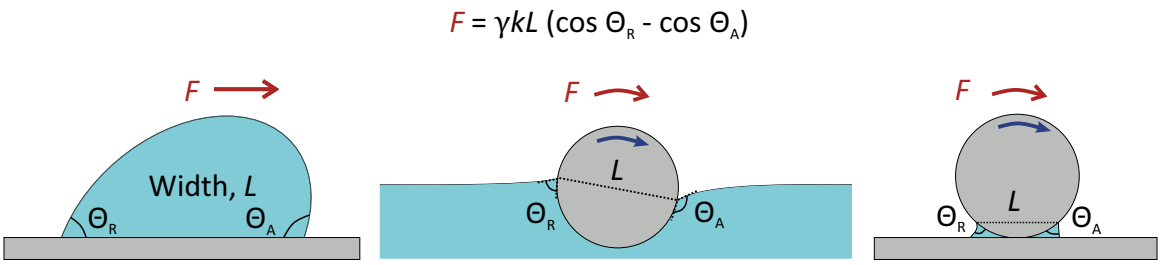

Figure 4.6: Equivalent scenarios. The same expression describes the force required to (1) move a drop on a flat surface, (2) rotate a particle at an interface, and (3) roll a particle on a flat surface when there is a liquid meniscus between the particle and the surface.

A and air can be conveniently obtained by instead measuring the force required to move a drop of liquid A on a flat surface made of material B.

4.3 Detachment force

In the previous section, I have considered the torque required to rotate a spherical particle about a fixed position at an interface. In this section, I consider the force required to detach a spherical particle from an interface, while it is rotating. I will use four models to describe the shape of the contact line and the contact angle variation around the contact line. The results obtained by the different models will be compared to test how sensitive the predictions are to differences in the assumed contact line geometry.

4.3.1 Derivation

The component of the capillary force acting normal to the plane containing the three-phase contact line is given by

$$F = \int_0^{2\pi} \gamma R \cos[\pi - \Theta(\alpha) - \phi] \cos\phi \; d\alpha, \tag{4.22}$$

where R is the particle's radius, ϕ is the polar angle between the y axis and the contact line, α is the azimuthal angle in the xy plane, and $\Theta(\alpha)$ is the contact angle between the liquid and the sphere at an azimuthal angle α. Note that in the previous section, ϕ was defined as the angle from the z-axis, whereas in this section ϕ is defined from the y-axis (figure 4.7).

When the particle rotates counterclockwise, the right half recedes relative to the liquid whereas the left half advances relative to the liquid. When the speed of rotation is higher than the detachment speed,[4] the contact line remains equally divided into an

[4]The detachment speed is the speed (along z) at which the centre of mass of the particle moves relative to the three-phase contact line.

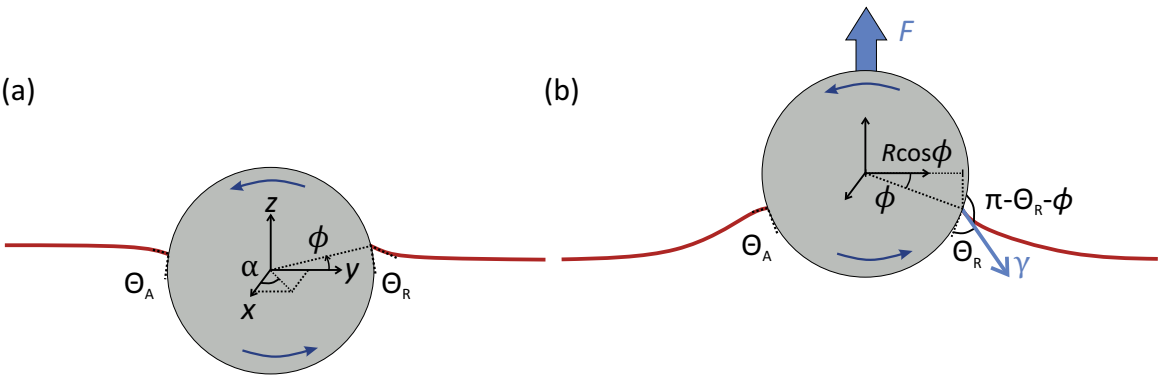

Figure 4.7: (a) Particle rotating at an interface. (b) Detaching the rotating particle from the interface.

advancing and a receding side throughout the detachment. The following calculations are based on this assumption.

4.3.1.1 Broken contact line with step contact angle variation

To evaluate equation 4.22 for a rotating particle, I first model the contact line as comprising of two separate regions as shown in figure 4.8 (a). On the right of the rotational axis ($0 < \alpha < \pi$), $\Theta = \Theta_{\mathrm{R}}$ and $\phi = \phi_{\mathrm{R}}$. On the left ($\pi < \alpha < 2\pi$), $\Theta = \Theta_{\mathrm{A}}$ and $\phi = \phi_{\mathrm{A}}$. ϕ_{R} is defined as the polar angle from the y-axis whereas ϕ_{A} is defined as the polar angle from the $-y$-axis. Both ϕ_{R} and ϕ_{A} are defined to be positive above the xy plane and negative below the xy plane. For this case, equation 4.22 can be written as

$$F = \int_0^{\pi} \gamma R \cos(\pi - \Theta_{\mathrm{R}} - \phi_{\mathrm{R}}) \cos\phi_{\mathrm{R}}\, d\alpha + \int_{\pi}^{2\pi} \gamma R \cos(\pi - \Theta_{\mathrm{A}} - \phi_{\mathrm{A}}) \cos\phi_{\mathrm{A}}\, d\alpha$$

$$= -\pi\gamma R \left[\cos(\Theta_{\mathrm{R}} + \phi_{\mathrm{R}}) \cos\phi_{\mathrm{R}} + \cos(\Theta_{\mathrm{A}} + \phi_{\mathrm{A}}) \cos\phi_{\mathrm{A}}\right] \tag{4.23}$$

Next, the detachment force can be calculated by finding the minimum/maximum value of F. The differential of F is given by

$$dF = \left(\frac{\partial F}{\partial \phi_{\mathrm{A}}}\right)_{\phi_{\mathrm{R}}} d\phi_{\mathrm{A}} + \left(\frac{\partial F}{\partial \phi_{\mathrm{R}}}\right)_{\phi_{\mathrm{A}}} d\phi_{\mathrm{R}}$$

$$\begin{aligned} &= \pi\gamma R[\sin(\phi_{\mathrm{A}} + \Theta_{\mathrm{A}}) \cos\phi_{\mathrm{A}} + \cos(\phi_{\mathrm{A}} + \Theta_{\mathrm{A}}) \sin\phi_{\mathrm{A}}]\, d\phi_{\mathrm{A}} \\ &+ \pi\gamma R[\sin(\phi_{\mathrm{R}} + \Theta_{\mathrm{R}}) \cos\phi_{\mathrm{R}} + \cos(\phi_{\mathrm{R}} + \Theta_{\mathrm{R}}) \sin\phi_{\mathrm{R}}]\, d\phi_{\mathrm{R}}. \end{aligned} \tag{4.24}$$

As a first approximation, ϕ_{A} and ϕ_{R} are assumed to be independent. In this case, $dF = 0$ when

$$\phi_{\mathrm{A}} = -\Theta_{\mathrm{A}}/2 + n\pi/2$$

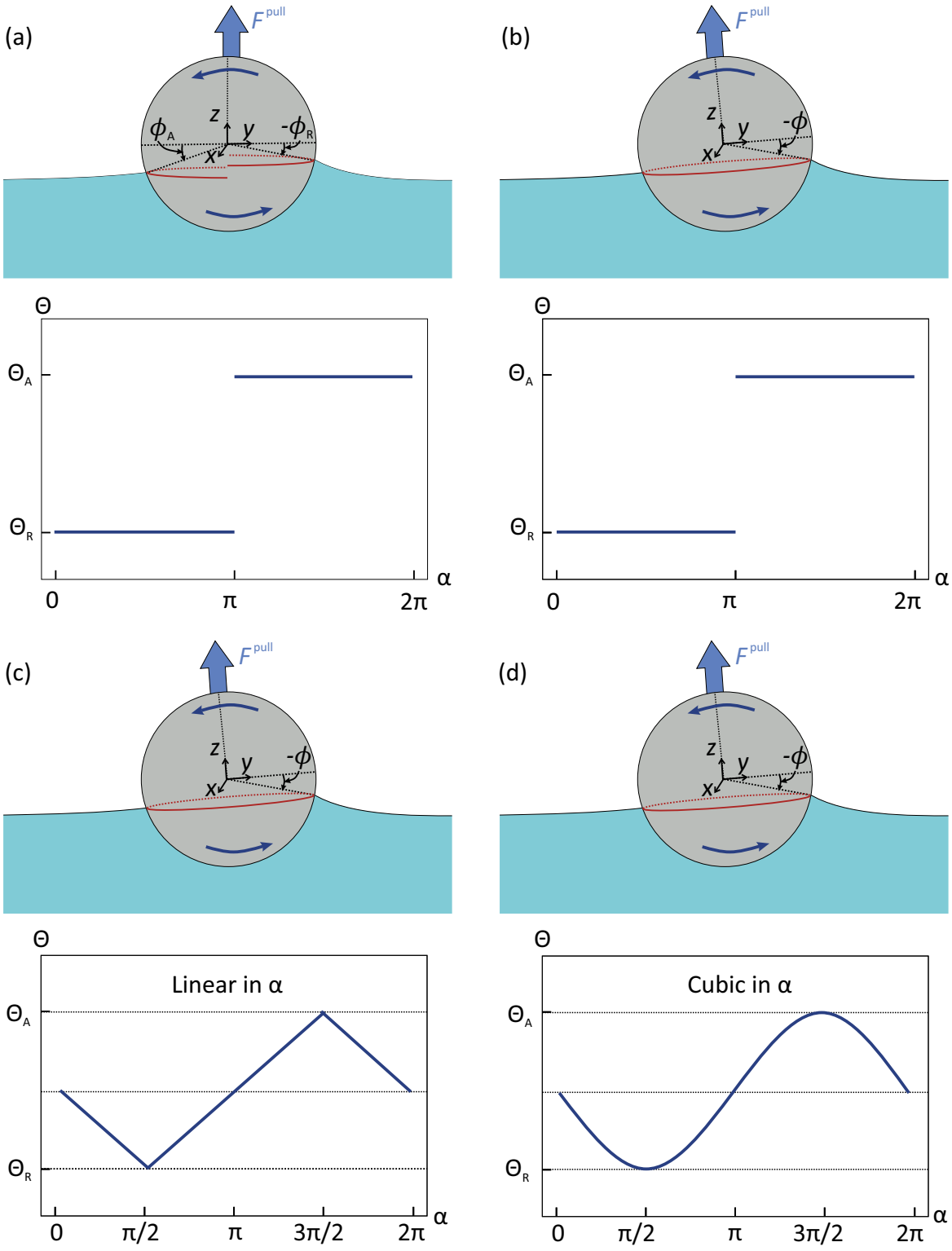

Figure 4.8: Contact line shapes and contact angle variation for the different models used when deriving the detachment force. (a) Model 1 - discontinuous contact line and a step contact angle variation. (b) Model 2 - continuous circular contact line and a step contact angle variation. (c) Model 3 - continuous circular contact line and a linear contact angle variation. (d) Model 4 - continuous circular contact line and a cubic contact angle variation.

and

$$\phi_{\mathrm{R}} = -\Theta_{\mathrm{R}}/2 + m\pi/2,$$

where $n = 0$ or 1, and $m = 0$ or 1 such that $-\pi/2 \leq \phi_{\mathrm{A}} \leq \pi/2$ and $-\pi/2 \leq \phi_{\mathrm{R}} \leq \pi/2$, respectively.

To determine whether these solutions correspond to a minimum (i.e. maximum downward capillary force) or a maximum (i.e. maximum upward capillary force), the second derivatives of F are calculated:

$$\left(\frac{\partial^2 F}{\partial \phi_{\mathrm{A}}^2}\right)_{\phi_{\mathrm{R}}} = 2\pi\gamma R[\cos(\phi_{\mathrm{A}} + \Theta_{\mathrm{A}})\cos\phi_{\mathrm{A}} - \sin(\phi_{\mathrm{A}} + \Theta_{\mathrm{A}})\sin\phi_{\mathrm{A}}]. \tag{4.25}$$

$$\left(\frac{\partial^2 F}{\partial \phi_{\mathrm{A}}^2}\right)_{\phi_{\mathrm{R}}} = \begin{cases} 2\pi\gamma R > 0, & \phi_{\mathrm{A}} = -\Theta_{\mathrm{A}}/2, \\ \\ -2\pi\gamma R < 0, & \phi_{\mathrm{A}} = (\pi - \Theta_{\mathrm{A}})/2. \end{cases} \tag{4.26}$$

Therefore, $\phi_{\mathrm{A}} = -\Theta_{\mathrm{A}}/2$ corresponds to a minimum and $\phi_{\mathrm{A}} = (\pi - \Theta_{\mathrm{A}})/2$ to a maximum.

Similarly, $\phi_{\mathrm{R}} = -\Theta_{\mathrm{R}}/2$ corresponds to a minimum whereas $\phi_{\mathrm{R}} = (\pi - \Theta_{\mathrm{R}})/2$ corresponds to a maximum. Substituting $\phi_{\mathrm{A}} = (\pi - \Theta_{\mathrm{A}})/2$ and $\phi_{\mathrm{R}} = (\pi - \Theta_{\mathrm{R}})/2$ in equation 4.23, gives the maximum upwards capillary force,

$$F^{\mathrm{push}} = \pi\gamma R\left(\sin^2\frac{\Theta_{\mathrm{R}}}{2} + \sin^2\frac{\Theta_{\mathrm{A}}}{2}\right). \tag{4.27}$$

This corresponds to the force required to detach the particle from the interface by completely pushing it into the liquid.

The minimum (i.e. maximum downwards) capillary force that the air-water interface exerts on the particle when the latter is pulled away from the water phase is obtained by substituting $\phi_{\mathrm{A}} = -\Theta_{\mathrm{A}}/2$ and $\phi_{\mathrm{R}} = -\Theta_{\mathrm{R}}/2$ in equation 4.23:

$$F^{\mathrm{pull}} = -\pi\gamma R\left(\cos^2\frac{\Theta_{\mathrm{R}}}{2} + \cos^2\frac{\Theta_{\mathrm{A}}}{2}\right). \tag{4.28}$$

Note that this force is negative since it acts downwards, pulling the particle towards the liquid. The magnitude this force corresponds to the force required to detach the particle from the interface by pulling it away from the liquid.

Alternative 'derivation' based on intuition To arrive at equation 4.27, I have assumed that the left and right halves of the particle are completely independent of each other. Therefore, I have effectively calculated the sum of the force required to push the left hemisphere (with contact angle Θ_{A}) and the force required to push the right hemisphere (with contact angle Θ_{R}).

With this picture in mind, we could have arrived at equation 4.27 by simply averaging the force required to push a non-rotating sphere (equation 1.27) having a

contact angle of Θ_A and that required to push a non-rotating sphere having a contact angle of Θ_R.

Similarly, equation 4.28 is simply the average of the forces required to pull a non-rotating sphere (equation 1.26) having a contact angle of Θ_R and a non-rotating sphere having a contact angle of Θ_A.

4.3.1.2 Circular contact line with step contact angle variation

In section 4.3.1.1, I have assumed that the left and right halves of the contact line are independent. This meant that the contact line was discontinuous at the axis of rotation [figure 4.8 (a)]. In this section, I assume a continuous circular contact line [figure 4.8 (b)].[5]

For this case, equation 4.22 can be written as

$$\begin{aligned} F &= \int_0^{\pi} \gamma R \cos(\pi - \Theta_R - \phi) \cos\phi \; d\alpha + \int_{\pi}^{2\pi} \gamma R \cos(\pi - \Theta_A - \phi) \cos\phi \; d\alpha \\ &= \pi\gamma R \left[\cos(\pi - \Theta_R - \phi) \cos\phi + \cos(\pi - \Theta_A - \phi) \cos\phi\right] \\ &= -\pi\gamma R \left[\cos(\Theta_R + \phi) \cos\phi + \cos(\Theta_A + \phi) \cos\phi\right] \\ &= -2\pi\gamma R \cos\left(\phi + \frac{\Theta_A + \Theta_R}{2}\right) \cos\left(\frac{\Theta_R - \Theta_A}{2}\right) \cos\phi. \end{aligned} \tag{4.29}$$

In the last step, we used the following trigonometric identity:

$$\cos(A + B) = 2\cos\left(\frac{A + B}{2}\right) \cos\left(\frac{A - B}{2}\right). \tag{4.30}$$

To find the maximum force as the particle is pushed (pulled) into (out of) the liquid, I calculate the derivative of F with respect to ϕ:

$$\begin{aligned} \frac{dF}{d\phi} = 2\pi\gamma R \Bigg[&\cos\left(\phi + \frac{\Theta_A + \Theta_R}{2}\right) \cos\left(\frac{\Theta_R - \Theta_A}{2}\right) \sin\phi \\ &+ \sin\left(\phi + \frac{\Theta_A + \Theta_R}{2}\right) \cos\left(\frac{\Theta_R - \Theta_A}{2}\right) \cos\phi \Bigg]. \end{aligned} \tag{4.31}$$

At the maximum/minimum points, $dF/d\phi = 0$. Equation 4.31 is equal to zero when

[5] The xy plane is defined as being parallel to the plane containing the contact line. Therefore, the angle ϕ take the same value everywhere along a continuous circular contact line.

$$\cos\left(\phi+\frac{\Theta_A+\Theta_R}{2}\right)\sin\phi=-\sin\left(\phi+\frac{\Theta_A+\Theta_R}{2}\right)\cos\phi$$

$$\Longrightarrow\ \tan\phi=-\tan\left(\phi+\frac{\Theta_A+\Theta_R}{2}\right)$$

$$\Longrightarrow\ \phi=-\frac{\Theta_A+\Theta_R}{4}\ \text{or}\ \frac{\pi}{2}-\frac{\Theta_A+\Theta_R}{4}.$$

The first solution leads to a downward capillary force. This downward force has to be overcome to detach the particle away from the liquid. Substituting $\phi=-(\Theta_A+\Theta_R)/4$ in equation 4.29 gives

$$F^{\text{pull}}=-2\pi\gamma R\cos\left(\frac{\Theta_A+\Theta_R}{4}\right)\cos\left(\frac{\Theta_R-\Theta_A}{2}\right)\cos\left(-\frac{\Theta_A+\Theta_R}{4}\right)$$

$$=-2\pi\gamma R\cos^2\left(\frac{\Theta_A+\Theta_R}{4}\right)\cos\left(\frac{\Theta_A-\Theta_R}{2}\right). \tag{4.32}$$

The second solution corresponds to the force required to detach the particle from the interface by pushing it into the liquid. Substituting $\phi=\pi/2-(\Theta_A+\Theta_R)/4$ into equation 4.29 gives

$$F^{\text{push}}=-2\pi\gamma R\cos\left(\frac{\pi}{2}+\frac{\Theta_A+\Theta_R}{4}\right)\cos\left(\frac{\Theta_R-\Theta_A}{2}\right)\cos\left(\frac{\pi}{2}-\frac{\Theta_A+\Theta_R}{4}\right)$$

$$=2\pi\gamma R\sin^2\left(\frac{\Theta_A+\Theta_R}{4}\right)\cos\left(\frac{\Theta_A-\Theta_R}{2}\right). \tag{4.33}$$

4.3.1.3 Circular contact line with linear contact angle variation

In sections 4.3.1.1 and 4.3.1.2, I have described the contact angle variation around the contact line by a step function. In this section, I use a continuous linear variation of the contact angle, as sketched in figure 4.8 (c).

In this case, $\Theta(\alpha)$ is given by

$$\Theta(\alpha)=\begin{cases}\frac{\alpha}{\pi}(\Theta_A-\Theta_R)+\frac{3}{2}\Theta_A-\frac{1}{2}\Theta_R, & -\pi<\alpha<-\frac{\pi}{2}\\ -\frac{\alpha}{\pi}(\Theta_A-\Theta_R)+\frac{1}{2}(\Theta_A+\Theta_R), & -\frac{\pi}{2}<\alpha<\frac{\pi}{2}\\ \frac{\alpha}{\pi}(\Theta_A-\Theta_R)+\frac{3}{2}\Theta_R-\frac{1}{2}\Theta_A, & \frac{\pi}{2}<\alpha<\pi.\end{cases} \tag{4.34}$$

Here, I have defined $-\pi < \alpha < \pi$ (instead of $0 < \alpha < 2\pi$ as in the above sections) so that $\Theta(\alpha)$ can be written in a similar form for $-\pi < \alpha < -\pi/2$ and $\pi/2 < \alpha < \pi$. This will simplify subsequent algebraic manipulations.

Since the contact line and the contact angles are symmetric about the yz-plane, equation 4.22 can be evaluated from $\alpha = -\pi/2$ to $\alpha = \pi/2$ and the result multiplied by 2, to obtain the total force. Substituting equation 4.34 into equation 4.22 gives

$$
\begin{aligned}
F &= 2\int_{-\frac{\pi}{2}}^{\frac{\pi}{2}} \gamma R \cos\left(\pi + \frac{\Theta_\mathrm{A} - \Theta_\mathrm{R}}{\pi}\alpha - \frac{\Theta_\mathrm{A} + \Theta_\mathrm{R}}{2} - \phi\right)\cos\phi \; d\alpha \\
&= -2\int_{-\frac{\pi}{2}}^{\frac{\pi}{2}} \gamma R \cos\left(\frac{\Theta_\mathrm{A} - \Theta_\mathrm{R}}{\pi}\alpha - \frac{\Theta_\mathrm{A} + \Theta_\mathrm{R}}{2} - \phi\right)\cos\phi \; d\alpha \\
&= -2\gamma R\cos\phi \frac{\left[\sin\left(\frac{\Theta_\mathrm{A}-\Theta_\mathrm{R}}{\pi}\alpha - \frac{\Theta_\mathrm{A}+\Theta_\mathrm{R}}{2} - \phi\right)\right]_{-\frac{\pi}{2}}^{\frac{\pi}{2}}}{\frac{\Theta_\mathrm{A}-\Theta_\mathrm{R}}{\pi}} \\
&= -\frac{2\pi}{\Theta_\mathrm{A} - \Theta_\mathrm{R}}\gamma R\cos\phi\left[-\sin(\Theta_\mathrm{R} + \phi) + \sin(\Theta_\mathrm{A} + \phi)\right] \\
&= -\frac{4\pi}{\Theta_\mathrm{A} - \Theta_\mathrm{R}}\gamma R\cos\phi\cos\left(\phi + \frac{\Theta_\mathrm{R} + \Theta_\mathrm{A}}{2}\right)\sin\left(\frac{\Theta_\mathrm{A} - \Theta_\mathrm{R}}{2}\right). \qquad (4.35)
\end{aligned}
$$

In the last step, the following trigonometric identity was used

$$\sin A - \sin B = 2\cos\left(\frac{A+B}{2}\right)\sin\left(\frac{A-B}{2}\right). \qquad (4.36)$$

Equation 4.35 is valid when Θ_A and Θ_R are expressed in radians.

Next, I equation 4.35 is differentiated with respect to ϕ to find the maximum and minimum forces.

$$
\begin{aligned}
\frac{dF}{d\phi} = -\frac{4\pi}{\Theta_\mathrm{A} - \Theta_\mathrm{R}}&\sin\left(\frac{\Theta_\mathrm{A} - \Theta_\mathrm{R}}{2}\right) \\
&\left[-\sin\phi\cos\left(\phi + \frac{\Theta_\mathrm{R} + \Theta_\mathrm{A}}{2}\right) - \cos\phi\sin\left(\phi + \frac{\Theta_\mathrm{R} + \Theta_\mathrm{A}}{2}\right)\right]. \qquad (4.37)
\end{aligned}
$$

At the minimum and maximum points, $dF/d\phi = 0$, which is fulfilled when the term in the square brackets is equal to zero. That is, when

$$
\begin{aligned}
-\sin\phi\cos\left(\phi + \frac{\Theta_\mathrm{R} + \Theta_\mathrm{A}}{2}\right) &= \cos\phi\sin\left(\phi + \frac{\Theta_\mathrm{R} + \Theta_\mathrm{A}}{2}\right) \\
\Rightarrow \tan\phi &= -\tan\left(\phi + \frac{\Theta_\mathrm{R} + \Theta_\mathrm{A}}{2}\right) \\
\Rightarrow \phi &= -\frac{\Theta_\mathrm{R} + \Theta_\mathrm{A}}{4} \text{ or } \frac{\pi}{2} - \frac{\Theta_\mathrm{R} + \Theta_\mathrm{A}}{4}. \qquad (4.38)
\end{aligned}
$$

Substituting $\phi = -(\Theta_R + \Theta_A)/4$, in equation 4.35 gives:

$$F^{\text{pull}} = -\frac{4\pi}{\Theta_A - \Theta_R}\gamma R \cos\left(-\frac{\Theta_R + \Theta_A}{4}\right)\cos\left(\frac{\Theta_R + \Theta_A}{4}\right)\sin\left(\frac{\Theta_A - \Theta_R}{2}\right)$$

$$= -\frac{4\pi}{\Theta_A - \Theta_R}\gamma R \cos^2\left(\frac{\Theta_R + \Theta_A}{4}\right)\sin\left(\frac{\Theta_A - \Theta_R}{2}\right). \tag{4.39}$$

Substituting, $\phi = \pi/2 - (\Theta_R + \Theta_A)/4$ in equation 4.35 gives:

$$F^{\text{push}} = -\frac{4\pi}{\Theta_A - \Theta_R}\gamma R \cos\left(\frac{\pi}{2} - \frac{\Theta_R + \Theta_A}{4}\right)\cos\left(\frac{\pi}{2} + \frac{\Theta_R + \Theta_A}{4}\right)\sin\left(\frac{\Theta_A - \Theta_R}{2}\right)$$

$$= \frac{4\pi}{\Theta_A - \Theta_R}\gamma R \sin^2\left(\frac{\Theta_R + \Theta_A}{4}\right)\sin\left(\frac{\Theta_A - \Theta_R}{2}\right). \tag{4.40}$$

4.3.2 Results and discussion

The expressions for the detachment forces obtained from the different models are summarised in table 4.2. In the following discussion, I will focus on F^{pull} to analyse the influence of contact angle hysteresis on the detachment force. Model 3 will be used as a reference against which the other models will be compared. Model 3 is chosen as the reference because it provides analytical results and is based on a continuous contact angle variation and contact line shape.

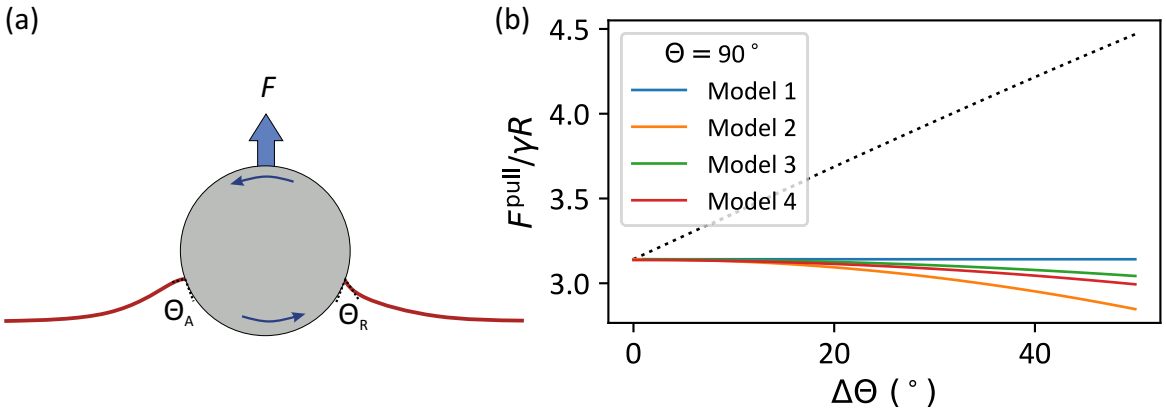

Figure 4.9: Comparison between the detachment force predicted by the models described in figure 4.8. The dotted black line shows the prediction for a non-rotating particle. Here, the average contact angle, $\Theta = \Theta_A + \Theta_R = 90°$. Note that $\Theta = \Theta_R = 90° - \Delta\Theta$ for the dotted black line since the interface recedes.

Comparison between different models Figure 4.9 compares the F^{pull} predicted by the different models as a function of the contact angle hysteresis (for an average

Table 4.2: Force required to detach a rotating particle from a liquid-air interface by pushing (pulling) it into (out of) the liquid, F^{push} (F^{pull}). Model 0 ignores rotation. Models 1, 2 and 3 take into account rotation. Model 1 assumes a discontinuous contact line divided into two separate semi circles [figure 4.8 (a)] . Model 2 assumes a circular contact line with a contact angle of Θ_{A} (Θ_{R}) on the right (left) side of the axis of rotation [figure 4.8 (b)]. Model 3 assume a continuous circular contact line with a linear contact angle variation [figure 4.8 (c)].

Model	F^{push}	F^{pull}
0	$2\pi\gamma R \sin^2 \frac{\Theta_{\text{A}}}{2}$	$2\pi\gamma R \cos^2 \frac{\Theta_{\text{R}}}{2}$
1	$\pi\gamma R \left(\sin^2 \frac{\Theta_{\text{R}}}{2} + \sin^2 \frac{\Theta_{\text{A}}}{2}\right)$	$\pi\gamma R \left(\cos^2 \frac{\Theta_{\text{R}}}{2} + \cos^2 \frac{\Theta_{\text{A}}}{2}\right)$
2	$2\ \pi\gamma R \sin^2 \left(\frac{\Theta_{\text{A}}+\Theta_{\text{R}}}{4}\right) \cos \left(\frac{\Theta_{\text{A}}-\Theta_{\text{R}}}{2}\right)$	$2\pi\gamma R \cos^2 \left(\frac{\Theta_{\text{A}}+\Theta_{\text{R}}}{4}\right) \cos \left(\frac{\Theta_{\text{A}}-\Theta_{\text{R}}}{2}\right)$
3	$\frac{4\pi}{\Theta_{\text{A}}-\Theta_{\text{R}}}\gamma R \sin^2 \left(\frac{\Theta_{\text{R}}+\Theta_{\text{A}}}{4}\right) \sin \left(\frac{\Theta_{\text{A}}-\Theta_{\text{R}}}{2}\right)$	$\frac{4\pi}{\Theta_{\text{A}}-\Theta_{\text{R}}}\gamma R \cos^2 \left(\frac{\Theta_{\text{R}}+\Theta_{\text{A}}}{4}\right) \sin \left(\frac{\Theta_{\text{A}}-\Theta_{\text{R}}}{2}\right)$

contact angle $\Theta = 90°$). The prediction for Model 4 (circular contact line, cubic contact angle variation) was obtained by numerically integrating equation 4.22 with respect to α and maximising the result with respect to ϕ. Two conclusions can be drawn. First, the force required to detach a rotating particle (solid lines) is lower than the force required to detach a non-rotating particle (black dotted line), regardless of the model used. Second, the predictions of Models 1, 2, 4 show little deviation with respect to Model 3 compared to their deviation from Model 0. These conclusions also apply to other values of Θ.

The deviation between Models 1, 2 and 4 relative to Model 3 is less than 10% up to $\Delta\Theta \approx 55°$ and $\Theta = 100°$ (Appendix A.2). In particular, Model 4, which provides the most realistic (smooth and continuous) contact angle variation, deviates from Model 3 by only 2%. This wide range of Θ and $\Delta\Theta$ includes most real particles.

In most practical cases, particles are not completely uniform but have local impurities and defects. Hence, the shape of the contact line and the contact angle variation may not follow the idealised geometries that I have assumed above. However, since the detachment force does not change significantly when different assumptions are made about the contact line geometry, the expression for Model 3 is expected to provide reasonable estimates for the force even when the contact line

is slightly distorted, as long as the correct values are inserted for the average contact angle and contact angle hysteresis.

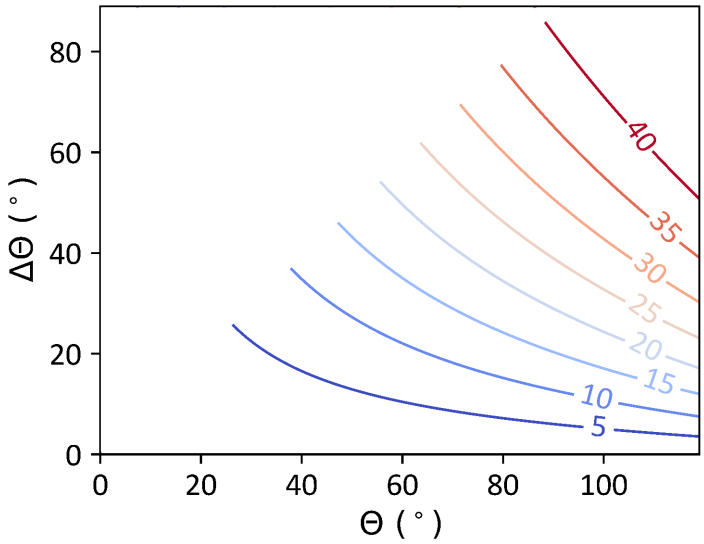

Figure 4.10: Percentage reduction in the detachment force between a non-rotating particle and a rotating particle. Each line shows contours of constant percentage reduction. The numbers associated with each contour gives the reduction in force (in %), calculated using equation 4.41.

Reduction in detachment force due to rotation The percentage reduction in the detachment force due to rotation is given by

$$\frac{F_0 - F_3}{F_0} \times 100, \tag{4.41}$$

where F_0 corresponds to the detachment force of a non-rotating particle (Table 4.2, Model 0)and F_3 corresponds to the detachment force of a rotating particle as predicted by Model 3 (Table 4.2, Model 3). The physical cause of the reduction in detachment force can be understood based on the following intuition. When a non-rotating particle is pulled out of a liquid, the average contact angle is Θ_R. In contrast, when the particle rotates during the detachment, the average contact angle increases to $(\Theta_A + \Theta_R)/2$. Therefore, rotation causes the particle to effectively be more lyophobic, which results in a lower detachment force. The percentage reduction in the detachment force can be as large as $\approx 40\%$, for example when $\Theta = 100^\circ$ and $\Delta\Theta \approx 50^\circ$ [figure 4.10].

In theory, even larger reductions can be obtained, but these would correspond to unrealistic values of Θ and $\Delta\Theta$, at least when the liquid is water or oils. The maximum static contact angle of water on any flat surface is around 120° (on fluorinated surfaces). Higher contact angles can only be achieved on very rough (superhydrophobic) surfaces. However, the expressions for the detachment force are not valid for very rough particles because the details of the contact line will become

important for superhydrophobic particles. For example, when a superhydrophobic particle is in the Cassie-Baxter state at an air-water interface, the contact line is separated by air gaps and therefore cannot be described by a continuous circle. In this case, the expressions for the detachment force has to be corrected by considering the actual length of the contact line, which is given by the apparent length of the contact multiplied by the area fraction, ϕ_s, that is in direct contact with the solid.

Is it economical to use rotation as a means to detach particles? Since rotation causes a decrease in the detachment force, it may at first seem that inducing rotation of particles could be a useful way to facilitate the detachment of particles from interfaces. However, this may not be economical from an energetic perspective because in order to rotate a particle at an interface, energy needs to be supplied to overcome resistive capillary torque described in section 4.2. The energy that needs to be supplied to rotate the particle is $2\pi M$ per revolution, where M is the resistive capillary torque given by equation 4.12. If $2\pi Mn$ (n is the number of revolutions before detachment actually occurs) is greater than the energy saved by having a lower detachment force, the total energy that will need to be supplied to induce rotation will be greater than the energy that is economised by having a lower detachment force.

4.4 Summary

In the first part of the chapter, I argued that a particle experiences a resistive capillary torque when rotating at a liquid-fluid interface. This is due to contact angle hysteresis. I derived an expression for the capillary torque and showed that it can be written as

$$M = \gamma K R L(\cos\Theta_R - \cos\Theta_A), \tag{4.42}$$

where $K = 24/\pi^3$ is a geometrical factor, R is the radius of the particle, L is the diameter of the three-phase contact line and Θ_R (Θ_A) is the receding (advancing) contact angle between the liquid and the particle. I described two scenarios where capillary torque is relevant. First, particles do not rotate when they are in Brownian motion at an interface because thermal energy is much less than the energy required to overcome capillary torque. Second, capillary torque prevents wet particles from rotating on a surface even when the coefficient of rolling friction between the particle and the surface is zero.

In the second part of the chapter, I derived analytical expressions for the force required to detach a particle from an interface while it rotates. I considered four different models, each assuming a different contact line shape and/or contact angle variation around the contact line. All the models predict that rotation can reduce the detachment force by up to $\approx 40\%$.

Chapter 5

Particle removal by drops

In this chapter, I image the collision between drops and single particles at different speeds using an inverted laser scanning confocal microscope. The forces acting on the drop during the collision are directly measured using microscope, as described in chapter 2. I combine the experiments in this chapter with the concepts developed in the previous chapters to address the following questions:

- What does a drop-particle collision look like on a microscopic scale?
- Which forces determine whether a particle can be removed from a surface?
- How can we increase the likelihood of particle removal?

5.1 Experimental setup

The experimental setup used in this chapter is sketched in figure 5.1. Refer to section 2.1 for details on laser scanning confocal microscopy and to section 2.2 for details on how the inverted microscope is used to measure horizontal forces.

5.2 Materials

5.2.1 Preliminary considerations

In general, many different materials can be used for the surface and the particle. This leads to a very large parameter space for the adhesion force and friction force between the particle and the surface. When the adhesion force and friction force are much smaller than the force between the drop and the particle, it is expected that the drop will always be successful at removing the particle. In contrast, when the adhesion force and friction force are much greater than the force between the drop and the particle, the drop will never be successful at removing the particle.

To observe both scenarios with the same system, the particle and surface must be chosen such that the adhesion force and friction force are of the same order of

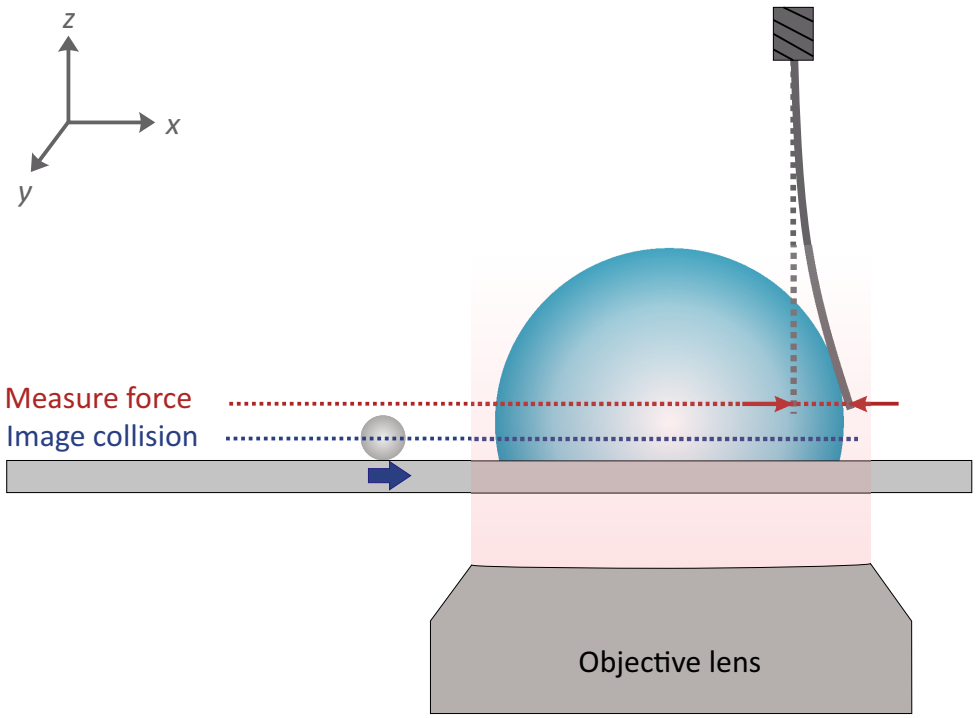

Figure 5.1: Experimental setup to image drop-particle collisions and to measure the force acting on the drop during the collision. The collision is imaged by focussing on a plane going through the centre of the particle (blue dotted line). Horizontal forces (along x) are measured by focussing on the bottom edge of the blade (red dotted line).

magnitude as the force between the drop and the particle. PDMS surfaces and glass particles satisfy this criterion and were therefore chosen as a model system.

PDMS surfaces also have a number of other desirable properties. It is transparent, which is a crucial requirement when using an inverted microscope. Its preparation is very reproducible. It is a widely used and well-understood model system. Furthermore, water drops can be moved on PDMS surfaces without breaking up into smaller droplets (no thread breakup).

Glass was chosen as model particle because glass consists mainly of silica, which is often a major constituent in real dust (e.g. sand, soil). Glass is also a widely used and well-understood material that can be produced reliably and sourced commercially.

5.2.2 Surfaces

PDMS surfaces Glass slides with a thickness of 270 µm were coated with Sylgard 184 PDMS, as described in section 3.1.1. PDMS surfaces were chosen because they are widely used, transparent (a requirement when using an inverted microscope) and can be prepared very reproducibly. The contact angle of water on the resulting surfaces was between 80° and 120° (section 3.3).

Lubricated PDMS surfaces Lubricated surfaces were prepared by spin coating 10 cSt PDMS oil onto the Sylgard 184 surfaces. A fluorescent marker was added to the PDMS oil so that it could be imaged with laser scanning confocal microscopy.

5.2.3 Particles

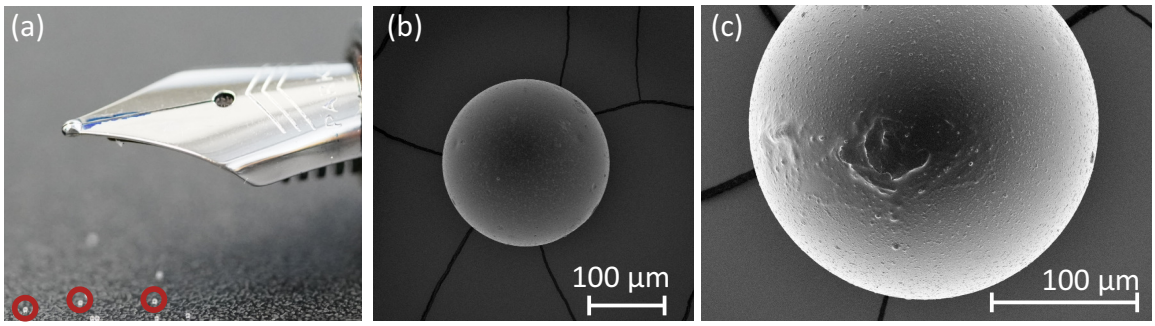

Figure 5.2: Glass particles with radii between 115 µm and 182 µm used in the experiments. (a) Size of the particles relative to a pen nib. (b) Magnified image of a particle, taken using scanning electron microscopy. (c) Particle with a defect. Thanks to Katharina Hegner for images (b) and (c).

Glass beads (from Polysciences Europe GmbH) with radii between 115 µm and 182 µm were used. The beads were spherical, but a small minority of them had defects (figure 5.2). An example of a particle with a defect is shown in figure 5.2 (c).

The particles were positioned on the PDMS surface using metal tweezers. Since metal is a good conductor, this ensures that the particles carry no surface charge prior to the experiments.[1]

PDMS spontaneously binds to glass, causing it to become more hydrophobic over time. Therefore, when the glass beads are placed on the PDMS surface, their surface properties change over time. Teisala *et al.* [103] have shown that the advancing and receding contact angles of water on glass increase with increasing exposure time to PDMS with a molecular weight of 6 000 g mol^{-1} (viscosity 100 cSt). However, the angles plateaued after around 3 h. To ensure that the surface properties of the particles were constant during the experiments, the particles were rolled over the PDMS surface a few times and then left to rest on it for a few hours before starting the drop-particle collision experiments.

Some of the glass particles were functionalised with PDMS by immersing them in PDMS oil (10 cSt) for 24 h. During this process, PDMS molecules adhere to the particles. To remove the excess oil afterwards, the particles were immersed in toluene, filtered with a filter paper, and finally rinsed with more toluene followed

[1]Interestingly, the particles showed significant repulsion towards a plastic micropipette tip. This could be observed by pouring a few particles on a petri dish and touching them with the tip of the pipette. This observation led me to the realisation that it might be important to ensure that the particles are not charged prior to the experiments.

by isopropanol. The resulting particles showed no difference compared to the initially unfunctionalised glass particles that were simply left on the PDMS surface for a few hours. This demonstrates that after a few hours of waiting the initially unfunctionalised particles were already in equilibrium with the surface, and therefore we can assume that the surface properties of the particles did not change over the course of the drop-particle collision experiments.

5.2.4 Drops

Most of the experiments were conducted using ultra pure (Milli-Q) water containing a fluorescent marker (Atto 488). The drop volume (between 3 µL and 10 µL) was chosen such that the force exerted by the particle on the drop was clearly visible when plotted on the same scale as the force required to push the drop alone. The water drops were assumed to be cloaked during the drop-particle collisions because they rolled on the PDMS surface for a few centimetres before each collision. Rolling over PDMS for a few centimeters causes uncrosslinked PDMS chains to accumulate on the drop-air interface. A water drop covered in PDMS has a surface tension of $65\,\mathrm{mN\,m^{-1}}$ (section 3.2).[2]

A few experiments were also performed with drops of diiodomethane, glycerol and glycerol-water mixtures.

5.3 Criterion for particle removal

There are two ways in which a drop can remove a particle from a surface: either by capillary force when the particle is at the drop-air interface, or by viscous force when the particle is submerged inside the drop.

For simplicity, I first consider a two-dimensional analogue of the problem. When a planar liquid-air interface collides with a stationary particle on a flat surface, the particle can either remain at the interface or enter the liquid. For the particle to remain attached to the liquid-air interface, it has to slide or roll (or a combination of both) over the surface such that its centre of mass moves at the same speed as the interface. Therefore, it must first be accelerated to match the speed of the interface. Once the particle starts moving (rolling/sliding) relative to the surface, it will encounter resistive forces, such as friction between the particle and the surface. The resistive forces, F_R, depend on whether the particle rolls or slides. The criterion

[2]Hourlier-Fargette *et al.* [63] showed that moving drops become cloaked after rolling on PDMS for a few millimetres. The authors showed that the larger the drop volume, the further the drop has to roll before becoming fully cloaked. The smallest drop volume that they used was 14 µL, for which the distance taken for the drop to become cloaked was less than 5 mm. Note that the authors used a glycerol/water (60%/40%) mixture rather than pure water, but this is not expected to significantly affect the distance over which the drop has to be roll before getting cloaked.

for the particle to stay attached to the interface can be written in the form of Newton's second law:

$$F_\gamma^{\max} \geq F_\mathrm{R} + F_\mathrm{inertial}, \tag{5.1}$$

where $F_\gamma^{\max}$ is the maximum capillary force that the interface can exert on the particle, and $F_\mathrm{inertial} = ma$ (m is the mass of the particle, a is its acceleration) is the inertial force required to accelerate the particle.

For small particles, F_inertial is negligible since m is proportional to R^3, whereas F_γ and F_R are proportional to R (appendix B.1).[3] In this case, equation 5.1 can be simplified to

$$F_\gamma^{\max} \geq F_\mathrm{R}. \tag{5.2}$$

Therefore, the particle remains attached to the interface when the maximum capillary force is greater than the resistive force that needs to be overcome to move the particle on the surface.

In contrast, when $F_\gamma^{\max} < F_\mathrm{R}$, the capillary force is not sufficiently strong to overcome resistive forces. Consequently, the particle crosses the interface and fully enters the liquid.

When the particle is inside the liquid, it experiences a viscous force, F_η, due to the flow of water around it. The particle moves together with the liquid when

$$F_\eta \geq F_\mathrm{R}. \tag{5.3}$$

Therefore, a particle can be removed from a surface either by the capillary force or by the viscous force, if at least one of these forces is greater than the resistive force that needs to be overcome to move the particle on the surface.

For typical sliding speeds of water drops on most surfaces (windows, leaves, windshields), viscous drag is negligible compared to the capillary force, $F_\eta \ll F_\gamma^{\max}$. Therefore, when using water drops to remove particles, the only relevant criterion is equation 5.2. However, as will be discussed in section 5.6, F_η becomes dominant when more viscous liquids are used.

5.4 Particle remains attached to the drop

In this section, I describe the collision between a water drop and a particle on a PDMS surface at a low speed. The outcome described below is observed for speeds up to $\approx 300\,\mu\mathrm{m\,s^{-1}}$.

[3] For small R, $R^3 \ll R$, and therefore $F_\mathrm{inertial} \ll F_\gamma$. A good estimate for 'small' is anything below 1 mm. F_R is usually proportional to R since the friction force $F_\mathrm{F} \propto F_\mathrm{adh}$, where F_adh is the adhesion force, which is proportional to R according to the JKR theory (equation 1.50).

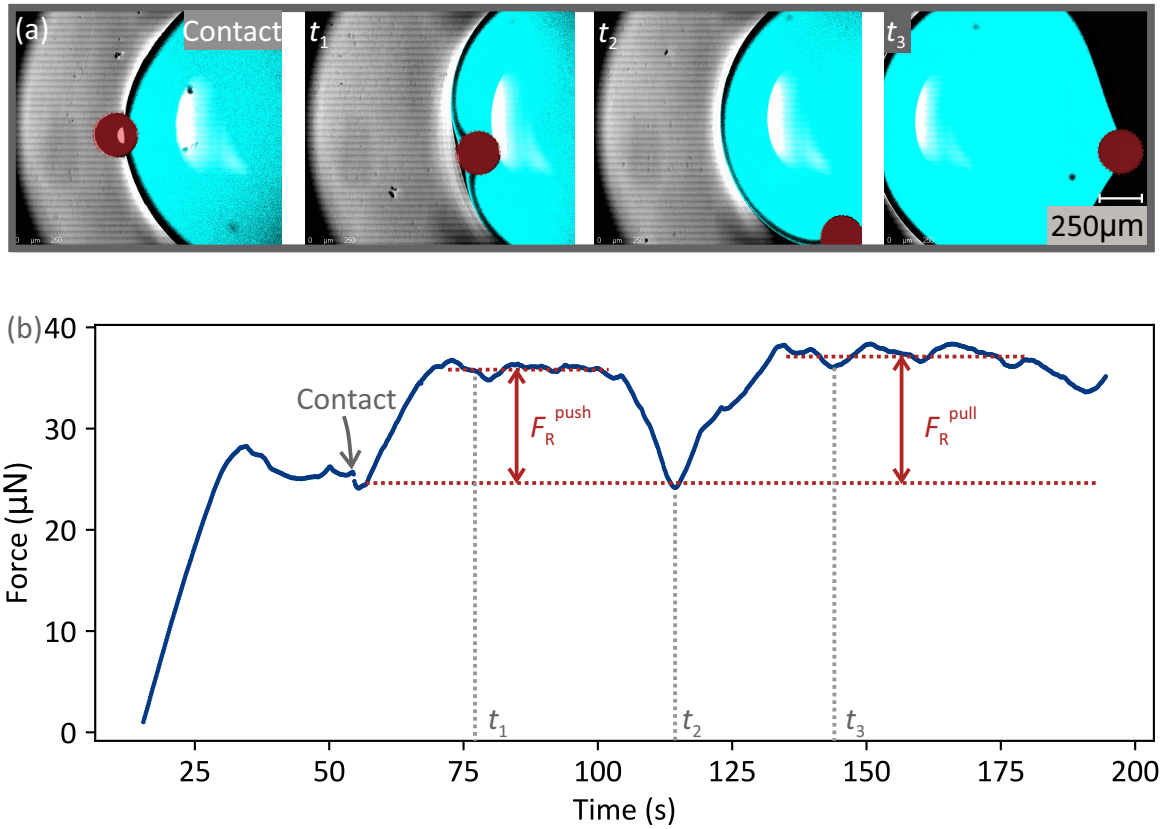

Figure 5.3: (a) Collision between a drop (cyan, volume 3 µL) and a particle (radius 115 µm, dark red) at 50 µm s^{-1} [80]. The focus was in a horizontal plane through the centre of the particle. (b) Horizontal force acting on the drop before and during the collision. F_R^{push} (F_R^{pull}) is the force required to push (pull) the particle.

Experiment A particle (radius 115 µm) was placed a few millimetres in front of a water drop and the surface was moved at constant speed while the drop was kept in a fixed position (figure 5.1).

Before the collision Figure 5.3 shows a collision at 50 µm s^{-1}. When the surface was set into motion, the force increased until it reached a steady value at ≈ 30 s. The plateau between 30 s and 55 s corresponds to the friction force between the drop and the surface.

Initial contact At ≈ 55 s the particle made contact with the drop. This event is often termed 'snap-in'. During snap-in, a water meniscus forms around the particle. This is seen as a small dip in the force curve (labelled 'contact').

Particle in front of drop Then, the force increased until the applied force was equal to the resistive force that needs to be overcome in order to move the particle relative to the surface. The plateau between contact and t_2 corresponds to the force required to push the particle at 50 µm s^{-1} ($F_R^{push} = 10 \pm 1$ µN) .

Particle moves to the side However, this configuration (when the particle is in front of the drop) is unstable due to the convex curvature of the drop. Any deviation from a head-on collision results in an asymmetry in the capillary force, causing the particle to move sideways. Experimentally, even when a perfect head-on collision is achieved, an asymmetry arises when the particle moves over a surface inhomogeneity. Therefore, the particle moved around the drop's base. At t_2, it was at the lateral side of the drop. In this position, the force had the same value as before the collision since the capillary force had no component acting along the x-axis (defined in figure 5.1).

Particle at the rear side of the drop After t_2, the particle was at the rear side of the drop. The particle remained attached to the drop while the surface continued to move at $50\,\mu\mathrm{m\,s^{-1}}$. The force required to pull the particle was $F_{\mathrm{R}}^{\mathrm{pull}} = (12 \pm 2)\,\mu\mathrm{N}$.

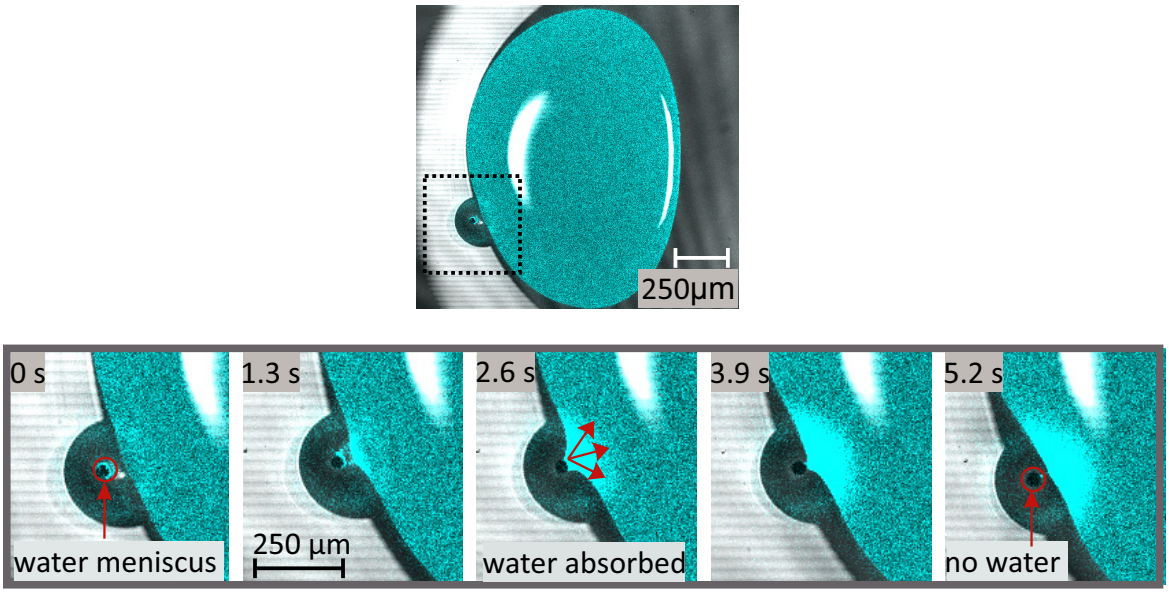

Figure 5.4: Contact between a water drop and a particle that is initially surrounded by a small water meniscus. Upon contact, the water in the small meniscus is absorbed by the drop. Water in the small meniscus appears brighter than water in the drop because the dye concentration was higher in the meniscus.

Collision with a wet particle The same behaviour (as in figure 5.3) was also observed when the particle was initially surrounded by a small water meniscus. In general, a small meniscus could be due to condensation of water vapour from the atmosphere or due to residual water from a previous collision. In this case, the water meniscus around the particle was quickly absorbed by the drop (figure 5.4) and rest of the collision looked exactly the same as when the particle was initially dry.

5.4.1 Details of the particle's motion

In this section, I investigate whether the particle rolls or slides and whether it aquaplanes when it is pulled by the drop.[4] These details are important because they influence the resistive force experienced by the particle when it moves on the surface.

5.4.1.1 Does the particle roll or slide?

To determine whether the particle rolls or slides over the surface, I zoomed into a particle that had microscopic defects. The defects made it possible to deduce how the particle moved.

When the particle was pulled by a drop at $50\,\mu m\,s^{-1}$, the defects periodically appeared into focus as shown in figure 5.5 (a). Therefore, the particle rolled. The time taken for the defects to perform a complete revolution was 16 s, which corresponds to the time period of pure rolling.[5]

The defects caused the particle to roll unevenly, resulting in a periodic motion of the water-air-particle contact line. In figure 5.5 (b), the contact angle, Θ, of water on the particle and the x-coordinate, x_{CL}, of the contact line relative to the centre of the particle are plotted. Each data point for Θ and x_{CL} corresponds to the average value of the upper and lower contact points [two green dots in figure 5.5 (a), middle column]. Both the contact line position and the contact angle oscillated with a time period equal to that of rolling (16 s).

The advancing angle is the maximum angle ($\Theta_A \approx 100^\circ$) when the contact line advanced on the particle. The receding angle is the minimum angle ($\Theta_R \approx 75^\circ$) when the contact line receded on the particle. These contact angles are higher than what would typically be expected for water on (clean) glass because uncrosslinked PDMS chains from the surface adhered to the particle [103].

Calculating the capillary force from the images Next, I calculate the capillary force that the drop exerts on the particle purely from the image series (figure 5.5) and compare the result to the measured force F_R^{pull} (figure 5.3) to check if the two values are consistent.

How to calculate the force from the images? The net capillary force, $\boldsymbol{F}_\gamma$, acting on the particle is obtained by integrating the surface tension vector around the contact line. To perform the integral, the contact line is assumed to be circular and the contact angle is assumed to be uniform along the contact line. Due to symmetry

[4] Aquaplaning is the phenomenon that causes roads to become slippery when wet.

[5] Pure rolling is when the particle rolls at the same speed as the surface. The time period of pure rolling is $T = 2\pi R/v$, where R is the radius of the particle and v is the speed of the surface. $T = 16\,s$ for $R = 125\,\mu m$ and $v = 50\,\mu m\,s^{-1}$.

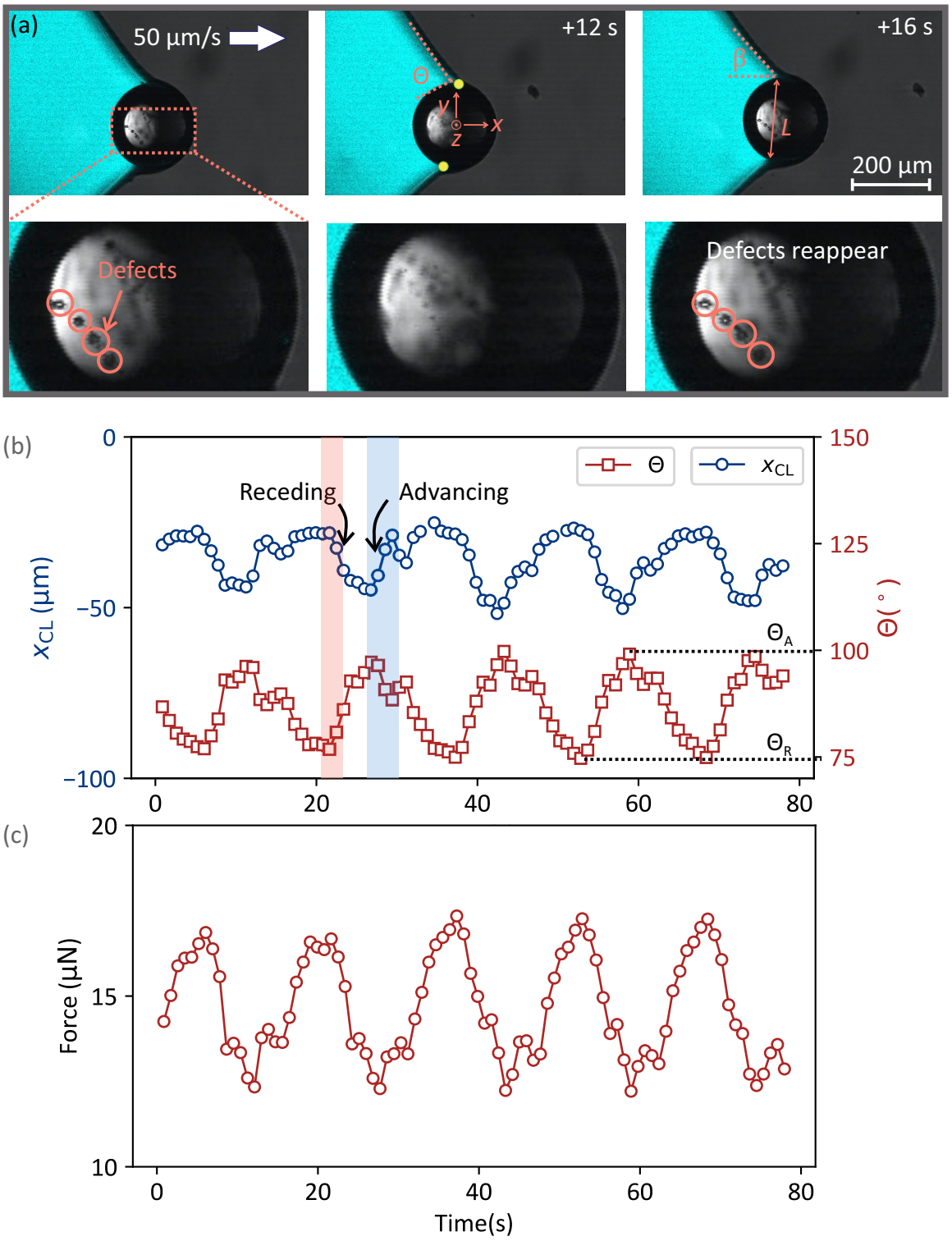

Figure 5.5: Water drop pulling a particle (radius 125 µm) with defects [80]. (a) The defects appear in focus every 16 s. The green dots (middle row) highlight the position of the contact line of diameter L. Θ is the contact angle and β is the angle between the drop-air interface and the x- axis. (b) Position of the contact line (x_{CL}) and contact angle as a function of time. x_{CL} is defined relative to centre of the particle. Both Θ and x_{CL} are averages of the values measured at the two green dots in (a). (c) Capillary force acting on the particle, calculated from the image series in (a).

of the surface tension vector about the xz plane, the force components along the y-axis cancel, leaving only the components parallel to the xz plane, $|\boldsymbol{F_{xz}}| = |\boldsymbol{F_{\gamma}}| \cos\beta$, where β is the angle between the surface tension vector and the x-axis [defined in figure 5.5 (a)]. The net force pulling the particle parallel to the surface is given by the horizontal component of $\boldsymbol{F_{xz}}$,

$$F_x = |\boldsymbol{F_{xz}}| \sin A = \pi L \gamma \cos\beta \sin A, \tag{5.4}$$

where πL is the circumference of the contact line, A is the angle between the surface and the plane containing the contact line and γ is the magnitude of the surface tension vector. $A \approx 40°$, based on the three-dimensional shape of the meniscus (figure 5.6).[6]

F_x is plotted as a function of time in figure 5.5 (c) using $A = 40°$. The average force calculated from equation 5.4 is $\approx 14\,\mu N$ [figure 5.5 (c)], which is in good agreement with the measured force, $F_R^{pull} = (12 \pm 2)\,\mu N$ [from figure 5.3 (b)].

5.4.1.2 Does the particle aquaplane?

To determine whether the particle aquaplaned during motion, I imaged the contact between the particle and the surface (figure 5.7). The contact region remained dry, demonstrating that the particle did not aquaplane.

5.4.2 Resistive forces

Now that I have shown that the particle rolls over the surface without aquaplaning, the physical origins of the resistive force (F_R^{push} and F_R^{pull}) that the particle experiences when it is pushed/pulled by the drop can be determined. Since both F_R^{push} and F_R^{pull} should have similar origins, I will drop the superscript and call both these forces F_R.

F_R has three contributions: (1) F_S due to solid-solid rolling friction, (2) $F_{\Delta\Theta}$ due to resistive capillary torque (introduced in chapter 4) and (3) F_η due to viscous drag. In the following, I will elaborate on each of these contributions.

5.4.2.1 Surface friction

F_S originates from viscoelastic dissipation in the PDMS surface and from molecular attraction forces between the particle and the surface [7, 96, 52].[7] As the particle rolls, the energy required to peel the rear contact is greater than the energy recovered when closing the front contact, thus giving rise to a rolling resistance [7].

[6] In general, I expect the shape of the water meniscus to change with speed and therefore A may deviate from 40° depending on the speed at which the surface moves. However, the temporal resolution of the microscope is insufficient to accurately image the meniscus in three dimensions during motion.

[7] PDMS is a viscoelastic material.

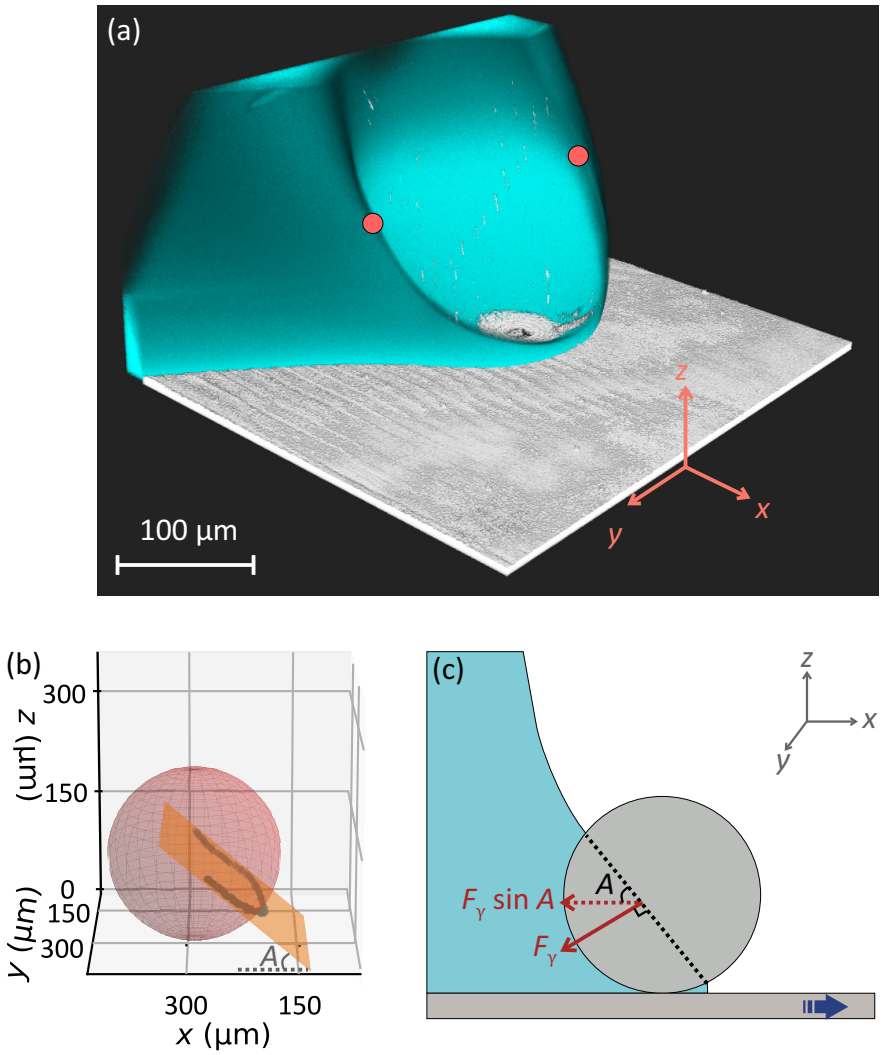

Figure 5.6: Water meniscus around a particle [80]. (a) Three-dimensional confocal image of the water meniscus (cyan) surrounding a stationary particle (not drawn) of radius 125 µm. The image is subject to an optical artefact above the particle's centre since the particle obstructs fluorescent light emitted by the drop. Therefore, the shape of the meniscus is only accurate below the red dots. (b) The lower half of the three-phase contact line [extracted from (a)] was circular with $A = 40°$. (c) Schematic side view showing the capillary force and its horizontal projection.

To determine F_S, I measured the force to push a particle by the blade (without the drop) at constant speeds [figure 5.8(a)]. F_S increased at a decreasing rate with speed.[8]

5.4.2.2 Resistive capillary torque

The second contribution to the resistive force is due to capillary torque ($M_{\Delta\Theta}$, the subscript stands for 'contact angle hysteresis') opposing rolling at the drop-air

[8]During these experiments, the particle rolled on the surface while sliding relative to the blade. Thus, the measured force is influenced by friction between the blade and the particle. However, the friction contribution due to the blade is expected to only be $\approx 10\%$ of the measured F_S since the coefficient of sliding friction between the blade and PDMS-coated particle is low (≈ 0.1 [12]).

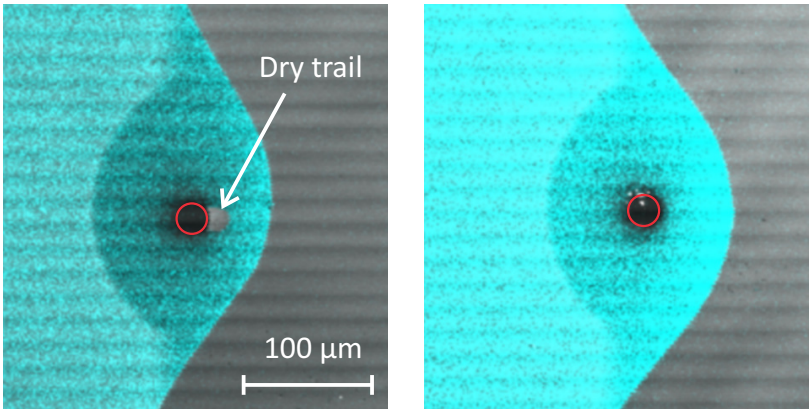

Figure 5.7: Imaging the contact between the particle and the surface by focussing on a plane going through the surface-particle contact during motion at $50\,\mu m\,s^{-1}$. The contact area between the particle and the surface appears black (highlighted by the red circle) and water appears cyan. In some cases, there was a dry trail directly behind the particle (left image). However, for the majority of cases, there was no clear dry trail behind the particle (right image). Regardless of whether there is a dry trail or not, the region under the particle always remained dry.

interface. This contribution has been discussed in detail in chapter 4. Here, I only provide a brief intuition for this effect. Consider a particle rotating counterclockwise at an interface. The right side recedes and has an angle of Θ_R with the interface whereas the left side advances and has an of angle Θ_A, as shown in the inset of figure 5.8 (b). This asymmetry gives rise to a resistive torque,

$$M_{\Delta\Theta} = \frac{24}{\pi^3}\gamma RL(\cos\Theta_R - \cos\Theta_A), \tag{5.5}$$

where R is the radius of the particle and L is the diameter of the three-phase contact line. The effective force required to overcome the capillary torque is

$$F_{\Delta\Theta} = \frac{24}{\pi^3}\gamma L(\cos\Theta_R - \cos\Theta_A). \tag{5.6}$$

For a particle with $L = 2R = 364\,\mu m$, $\Theta_R = 75^\circ$ and $\Theta_A = 100^\circ$, we obtain $F_{\Delta\Theta} \approx 8\,\mu N$.

5.4.2.3 Viscous drag

As the particle rolls at the air-water interface, it creates a flow in the water due to the no-slip boundary condition between the particle's surface and the water. This results in a viscous drag, F_η.

However, it turns out that F_η is negligible compared to $F_{\Delta\Theta}$ due to the small capillary number, $Ca = \eta v/\gamma \approx 10^{-5} \ll 1$, where η is the dynamic viscosity of water, v is the rolling speed of the particle and γ is the surface tension of the drop. Assuming a Stoke's drag gives a viscous force $6\pi\eta Rv \approx 1 \times 10^{-8}\,N$, which is two orders of magnitude lower than both F_S and $F_{\Delta\Theta}$. Therefore, F_η can be neglected and $F_R = F_S + F_{\Delta\Theta}$.

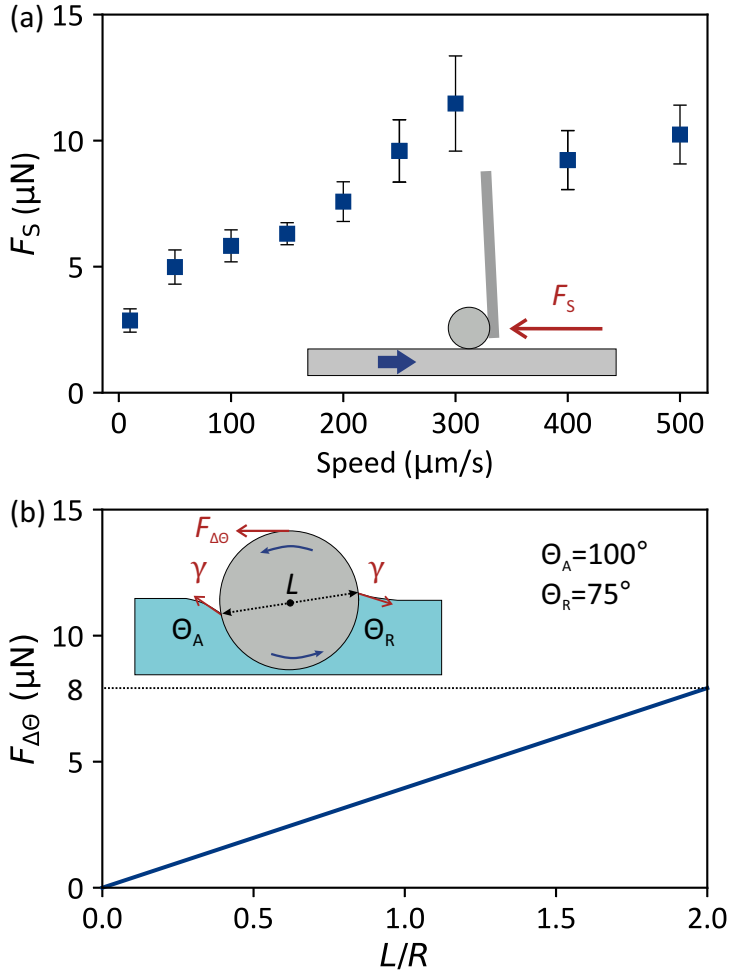

Figure 5.8: (a) Force required to push a particle on a dry PDMS surface at different speeds [80]. Error bars correspond to the standard deviation of the measurements and are due to surface inhomogeneities. (b) Resistive capillary force (equation 5.6) on a particle (radius 182 µm) rolling at a water-air interface (assumed to be cloaked, $\gamma = 65\,\mathrm{mN\,m^{-1}}$).

5.4.2.4 Do the proposed contributions add up?

Results Figure 5.9 compares $F_S + F_{\Delta\Theta}$ to the measured values of F_R when the particle was pushed or pulled by a water drop.

For a systematic comparison, F_S, F_R^{push} and F_R^{pull} were all measured using the same particle and all the measurements were performed along the same track on the surface. There is a very good agreement between the sum of the two contributions and the measured F_R.

Discussion Surprisingly, F_R showed no clear speed dependence. This is probably because $F_{\Delta\Theta}$ decreases with speed and balances the increase in F_S such that their sum, F_R, is approximately constant. To understand why $F_{\Delta\Theta}$ could decrease with speed, consider a particle attached to the rear side of the drop. When the particle is in equilibrium at the drop-air interface, half of it will lie inside the water phase since the average contact angle of water on the particle is $\approx 90°$ in our case. In this

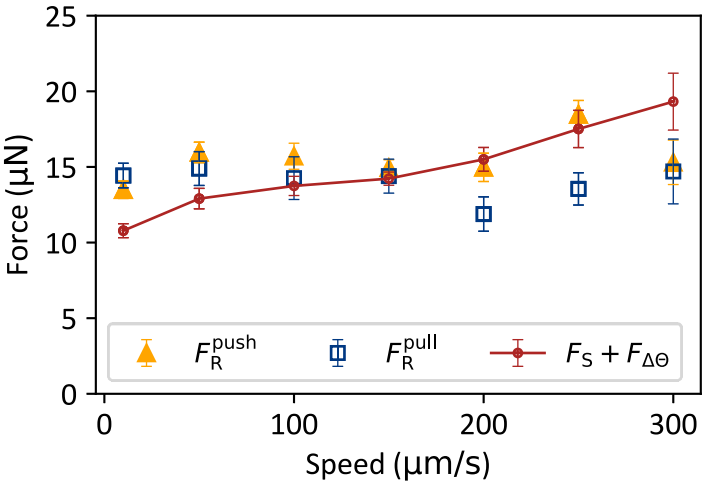

Figure 5.9: Resistive force experienced by a particle (radius 182 µm) when it was pushed (orange triangles) or pulled (blue squares) by a water drop [80]. The red circles and line were obtained by adding the two proposed resistive contributions, F_S and $F_{\Delta\Theta}$. Error bars correspond to the standard deviation of the measurements due to surface inhomogeneities.

configuration, the contact line radius is equal to the radius of the particle. However, when the particle moves with the drop, the net capillary force has a component pulling the particle towards the drop. To produce this force, the contact line has to slide over the particle such that the net capillary force has a component pointing towards the drop, as in figure 5.6 (c). As the contact line slides, the particle moves further out of the drop and the contact line radius, L, decreases, which corresponds to a decrease in $F_{\Delta\Theta}$.

Furthermore, it is likely that the angular tilt of the contact line [A in figure 5.6 (c)] is a function of speed, causing both the magnitude and the direction of the net capillary force vector to change with speed.

Another important consideration is that when the particle is attached to the drop, F_S may no longer take the same values as measured in dry conditions. The normal adhesion force between the particle and the surface will be influenced by the vertical component of capillary force acting at the air-water-particle contact line and by van der Waals forces which act through water instead of air. Since rolling friction on elastomers depends on the normal force [7], F_S will also change.

Given all the complexity, it is perhaps surprising that $F_S + F_{\Delta\Theta} \approx F_R$.

5.5 Particle detaches from the drop

Particle enters the drop When the collision was performed at 500 µm s^{-1}, the particle entered the drop (figure 5.10). The force reached a maximum of $F_\gamma^{push} = 16$ µN when the particle crossed the drop-air interface.

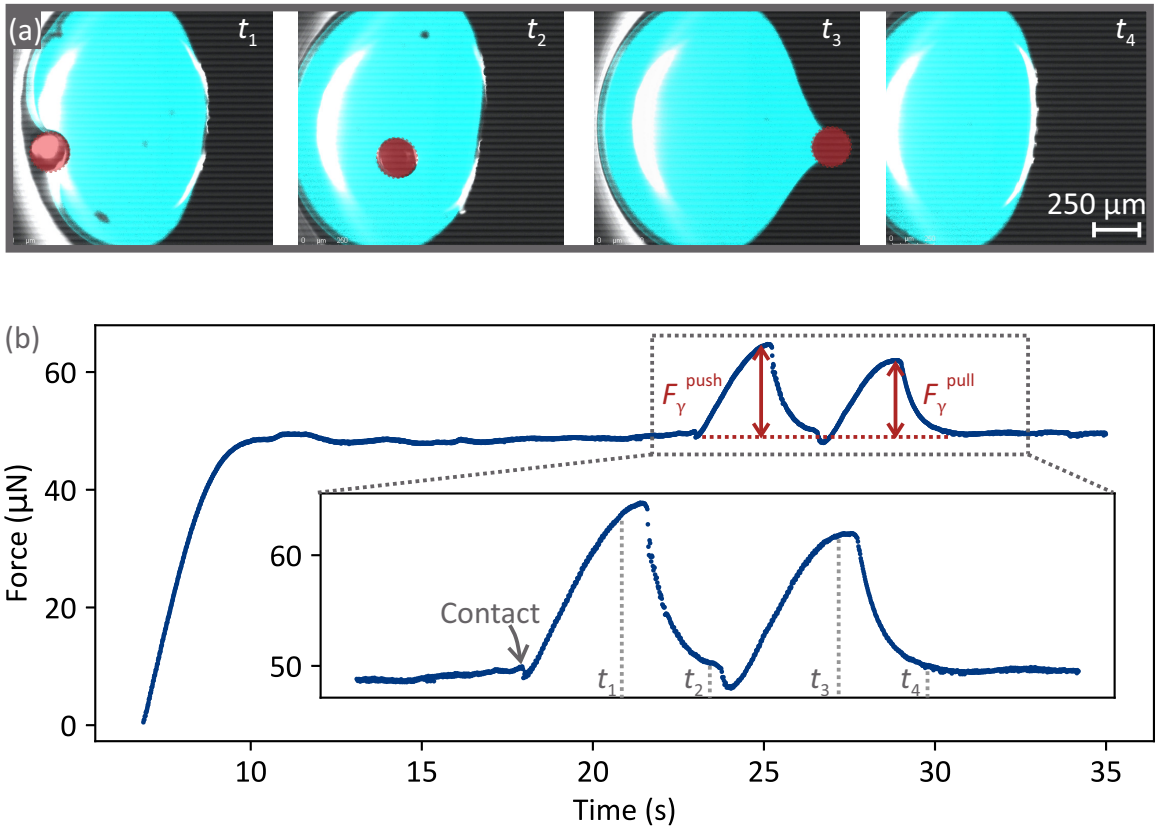

Figure 5.10: Collision between a particle (radius 115 µm) and a water drop (volume 3 µL) at 500 µm s^{-1} [80]. (a) The focus was on a horizontal plane going through the particle's centre. (b) Force acting on the drop. The particle was initially 1.2 cm away from the drop and collided with the drop at ≈ 23 s.

Particle inside the drop The force decreased to the same value as before the collision when the particle was inside the drop (t_2). This demonstrates that viscous drag is negligible. The viscous drag is given by equation 1.37:

$$F_\eta \approx 1.7 \times 6\pi\eta R^2 \frac{v_D}{H}. \tag{5.7}$$

where η is the dynamic viscosity of water and R is the particle's radius. $v_D R/H$ is the average velocity of the flow around the particle, where v_D is the speed of the drop relative to the surface and H is the drop's height.

F_η is of the order of 1 nN, which is indeed negligible compared to the capillary force. Consequently, a particle that crosses the front side of the drop will easily move through the drop, reaching the rear interface.

Particle exits the drop The particle detached from the drop just after t_3, exerting a maximum force $F_\gamma^{pull} = 13$ µN. From this measurement, we can conclude that the capillary force is much more significant than the viscous force and is therefore the relevant force when removing particles using water drops.

Does the particle have time to roll/slide during entry? To determine whether particles moved (rolled/slid) relative to the surface as they crossed the drop-air interface, the positions of the centres of mass of four particles were recorded during entry. In figure 5.11, each colour corresponds to a different particle colliding with the same drop in succession. The drop was fixed in place and the particles were placed in a line (along the axis of motion) on the PDMS surface. The position of the centre of mass of each particle was monitored as the surface moved at constant speed. Before making contact with the drop, the particles moved together with the surface at $500\,\mu m\,s^{-1}$. This can be seen in figure 5.11, where the scatter points initially follow a straight line with a gradient of $500\,\mu m\,s^{-1}$. However, when the particles made contact with the drop, their centres of mass slowed down. This can be seen in figure 5.11, where the scatter points deviate from the $500\,\mu m\,s^{-1}$ line after the particle has made contact with the drop. A reduction in the speed of the particle implies that there is relative motion (rolling and/or sliding) between the particle and the surface.

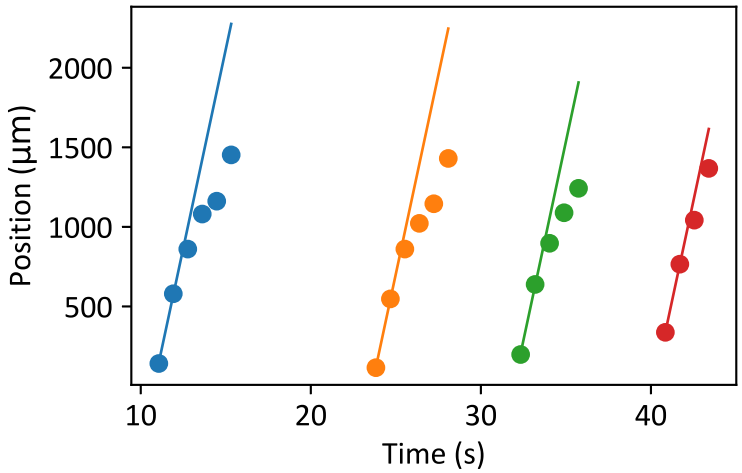

Figure 5.11: Positions of the centre of masses of four particles entering a stationary drop on a surface moving at $500\,\mu m\,s^{-1}$. Each colour corresponds to a different particle and the straight lines correspond to a speed of $500\,\mu m\,s^{-1}$. The points deviate from the lines when the particles collide with the drop, demonstrating that the particles slowed down during the collision.

5.5.1 Maximum capillary forces

5.5.1.1 Prediction

The maximum capillary force that the drop can exert on the particle depends on whether the particle rolls or slides, the contact line geometry and the contact angle between the particle and the drop. To estimate the maximum capillary force I first consider a particle crossing an air-water interface perpendicularly (neglecting the PDMS surface).

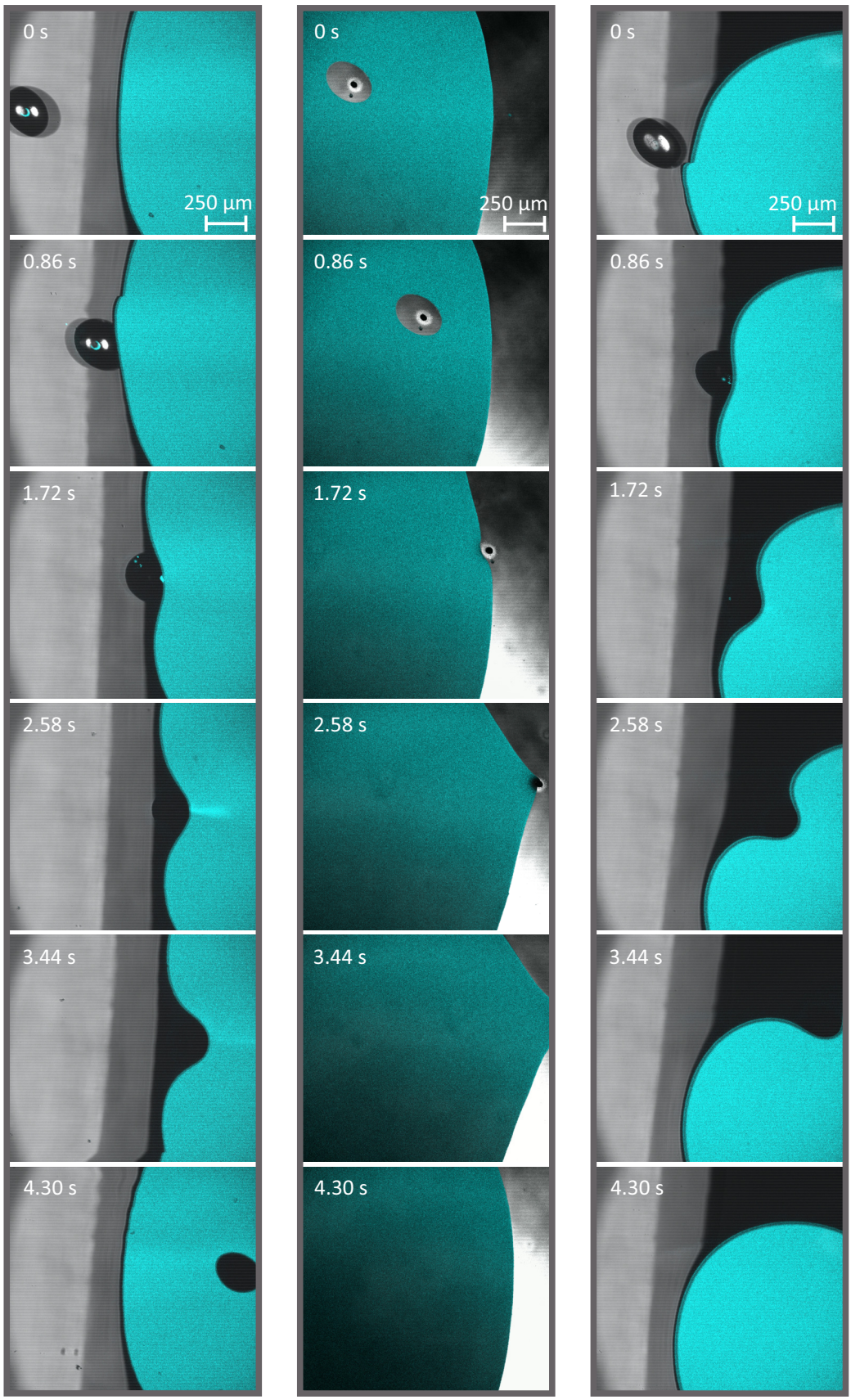

Figure 5.12: Closeup of collisions at 500 µm s^{-1} during entry (leftmost column) and exit (middle column). The rightmost column shows a non-head-on collision at the same speed. The particle did not enter the drop but went sideways.

Entry (Slide) For a non-rotating (sliding) particle, the maximum capillary force with which the drop can push the particle during entry is given by equation 1.27:

$$F_{\text{slide}}^{\text{push}} = 2\pi R\gamma \sin^2 \frac{\Theta_{\text{A}}}{2}, \tag{5.8}$$

where R is the radius of the particle and Θ_{A} is the advancing contact angle of water on the particle.

Entry (roll) When the particle rolls during entry, the maximum capillary force is reduced and is given by equation 4.40:

$$F_{\text{roll}}^{\text{push}} = \frac{4\pi}{\Theta_{\text{A}} - \Theta_{\text{R}}} \gamma R \sin^2 \left(\frac{\Theta_{\text{R}} + \Theta_{\text{A}}}{4} \right) \sin \left(\frac{\Theta_{\text{A}} - \Theta_{\text{R}}}{2} \right). \tag{5.9}$$

Exit (Slide) The maximum capillary force with which the drop can pull a non-rotating particle when it exits the drop is given by equation 1.26:

$$F_{\text{slide}}^{\text{pull}} = 2\pi R\gamma \cos^2 \frac{\Theta_{\text{R}}}{2}. \tag{5.10}$$

Exit (Roll) When the particle rolls as it exits the drop, the magnitude of the maximum capillary force is reduced and is given by equation 4.39:

$$F_{\text{roll}}^{\text{pull}} = \frac{4\pi}{\Theta_{\text{A}} - \Theta_{\text{R}}} \gamma R \cos^2 \left(\frac{\Theta_{\text{R}} + \Theta_{\text{A}}}{4} \right) \sin \left(\frac{\Theta_{\text{A}} - \Theta_{\text{R}}}{2} \right). \tag{5.11}$$

5.5.1.2 Comparing predicted and measured forces

Figure 5.13 (b) compares the predicted maximum forces to the maximum forces measured when a particle entered and exited a drop.

All the experiments were performed at $500\,\mu\text{m}\,\text{s}^{-1}$ along the same track on the surface and with the same particle. The particle and the drop were carefully aligned such that they collided head-on. Setting up a head-on collision is crucial, otherwise a lower force is measured and the particle might not even enter the drop (as shown in the rightmost column of figure 5.12).[9]

The predictions are of the correct order of magnitude, but are around two times larger than the measured forces. This discrepancy is likely because the predictions assume that the angle A (defined in figure 5.6) between the surface and the water-air-particle contact line is 90°. But in general, A differs from 90°. Since the measurements

[9]Setting up a head-on collision, like the one shown in the leftmost column of figure 5.12, requires placing the particle with micrometre precision such that the particle and the drop are aligned exactly parallel to the axis along which the surface moves. To achieve this, I used the drop to place the particle. We have seen that when a particle is pulled by the rear side of the drop, it follows the drop along the head-on axis, as shown in figure 5.3 (c) (time t_3). Once the particle is in this configuration, I detached it from the drop by suddenly increasing the speed. Then, I performed the collision experiment by moving the drop back towards the particle at constant speed.

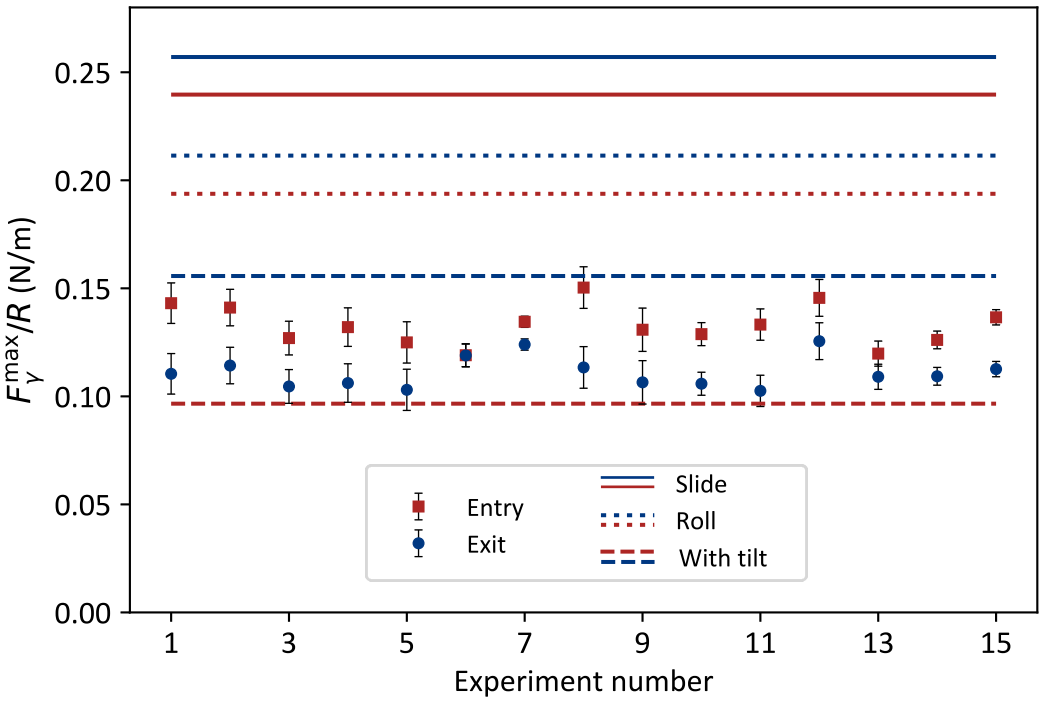

Figure 5.13: Maximum force measured when a 182 µm particle entered (red squares) and exited (blue circles) a water drop (volume 8-10 µL) at 500 µm s^{-1} (data points are from [80]). The error bars correspond to the standard deviations in the drop friction due to surface inhomogeneities. The solid horizontal lines correspond to the predicted force for a sliding particle [equations 5.8 (red) and 5.10 (blue)]. The dotted lines correspond to a rolling particle [equations 5.9 (red) and 5.11 (blue)]. The dashed lines takes into account the tilt of the three-phase contact line with respect to the surface (ignoring rolling) [obtained by maximising equations 5.13 (red) and 5.15 (blue)].

only capture the horizontal component of the capillary force, the predictions provided by equations 5.8-5.11 are indeed expected to be higher.

To reconcile the predicted and measured forces, only the horizontal projection of the predicted force has to be considered when calculating the maximum force. Therefore, $|\boldsymbol{F}_\gamma| \sin A$ has to be maximised instead of $|\boldsymbol{F}_\gamma|$. An expression for the maximum horizontal component of the capillary force (ignoring rolling) was derived by Leenaars (1989) [75] and Heckenthaler *et al.* (2019) [58]. They proposed that equation 5.10 should be multiplied by $\sin \Theta_S$, where Θ_S is the contact angle between the drop and the flat surface (80° - 100° in our case, section 3.3.2). However, the experiments presented in this chapter demonstrate that this correction still overestimates the predicted force since Θ_S is generally not equal to A, as shown in figure 5.6, where A was 40°.

A model to account for the contact line tilt The reason why Θ_S is, in general, not equal to A can be understood based on figure 5.14. In equilibrium, $\beta = 0$ and therefore, $A = \Theta_S$. However, as the upper part of the interface advances over the particle, $\beta \neq 0$ and $A = \Theta_S + \beta$. The lower part of the interface remains pinned such

that the contact angles on both the particle and the surface are fulfilled. The net capillary force acting on the particle is

$$\boldsymbol{F_\gamma} = 2\pi R\gamma \sin\phi \sin(\Theta_\mathrm{A} - \phi)\ \hat{\boldsymbol{n}}$$

$$= 2\pi R\gamma \sin(\Theta_\mathrm{A} - \beta) \sin\beta\ \hat{\boldsymbol{n}}, \tag{5.12}$$

where $\hat{\boldsymbol{n}}$ is the unit vector normal to the plane containing the contact line and $\phi = \Theta_\mathrm{A} - \beta$ (based on the geometry), where $\pi - \Theta_\mathrm{A} \leq \beta \leq \Theta_\mathrm{A}$. The horizontal component (along x as defined in figure 5.14) of $\boldsymbol{F_\gamma}$ is

$$F_x^{\mathrm{entry}} = 2\pi R\gamma \sin(\Theta_\mathrm{A} - \beta) \sin\beta \sin(\beta + \Theta_\mathrm{S}). \tag{5.13}$$

The vertical (downwards) component of the capillary force is

$$F_y^{\mathrm{entry}} = -2\pi R\gamma \sin(\Theta_\mathrm{A} - \beta) \sin\beta \cos(\beta + \Theta_\mathrm{S}). \tag{5.14}$$

Equations 5.13 and 5.14 are valid for a particle entering a drop. The corresponding equations for a particle exiting a drop are obtained by replacing Θ_A by $\pi - \Theta_\mathrm{R}$ and Θ_S by $\pi - \Theta_\mathrm{S}$.[10] The horizontal capillary force pulling the particle towards the drop during exit is

$$F_x^{\mathrm{exit}} = 2\pi R\gamma \sin(\Theta_\mathrm{R} + \beta) \sin\beta \sin(\Theta_\mathrm{S} - \beta), \tag{5.15}$$

where $-\Theta_\mathrm{R} \leq \beta \leq \pi - \Theta_\mathrm{R}$ The vertical (downwards) component of the capillary force during exit is

$$F_y^{\mathrm{exit}} = 2\pi R\gamma \sin(\Theta_\mathrm{R} + \beta) \sin\beta \cos(\beta - \Theta_\mathrm{S}). \tag{5.16}$$

The maximum horizontal capillary force is obtained by maximising equations 5.13 and 5.15 with respect to β. The results are plotted as dashed lines in figure 5.13 and show very good agreement with the measured forces.

5.6 Different liquids

So far, I have only considered water drops. Water is the most common liquid in nature. However, its low viscosity and high surface tension is a relatively unique combination (figure 5.15). When different liquids are used, both the maximum capillary force and the viscous force change. In the following, I will first discuss how the capillary force changes when different liquids are used. Then, I will discuss the regime when the viscous force becomes significant.

[10] Note that during entry Θ_S is given by the advancing contact angle of water on the surface (120°), whereas during exit, Θ_S corresponds to the receding contact angle (80°).

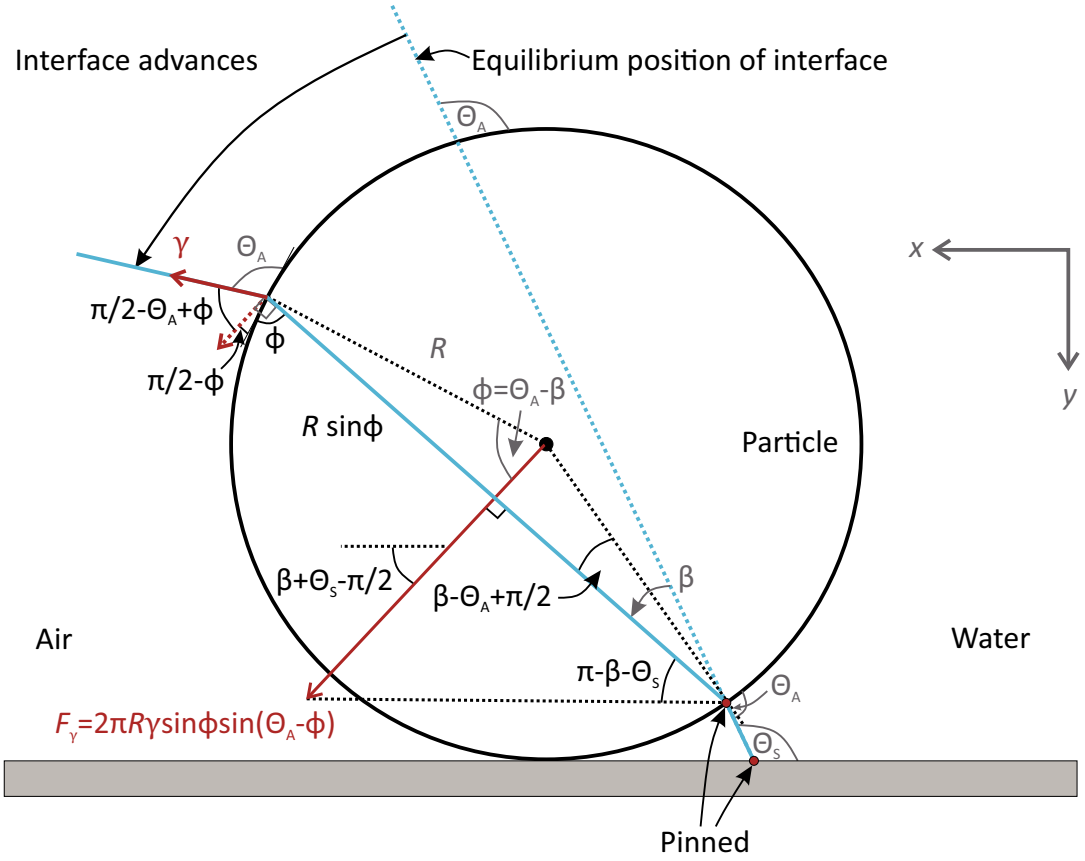

Figure 5.14: An air-water interface (blue line) moving across a fixed particle. This scenario is equivalent to a particle entering a fixed drop from left to right (ignoring rolling). The lower side of the interface is pinned because moving away from the position sketched in the figure would violate the contact angles Θ_A or Θ_S, or require the interface to bend, which is not feasible because it would cause a very large Laplace pressure that would differ from the rest of the drop. Forces are written in red. The angles written in grey are defined quantities. Angles written in black are deduced from the ones written in grey.

5.6.1 Capillary forces

How does the capillary force change when different liquids are used? The maximum capillary forces (when a particle entered/exited a drop) were measured for three liquids: glycerol, water and diiodomethane. The surface tensions of the liquids are given in the table 5.1.

Table 5.1: Surface tension and dynamic viscosity of the different liquids used. The values correspond to pure liquids at a temperature of 20 °C.

Liquid	γ (mN m^{-1})	η (mPa s)
Water	72.8	1
Glycerol	64.0	1412
Diiodomethane	50.8	2.6

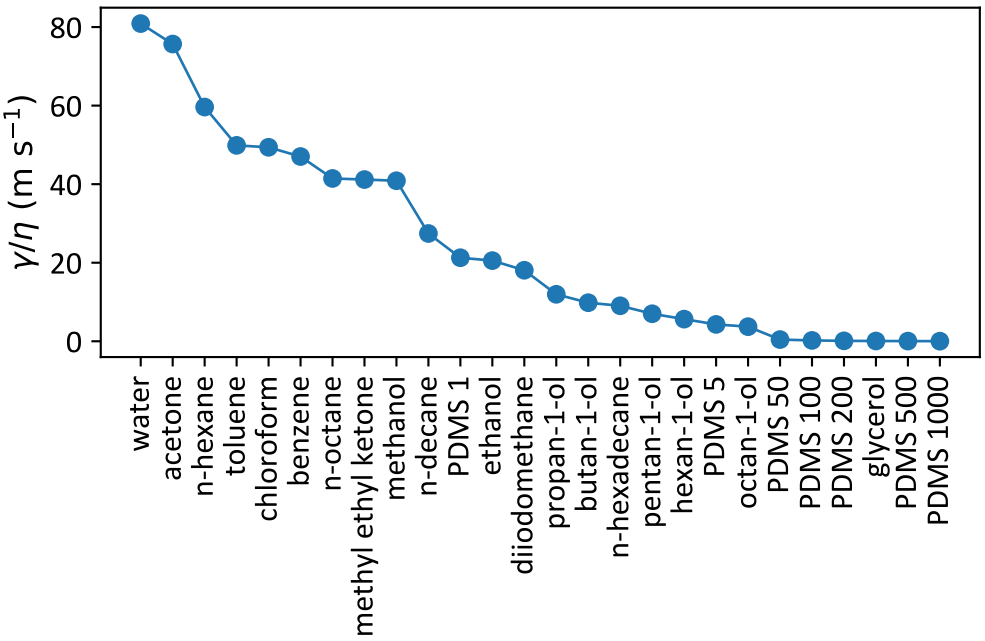

Figure 5.15: Ratio of surface tension, γ, to dynamic viscosity, η, for various liquids. PDMS x refers to PDMS oil with a viscosity of x cSt.

Figure 5.16 shows that the maximum capillary force is higher when liquids of higher surface tensions are used.[11] This observation is in agreement with equations 5.8 to 5.11, where the capillary force is proportional to surface tension.

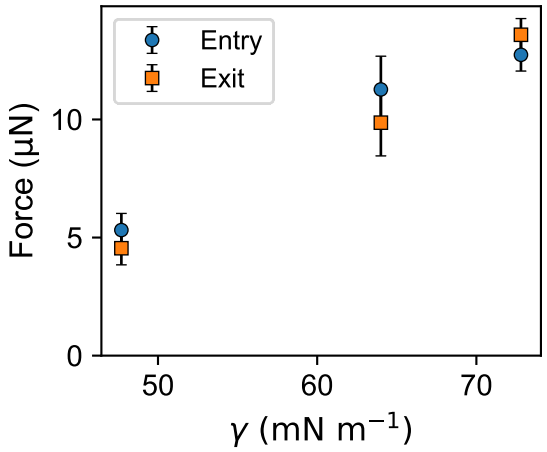

Figure 5.16: Entry and exit forces at 500 μm s^{-1}, measured for drops of diiodomethane ($\gamma = 50.8$ mN m^{-1}), a glycerol ($\gamma = 64.0$ mN m^{-1}) and pure water ($\gamma = 72.8$ mN m^{-1}). Note: for this plot, I have taken γ as the surface tensions of the pure liquids.

However, it is worth noting that although liquids having higher surface tensions are more likely to exert larger capillary forces on particles, this might not always

[11] Viscous force was negligible in these measurements. This can be deduced from the fact that the force required to push the drop alone was the same as the force required to push the drop with the particle submerged inside the drop.

be the case because the capillary force also depends on the advancing and receding contact angles. The contact angles also change when different liquids are used.

5.6.2 Viscous force

To determine when the viscous force becomes more significant than the capillary force, consider the following thought experiment. A surface that is contaminated with particles is pulled out of a liquid bath. Is there a greater chance of removing particles when the surface is pulled out quickly or slowly?

At low capillary numbers ($\mathrm{Ca} = \eta V/\gamma$), the capillary force is dominant. As the capillary number increases (for example, by increasing speed), the viscous force increases. An estimate for the ratio of the viscous force to the capillary force is obtained by dividing equation 5.7 by $2\pi R\gamma$:

$$\frac{F_\eta}{F_\gamma} \approx 5\frac{R}{H}\left(\frac{\eta v}{\gamma}\right), \tag{5.17}$$

where R is the radius of the particle, H is the thickness of the liquid meniscus, η is the dynamic viscosity of the liquid, v is the speed of the surface and γ is the surface tension of the liquid. For very low contact angles between the drop and the surface, H is small close to the three-phase contact line. When $H \approx R$, the viscous force becomes greater than the capillary force when $v > 0.2\gamma/\eta$. Therefore, with water, the viscous force only begins to dominate the capillary force above $\approx 15\,\mathrm{m\,s^{-1}}$. In contrast, with glycerol, the viscous force dominates above $\approx 1\,\mathrm{cm\,s^{-1}}$.

Based on the above reasoning, the higher the capillary number, the greater the viscous force and hence the greater the likelihood of removing a particle by viscous force. Note that this argument only applies if no liquid film is entrained on the surface.

Therefore, there is no general rule about whether it is more optimal to pull out the surface quickly or slowly. When the surface is pulled out of the liquid bath slowly, it is more likely that particles get removed by capillary force, whereas when the surface is pulled out quickly, it becomes more likely that particles get removed by viscous force.

Drops In the context of drops, the capillary number is not the only factor that determines whether the capillary or the viscous force is dominant. The contact angle between the drop and the flat surface is also important. To understand this, consider a glycerol drop and a water drop (both much smaller than the capillary length) on a hydrophobic surface. Due to the higher surface tension of water compared to glycerol, water drops generally have higher contact angles with hydrophobic surfaces than glycerol drops. Therefore, when water and glycerol drops of equal volumes are placed on the surface, the glycerol drop will have a smaller height.

Since $F_\eta \propto \eta/H$, where H is the height of the drop (equation 5.7), a glycerol drop exerts a larger viscous force than a water drop because (1) it has a higher viscosity, and (2) it has a smaller height due to a smaller contact angle. However, even with glycerol, the viscous force is still relatively insignificant. For example, a glycerol drop of height 400 µm moving at a velocity of 300 µm s^{-1} over a particle of radius 200 µm exerts a viscous force of the order of 1 µN, which is one order of magnitude lower than the rolling friction between the particle and the PDMS surface (≈ 10 µN, figure 5.8).

5.7 Different types of particles and surfaces

The experiments described so far involved spherical hydrophobic particles on a hydrophobic surface. However, there are many other possibilities. Dust particles are not always spherical but come in a variety of shapes and sizes. Furthermore, the particle, as well as the surface, do not necessarily have to be hydrophobic. All of these details will influence the likelihood of a drop successfully removing a particle from a surface.

In addition, when exposed to outdoor conditions, surfaces constantly change, at least on the microscopic level. Old dust particles get blown off by wind and new particles are deposited. In some cases, the surface can undergo physical and chemical degradation. These factors make it challenging to accurately predict whether water drops (e.g. from rain) can successfully remove particles from any given surface.

Here, I discuss how particle removal is influenced by different factors such as the particle type, the particle shape and the surface type.

5.7.1 Different particle geometry

Size Very small (nano) particles are more difficult to remove from PDMS surfaces because a larger fraction of their area gets embedded inside the PDMS. In equilibrium, the indentation depth between the particle and the flat surface is given by the Johnson-Kendall-Roberts (JKR) theory (equation 1.47):

$$d = \left(\frac{\sqrt{3}\pi w_{\text{adh}}}{2E^*}\right)^{\frac{2}{3}} R^{\frac{1}{3}}. \tag{5.18}$$

Here, w_{adh} is the work of adhesion and R is the radius of the particle. $1/E^* = (1-\nu_p^2)/E_p + (1-\nu_s^2)/E_s$, where ν_p and ν_s are the Poisson ratios of the particle and the PDMS surface, respectively, and E_p and E_s are their Young's moduli. Since $E_p \gg E_s$,[12] $E^* \approx E_s/(1-\nu_s^2)$. Therefore, the fraction of the particle that is embedded into the silicone surface is

[12]The Young's modulus of glass is of the order of 1×10^{10} Pa whereas that of the PDMS is of the order of 1×10^6 Pa.

$$\frac{d}{R} = \left(\frac{\sqrt{3}\pi w_{\text{adh}}(1-\nu_s^2)}{2E_s} \right)^{\frac{2}{3}} \frac{1}{R^{\frac{2}{3}}}. \tag{5.19}$$

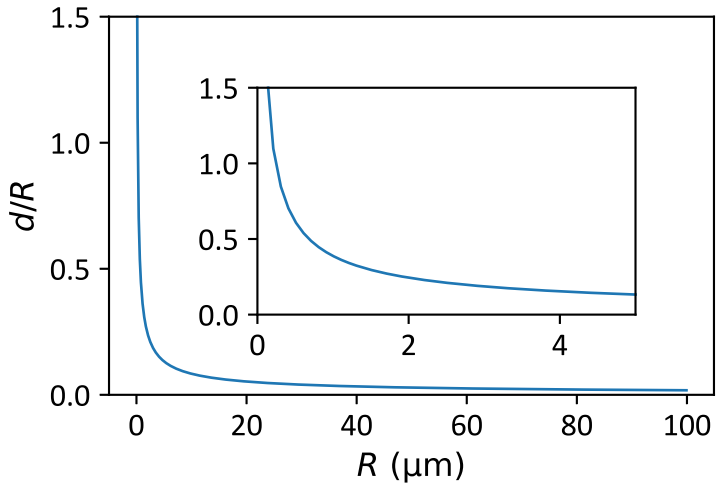

Figure 5.17: Fraction of particle that is embedded into the surface (equation 5.19). The following parameters were used: $E_s = 0.62\,\text{MPa}$, $w_{\text{adh}} = 71\,\text{mN}\,\text{m}^{-1}$ and $\nu_s = 0.5$. Values for w_{adh} and ν_s are from reference [99]. Note that the JKR theory is based on linear elastic theory and is only valid for small deformations. Therefore, the precise values of d/R at very small R may not be entirely accurate.

When a greater proportion of the particle is embedded, less of the particle can be in contact with a drop. Since the capillary force is proportional to the perimeter of the drop-air-particle contact line, the capillary force will be lower. Therefore, even though the JKR theory predicts that the adhesion between a particle and a surface decreases with the size of the particle, it is in fact more difficult for drops to remove very small particles from deformable surfaces. Leenaars [75] argued that liquid-air interfaces are in principle equally effective at removing particles, independent of their size. This argument breaks down for deformable surfaces.

Shape Although particles are commonly assumed to be spheres as a first approximation, most real contaminants are not completely spherical. Some have sharp edges, some consist of aggregates of many smaller particles, some take the shape of fibres/hairs and some are rather flat (e.g. sawdust or broken leaves).

Amongst all the possibilities, spherical particles are the most likely to roll. In contrast, flat particles are highly unlikely to roll and therefore can only be removed by sliding. Therefore, the capillary torque contribution to the resistive force (equation 5.6) is most likely not relevant for particles that are not round.

On the PDMS surfaces used throughout this chapter, flexible fibres (or hairs) were particularly difficult to remove using water drops for two reasons. Firstly, they get caught easily by pinning sites on the surface. Secondly, fibres are typically longer

than the drop diameter. This means that the capillary force only acts on a small part of the fibres, exerting a force that is usually insufficient to remove them.

5.7.2 Particles with different surface properties

The average contact angle between water and the particle was around 90° in the experiments presented in this section. Therefore, the maximum entry and exit forces were similar. However, if the average contact angle was not around 90°, the entry and exit forces would differ significantly. Below, I discuss two limiting cases.

Superhydrophobic particle A superhydrophobic particle has a high contact angle (around 160°) with water. A high contact angle corresponds to a high entry force and a low exit force. Therefore, superhydrophobic particles can most easily be removed by pushing (rather than pulling) them with water drops. However, we have seen that due to the convex shape of drops, particles tend to move along the circumference of the drop to reach the rear side. If superhydrophobic particles reach the rear side of the drop, they will easily detach since the pulling force is low for high contact angles. Therefore, to maximise the chance of removing superhydrophobic particles, large drops should be used such that the circumference of the drop is not significantly curved. Alternatively, an easier method would be to vertically dip the particle-contaminated surface into a water bath such that the water-air interface advances as a straight line on the surface.

Superhydrophilic particle A superhydrophilic particle has a low contact angle with water. A low contact angle corresponds to a low entry force and a high exit force. As a result, a superhydrophilic particle will enter the drop easily, but will strongly attach to the rear interface. For example, if the particle has a contact angle of 0° with the drop, the entry force will be zero, whereas the exit force will be $2\pi R\gamma$. Since the exit force is the crucial parameter determining whether the particle remains attached to the drop, it is easier to remove a hydrophilic particle than a hydrophobic particle, purely based on the maximum capillary force.

However, changing the surface properties of the particle also influences its adhesion to the surface. Depending on the specific system, the resistive force can either increase or decrease. To predict whether a change in the surface properties of the particle will increase or decrease the likelihood of particle removal, changes in both the capillary force and the resistive force have to be considered.

5.7.3 Surfaces with different hydrophobicities

So far, we have seen drop-particle collisions on a PDMS surface. PDMS has an average contact angle of around 90° with water. In general, surfaces have contact

angles that can significantly differ from 90°. Here, I discuss the influence of the hydrophilicity/hydrophobicity of the surface on particle removal.

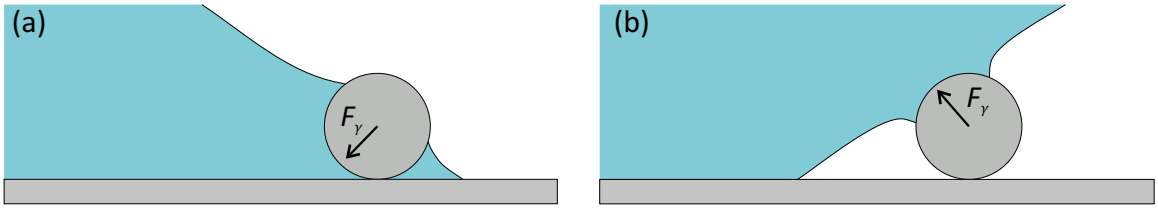

Figure 5.18: (a) On a hydrophilic surface, the capillary force pulls the particle towards the surface. (b) On a superhydrophobic surface, the capillary force pulls the particle away from the surface.

Hydrophilic surface Water forms a low contact angle ($< 90°$) with hydrophilic surfaces [figure 5.18 (a)]. Consequently, the capillary force pulls the particle towards the surface, effectively increasing the adhesion between the particle and the surface. An increase in adhesion results in an increase in friction and therefore reduces the likelihood of a successful particle removal.

Superhydrophobic surface In contrast, the contact angle of water on superhydrophobic surfaces is around 160°. Consequently, when the water-air interface makes contact with the particle, the capillary force acts upwards [figure 5.18 (b)], against the adhesion force between the particle and the surface. Therefore, high contact angles (significantly greater than 90°) promote particle detachment.

5.8 Enhancing particle removal

In section 5.3, we have seen that the forces that determine particle removal are the capillary force between the water drop and the particle and the friction force between the particle and the surface. A high capillary force favours attachment between the particle and the drop. In contrast, a high resistive force favours detachment of the particle from the drop.

Therefore, to enhance particle removal using water drops, we should either increase the capillary force or reduce the resistive force. Since particles generally move around the drop's circumference and end up at the rear side, the maximum capillary force at the rear side of the drop, F^{pull}, ultimately determines whether the particle is removed. Therefore, in this section, I will only discuss F^{pull} and not F^{push}. For simplicity, I will consider a sliding particle, but similar arguments also apply for a rolling particle.

5.8.1 Maximising the capillary force

For a particle of a given size, the maximum capillary force, $F_{\text{slide}}^{\text{pull}} = 2\pi R\gamma\cos^2(\Theta_{\text{R}}/2)$, can be increased by (1) choosing a liquid with higher surface tension, or (2) functionalising the particle such it becomes more hydrophilic (smaller Θ_{R}).

We do not usually have control over which types of particles adhere to surfaces, especially when they are exposed to the outdoors. However, we can usually choose which liquid to use to clean the surface. But varying the liquid does not change the maximum capillary force significantly because the surface tension of most liquids is more or less of the same order of magnitude (between 1×10^{-3} to $1 \times 10^{-2}\,\text{N}\,\text{m}^{-1}$). Therefore, there is not much scope to significantly enhance particle removal by only attempting to maximise the capillary force. It is much more effective to devise ways to reduce the resistive force between the particle and the surface.

5.8.2 Lowering the friction force

To set a particle in motion, the force applied to the particle must exceed the static friction force between the particle and the surface. Once the particle starts moving, the friction force typically drops to a lower value, termed the kinetic friction force. A particle can be removed if the capillary force exceeds the static friction force and the kinetic friction force.

Lubrication One method to reduce friction is by lubricating the surface. I tested this idea by lubricating PDMS surfaces with silicone oil (viscosity 10 cSt).

On lubricated surfaces, drops as well as particles are surrounded by wetting ridges. As a result, the shape of the water meniscus around the particle is different compared to its shape on a non-lubricated surface. When a particle is attached to the rear side of a water drop on a lubricated surface, the lubricant wetting ridge wraps around both the drop and the particle (figure 5.19). In this case, a water meniscus does not wrap around the lower part of the particle, as was the case on the non-lubricated surface [figure 5.6 (a)]. Instead, the particle is mostly surrounded by the lubricant.

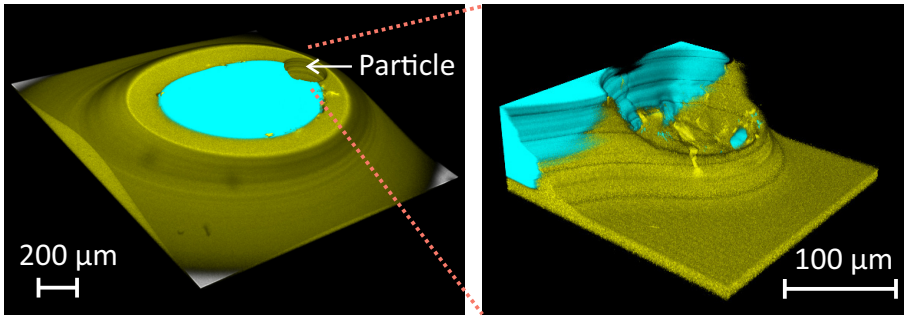

Figure 5.19: Wetting ridge around a particle (not dyed) attached to a water drop (cyan) on a lubricated (lubricant shown in yellow) surface.

A typical collision on a lubricated surface is shown in figure 5.20. The particle collided with the front side of the drop and moved around the circumference of the drop to reach the rear side, where it remained attached. Due to the low friction force between the particle and the lubricated surface, the drop barely deformed during the collision at $500\,\mu m\,s^{-1}$. In contrast, at this speed the particle entered and exited the drop on the non-lubricated surface (figure 5.10). On the lubricated surface, the force required to pull the particle at $500\,\mu m\,s^{-1}$ was around 10 times smaller than the force required to pull the particle at $50\,\mu m\,s^{-1}$ on the non-lubricated surface ($\approx 1\,\mu N$ compared to $\approx 10\,\mu N$).

Indeed, on the lubricated surface, the particle remained attached to the drop even at $2\,cm\,s^{-1}$, which is the highest speed that can be attained with the experimental setup.

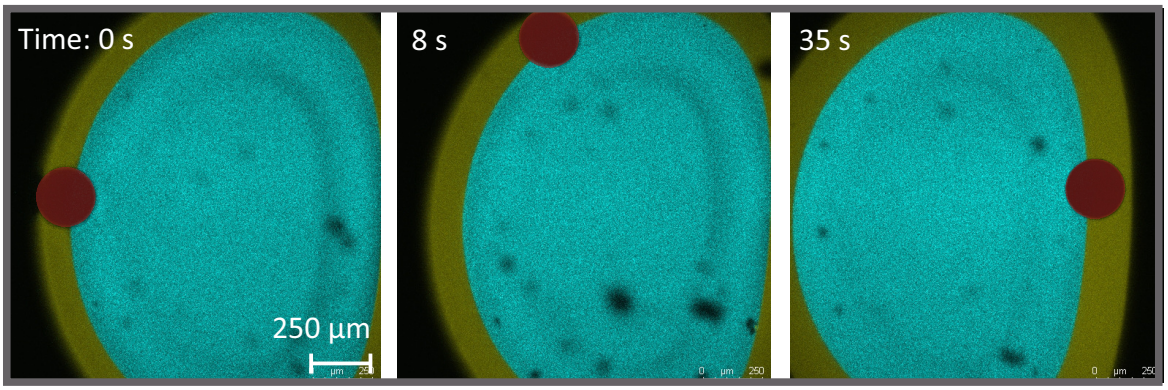

Figure 5.20: Collision between a drop (cyan) and a particle (drawn in red) on a lubricated (lubricant: 10 cSt silicone oil, yellow) surface at $500\,\mu m\,s^{-1}$.

Relevance to liquid-infused surfaces Liquid-infused surfaces (section 1.6.2.2) are hypothesised to be easy-to-clean. Since liquid-infused surfaces are essentially lubricated surfaces that are cleverly designed to retain the lubricant, they should have similar properties to the lubricated PDMS surface presented above. Therefore, the results presented above provide an experimental proof of the easy-to-clean nature of liquid-infused surfaces.

However, it turns out that liquid-infused surfaces are also more prone to accumulating contaminants. Since these surfaces are inherently 'wet', any dust particle that touches the surface sticks to it due to capillary force from the lubricant. On dry inclined surfaces, large dust particles usually do not stick strongly since the weight of the particle exceeds the adhesion force. However, on liquid-infused surfaces, the adhesion force is typically much greater due to capillary forces from the wetting ridge. This causes large dust to stick easily. Therefore, compared to dry surfaces, liquid-infused surfaces are more likely to get contaminated but are also easier to clean.

Superhydrophobic surfaces Another way to reduce the resistive force is to reduce the adhesion force between the particle and the surface, for example by using a superhydrophobic surface. Superhydrophobic surfaces typically have low adhesion with contaminant particles due to their favourable surface chemistry and their substantial degree of roughness which reduces the true contact area between the particles and the surface. These factors are responsible for their excellent self-cleaning property [49].

5.9 Summary

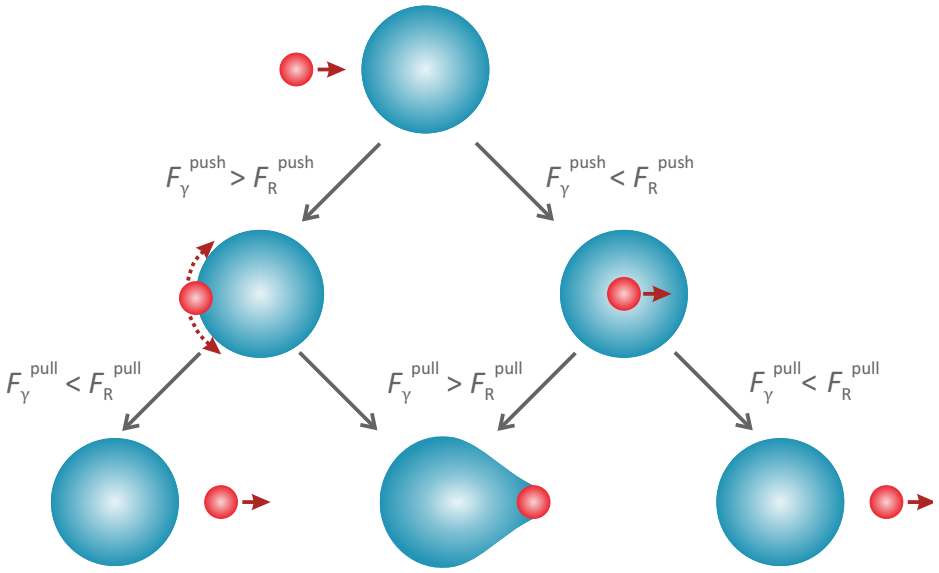

Figure 5.21: Summary of all possible outcomes when a particle collides with a water drop on a surface [80]. The schematic shows the collision (top view) between a particle (red) and a water drop on a surface. F_γ^{push} (F_γ^{pull}) is the maximum capillary force that the drop-air interface can exert on the particle when the latter is to the left (right) of the drop. $F_{\text{R}}^{\text{push}}$ ($F_{\text{R}}^{\text{pull}}$) is the resistive force acting on the particle when it is pushed (pulled) by the drop.

In this chapter, I used laser scanning confocal microscopy to (1) image collisions between water drops and single glass particles on silicone (unlubricated and lubricated) surfaces and (2) measure the force acting on the drop/particle during the collisions. When a particle collided with a drop, it either remained attached to the air-water interface (successful removal) or entered and exited the drop (unsuccessful removal). The capillary force between the particle and the interface was over two orders of magnitude larger than the viscous force acting on the particle due to the flow of liquid inside the drop. Therefore, the capillary force is the dominant force promoting particle removal.

Successful particle removal occurs when the capillary force exceeds the force required to displace the particle on the surface (against friction forces). Consequently,

particle removal can be enhanced by reducing the resistive force, for example by lubricating the surface or by coating it with a superhydrophobic layer.

Chapter 6

Conclusions and outlook

In this thesis, I devised two experimental methods. The first method enables us to measure forces dynamically using an inverted laser scanning confocal microscope (LSCM). The second method allows us to quantify changes in the surface tension of drops when they are placed in contact with surfaces. Furthermore, I derived theoretical models to study the rotation of particles at an interface. I showed that particles experience a resistive capillary torque when rotating at an interface and that the force required to detach a particle from an interface is reduced when the particle rotates during the detachment. Finally, I applied all the above experimental methods and theoretical results to study the collision between drops and particles on surfaces.

In this chapter, I summarise the methods and key results, and propose some future research avenues.

Forces with LSCM I showed how laser scanning confocal microscopy can be used to image microscopic processes dynamically and to measure horizontal forces at well-defined speeds. Forces are measured using a flexible metal blade that is clamped directly above the objective lens of the microscope. For example, when using this setup to the friction force between drops and surfaces, the drops is fixed by the blade while the surface moves at constant speed relative to the drop. When the drop presses against the blade, the blade deflects. The friction force is obtained by recording the deflection of the blade (with the microscope) and then using Hooke's law. This setup allows us to go beyond static imaging. In general, this setup can be used to study a variety of problems, where the combination of dynamic microscopic imaging and friction force measurements is desirable.

A foreseeable improvement is to adapt the setup such that force measurements and imaging can be performed simultaneously. Currently this is not the case because the objective lens can only focus on one horizontal plane, either on the blade or on the object that it is being pushed by the blade (e.g. a drop). Simultaneous force/imaging measurements can be performed in two ways: (1) a separate camera can be used to monitor the deflection of the blade, or (2) the objective lens can be made to periodically oscillate up and down such that in each oscillation, it focuses on

the blade and on the surface. Note that the second method will not strictly provide simultaneous measurements, but the measurements can nevertheless be regarded as simultaneous if the time period taken for each oscillation is much faster than the timescale of the physical process under investigation.

Surface pendant drop method The second experimental method that I designed is the surface pendant drop method, which I have used to quantify the surface tension of drops on PDMS surfaces. This method can be applied more generally to measure how the surface tension of drops change as they accumulate contaminants (e.g. particle, surfactants) from surfaces.

Water drops on PDMS I have shown that the time taken for drops to become cloaked on PDMS surfaces depends on the amount of lubricant in the PDMS matrix and on the viscosity of the lubricant. Cloaking took longer when there was less lubricant and when the lubricant was more viscous. These are the first measurements directly quantifying (1) the surface tension of a cloaked drop and (2) the kinetics of the change in surface tension during cloaking.

These findings are particularly relevant in the context of liquid-infused surfaces. One major drawback of these surfaces is that the lubricant gets depleted due to the cloaking of drops. So far, there is no solution to this problem for water drops on PDMS. However, if the lubricant viscosity and the concentration of lubricant in the texture are carefully chosen, such that the cloaking timescale exceeds the duration over which drops remain on the surface before being shed off, it might be possible to minimise the problem of lubricant depletion.

Particles rotating at an interface In general, particles either roll and/or slide when they are pulled on a solid surface by a drop-air interface. By developing a theoretical framework to model the effect of rotation on the capillary force, I showed that there are two main consequences of the particle rolling rather than sliding. First, particles experience a resistive torque when rotating at an interface. Second, the force required to detach a particle from an interface is reduced when the particle rotates. Both these effects are due to contact angle hysteresis between the liquid and the particle.

The resistive capillary torque experienced by rotating particles is relevant to the granular matter research community. It is well-known that the flow of granular matter (e.g. sand) is greatly reduced when the particles are moist. The reduced mobility has been attributed to several factors, but so far capillary torque has not been considered when modeling the flow of moist granular matter.

In future, the theoretical predictions for the capillary torque and the detachment force could be validated through experiments and computer simulations. Simulations

are particularly well-suited for this purpose since they offer the possibility to systematically investigate the influence of contact angle hysteresis on the capillary torque and the detachment force. Since the same equations apply to tiny as well as large particles, an experimental validation might also be possible using large particles which are relatively easier to handle.

Removal of particles from surfaces using drops In chapter 5, I used the experimental setup described above (Forces with LSCM) to image the collision between drops and particles on flat surfaces and to measure the force acting on the drop during the collision. I combined the experimental results with the theory that I derived on particles rotating at interfaces to study the mechanism by which drop remove particles from surfaces.

I showed that when water drops are used to remove particles from surfaces, the viscous force is negligible compared to capillary forces. Therefore, particles are removed by the air-water interface rather than by the flow of water inside the drop. In contrast to particle removal by bulk flows (where high speeds lead to increased removal), interfaces are more effective at removing particles when they move slowly. On flat surfaces, round particles are more likely to roll rather than slide since the coefficient of rolling friction is typically much lower than the coefficient of sliding friction. However, since a particle experiences a capillary torque when rolling at an interface, it can still experience a significant resistive force despite the low rolling friction between the particle and the surface.

In this work, I focussed on the collision between drops and single particles. The insights that this thesis provides will contribute towards a quantitative understanding of the more complex problem of how a drop removes multiple particles. The complexity of the problem is greatly increased when many particles are present, as demonstrated by a recent study by Geyer *et al.* (2020) [49] who investigated the opposite limit (very large number of particles). They showed that on a superhydrophobic surface, a water drop accumulates particles at its interface until it is completely covered, forming a so-called liquid marble. Their results imply that once there is complete coverage, there is no space for more particles and the cleaning efficiency is therefore greatly reduced.[1] Hence, it is important to ensure that self-cleaning surfaces do not get too heavily contaminated. In wet climates, this will likely not be a problem due to regular rainfall, fog, or dew. In dry climates, excessive contamination can be prevented by occasionally spaying water drops on the surface.

From a fundamental perspective, it would be interesting to investigate how the mechanism of particle removal evolves when the number of particles is successively increased. With only one particle, removal is only determined by the friction (and adhesion) between the particle and the surface, and by the capillary force between the

[1] In this case, larger drops are better due to their greater surface area.

drop and the particle. With two particles, the interaction between the particles also has to be considered. The presence of the second particle may influence the friction force experienced by the first particle, for example, if they rub against each other. As more particles are added, it becomes increasingly likely that the particles influence one another and the problem becomes a complex multi-body problem. Therefore, if we have an ideal surface contaminated with identical particles, the fact that a water drop can remove the first particle does not necessarily mean that it can also remove the second particle (and so on) because particle-particle interactions will have to be considered as well, and the particle-particle interactions will likely change each time an additional particle is introduced. Systematically studying this problem will also enable us to answer questions such as: How does a liquid marble form? What are the fundamental limits when using drops to clean surfaces?

Appendix A

Capillary force on rotating particles

A.1 Calculation of K factors

In this section, the K factor in equation 4.12 is calculated for two different functions describing the variation of the contact angle around a circular contact line.

A.1.1 Linear $\cos\Theta(\alpha)$

A linear variation of $\cos\Theta(\alpha)$ is described by the following equation:

$$\cos\Theta(\alpha) = \begin{cases} (\cos\Theta_{\mathrm{R}} - \cos\Theta_{\mathrm{A}})\frac{\alpha}{\pi} + \frac{1}{2}(\cos\Theta_{\mathrm{A}} + \cos\Theta_{\mathrm{R}}), & 0 < \alpha < \frac{\pi}{2} \\ -(\cos\Theta_{\mathrm{R}} - \cos\Theta_{\mathrm{A}})\frac{\alpha}{\pi} + \frac{1}{2}(3\cos\Theta_{\mathrm{R}} - \cos\Theta_{\mathrm{A}}), & \frac{\pi}{2} < \alpha < \frac{3\pi}{2} \\ (\cos\Theta_{\mathrm{R}} - \cos\Theta_{\mathrm{A}})\frac{\alpha}{\pi} + \frac{1}{2}(5\cos\Theta_{\mathrm{A}} - 3\cos\Theta_{\mathrm{R}}), & \frac{3\pi}{2} < \alpha < 2\pi. \end{cases} \tag{A.1}$$

Here, α is the azimuthal angle in the xy plane.

The expression for the magnitude of the capillary torque is (negative of equation 4.7):

$$M = \gamma R^2 \sin\phi \int_0^{2\pi} \cos\Theta(\alpha)\sin\alpha \; d\alpha \tag{A.2}$$

$$= \gamma R \frac{L}{2} \int_0^{2\pi} \cos\Theta(\alpha)\sin\alpha \; d\alpha, \tag{A.3}$$

where R is the radius of the particle and $L = 2R\sin\phi$ is the diameter of the contact line.

Substituting equation A.1 into equation A.3 leads to

$$
\begin{aligned}
&\frac{M}{\gamma R L} \\
&\quad = \frac{1}{2}\int_0^{\frac{\pi}{2}} \sin\alpha \left[(\cos\Theta_\mathrm{R} - \cos\Theta_\mathrm{A})\frac{\alpha}{\pi} + \frac{1}{2}(\cos\Theta_\mathrm{A} + \cos\Theta_\mathrm{R})\right] d\alpha \\
&\quad + \frac{1}{2}\int_{\frac{\pi}{2}}^{\frac{3\pi}{2}} \sin\alpha \left[-(\cos\Theta_\mathrm{R} - \cos\Theta_\mathrm{A})\frac{\alpha}{\pi} + \frac{1}{2}(3\cos\Theta_\mathrm{R} - \cos\Theta_\mathrm{A})\right] d\alpha \\
&\quad + \frac{1}{2}\int_{\frac{3\pi}{2}}^{2\pi} \sin\alpha \left[(\cos\Theta_\mathrm{R} - \cos\Theta_\mathrm{A})\frac{\alpha}{\pi} + \frac{1}{2}(5\cos\Theta_\mathrm{A} - 3\cos\Theta_\mathrm{R})\right] d\alpha \\
&\quad = \frac{\cos\Theta_\mathrm{R} - \cos\Theta_\mathrm{A}}{2\pi}\int_0^{\frac{\pi}{2}} \alpha\sin\alpha\ d\alpha + \frac{\cos\Theta_\mathrm{A} + \cos\Theta_\mathrm{R}}{4}\int_0^{\frac{\pi}{2}} \sin\alpha\ d\alpha \\
&\quad - \frac{\cos\Theta_\mathrm{R} - \cos\Theta_\mathrm{A}}{2\pi}\int_{\frac{\pi}{2}}^{\frac{3\pi}{2}} \alpha\sin\alpha\ d\alpha + \frac{3\cos\Theta_\mathrm{R} - \cos\Theta_\mathrm{A}}{4}\int_{\frac{\pi}{2}}^{\frac{3\pi}{2}} \sin\alpha\ d\alpha \\
&\quad + \frac{\cos\Theta_\mathrm{R} - \cos\Theta_\mathrm{A}}{2\pi}\int_{\frac{3\pi}{2}}^{2\pi} \alpha\sin\alpha\ d\alpha - \frac{5\cos\Theta_\mathrm{A} + 3\cos\Theta_\mathrm{R}}{4}\int_{\frac{3\pi}{2}}^{2\pi} \sin\alpha\ d\alpha \\
&\quad = +\left(\frac{\cos\Theta_\mathrm{R} - \cos\Theta_\mathrm{A}}{2\pi}\right)(1) + \left(\frac{\cos\Theta_\mathrm{A} + \cos\Theta_\mathrm{R}}{4}\right)(1) \\
&\quad - \left(\frac{\cos\Theta_\mathrm{R} - \cos\Theta_\mathrm{A}}{2\pi}\right)(0) + \left(\frac{3\cos\Theta_\mathrm{R} - \cos\Theta_\mathrm{A}}{4}\right)(0) \\
&\quad + \left(\frac{\cos\Theta_\mathrm{R} - \cos\Theta_\mathrm{A}}{2\pi}\right)(-2\pi + 1) + \left(\frac{5\cos\Theta_\mathrm{A} - 3\cos\Theta_\mathrm{R}}{4}\right)(-1) \\
&\quad = \cos\Theta_\mathrm{R}\left(+\frac{1}{2\pi} + \frac{1}{4} - 1 + \frac{1}{2\pi} + \frac{3}{4}\right) + \cos\Theta_\mathrm{A}\left(-\frac{1}{2\pi} + \frac{1}{4} + 1 - \frac{1}{2\pi} - \frac{5}{4}\right) \\
&\quad = \frac{1}{\pi}\left(\cos\Theta_\mathrm{R} - \cos\Theta_\mathrm{A}\right). \qquad \text{(A.4)}
\end{aligned}
$$

In the last step, the following result was used:

$$
\begin{aligned}
\int_a^b \alpha\sin\alpha\ d\alpha &= \int_a^b \alpha\frac{d(-\cos\alpha)}{d\alpha} && \text{(A.5)} \\
&= -\left[\alpha\cos\alpha\right]_a^b - \int_a^b (-\cos\alpha)\ d\alpha && \text{(A.6)} \\
&= -\left[\alpha\cos\alpha\right]_a^b + \left[\sin\alpha\right]_a^b. && \text{(A.7)}
\end{aligned}
$$

A.1.2 Cubic $\cos\Theta(\alpha)$

Using a cubic function to define the contact angle is the most realistic since it allows the contact angle to vary smoothly and continuously. The contact angle function has to satisfy four boundary conditions:

- $\cos\Theta(\alpha = -\pi/2) = \cos\Theta_{\mathrm{A}}$,
- $\cos\Theta(\alpha = \pi/2) = \cos\Theta_{\mathrm{R}}$,
- $\frac{d(\cos\Theta)}{d\alpha} = 0$ at $\alpha = -\pi/2$, and
- $\frac{d(\cos\Theta)}{d\alpha} = 0$ at $\alpha = \pi/2$.

The last two conditions are required in order to have a smooth contact angle variation. Since there are four boundary conditions, the function describing the contact angle variation must have four independent parameters. A cubic polynomial fulfils this requirement,

$$\cos\Theta(\alpha) = a\alpha^3 + b\alpha^2 + c\alpha + d, \tag{A.8}$$

where a, b, c, and d are independent variables. These variables can be written in terms of Θ_{A} and Θ_{R} using the four boundary conditions listed above to obtain:

$$a = \frac{2}{\pi^3}(\cos\Theta_{\mathrm{A}} - \cos\Theta_{\mathrm{R}}) \tag{A.9}$$

$$b = 0 \tag{A.10}$$

$$c = -\frac{3}{2\pi}(\cos\Theta_{\mathrm{A}} - \cos\Theta_{\mathrm{R}}) \tag{A.11}$$

$$d = \frac{1}{2}(\cos\Theta_{\mathrm{A}} + \cos\Theta_{\mathrm{R}}). \tag{A.12}$$

Therefore, the equation describing $\Theta(\alpha)$ is

$$\cos\Theta(\alpha) = \frac{2}{\pi^3}(\cos\Theta_{\mathrm{A}} - \cos\Theta_{\mathrm{R}})\alpha^3 - \frac{3}{2\pi}(\cos\Theta_{\mathrm{A}} - \cos\Theta_{\mathrm{R}})\alpha + \frac{1}{2}(\cos\Theta_{\mathrm{A}} + \cos\Theta_{\mathrm{R}}). \tag{A.13}$$

This equation is valid for $-\pi/2 < \alpha < \pi/2$.

To find the K factor corresponding to a cubic variation in $\cos\Theta(\alpha)$, the integral in equation A.3 is first rewritten such that the limits of integration match the range for which the definition of $\cos\Theta(\alpha)$ is valid ($-\pi/2$ to $\pi/2$),

$$\begin{aligned}\frac{M}{\gamma RL} &= \frac{1}{2}\int_0^{2\pi} \cos\Theta(\alpha)\sin\alpha \; d\alpha \\ &= \frac{1}{2}\int_{-\pi}^{\pi} \cos\Theta(\alpha)\sin\alpha \; d\alpha \\ &= \int_{-\frac{\pi}{2}}^{\frac{\pi}{2}} \cos\Theta(\alpha)\sin\alpha \; d\alpha \end{aligned} \tag{A.14}$$

The last step is because $\Theta(\alpha)$ is symmetric about the yz plane, and therefore the integrand has a periodicity of π.

Next, equation A.3 is substituted into equation A.14 to obtain

$$\begin{aligned}\frac{M}{\gamma RL} &= \int_{-\frac{\pi}{2}}^{\frac{\pi}{2}} \sin\alpha \left[a\alpha^3 + c\alpha + d\right]\ d\alpha \\ &= \left[\left(\frac{3\pi^2}{2} - 12\right)a + 2c + 0\right] \\ &= \frac{24}{\pi^3}(\cos\Theta_{\mathrm{R}} - \cos\Theta_{\mathrm{A}}). \end{aligned} \tag{A.15}$$

Therefore, the $K = 24/\pi^3$ for the cubic contact angle variation. In the above, the following results were used:

$$\begin{aligned}\int_{-\frac{\pi}{2}}^{\frac{\pi}{2}} \alpha\sin\alpha\ d\alpha &= \int_{-\frac{\pi}{2}}^{\frac{\pi}{2}} \alpha\frac{d(-\cos\alpha)}{d\alpha}\ d\alpha \\ &= \left[-\alpha\cos\alpha\right]_{-\frac{\pi}{2}}^{\frac{\pi}{2}} - - \int_{-\frac{\pi}{2}}^{\frac{\pi}{2}} \cos\alpha\ d\alpha \\ &= 2,\end{aligned}$$

and

$$\begin{aligned}\int_{-\frac{\pi}{2}}^{\frac{\pi}{2}} \alpha^3\sin\alpha\ d\alpha &= \int_{-\frac{\pi}{2}}^{\frac{\pi}{2}} \alpha^3\frac{d(-\cos\alpha)}{d\alpha}\ d\alpha \\ &= \left[-\alpha^3\cos\alpha\right]_{-\frac{\pi}{2}}^{\frac{\pi}{2}} - -3\int_{-\frac{\pi}{2}}^{\frac{\pi}{2}} \alpha^2\cos\alpha\ d\alpha \\ &= 3\int_{-\frac{\pi}{2}}^{\frac{\pi}{2}} \alpha^2\frac{d(\sin\alpha)}{d\alpha}\ d\alpha \\ &= 3\left[\alpha^2\sin\alpha\right]_{-\frac{\pi}{2}}^{\frac{\pi}{2}} - 3\int_{-\frac{\pi}{2}}^{\frac{\pi}{2}} 2\alpha\sin\alpha\ d\alpha \\ &= \frac{3\pi^2}{2} - 12.\end{aligned}$$

A.2 Detachment force

In this section, the detachment force (F^{pull}) predicted by Models 1, 2 and 4 are compared to the detachment force predicted by Model 3.

The percentage difference in the detachment force predicted by the models are calculated using

$$\frac{F_i - F_3}{(F_i + F_3)/2} \times 100, \tag{A.16}$$

where F_i $(i = 1, 2, 4)$ is the detachment force predicted by Model 1, 2 and 4 respectively. F_3 is the detachment force predicted by Model 3.

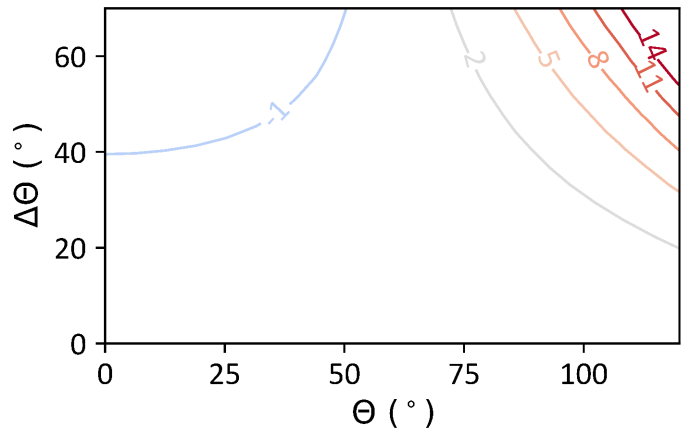

Figure A.1: Comparison between the detachment force predicted by Models 1 and 3. The curves are contours of contact percentage difference (calculated using A.16). The numbers on the contours are the percentage differences.

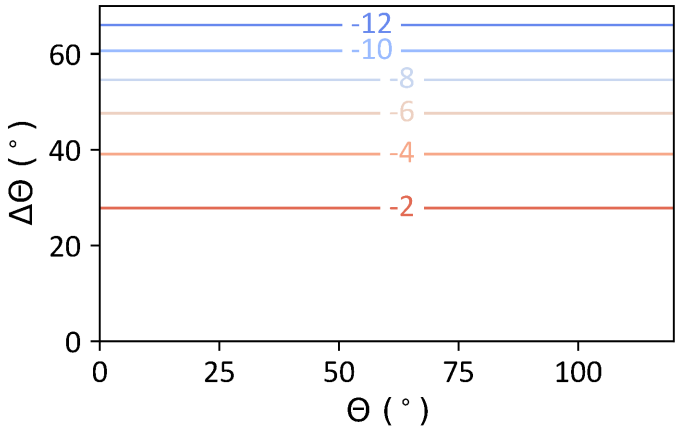

Figure A.2: Comparison between the detachment force predicted by Models 2 and 3. The curves are contours of contact percentage difference (calculated using A.16). The numbers on the contours are the percentage differences.

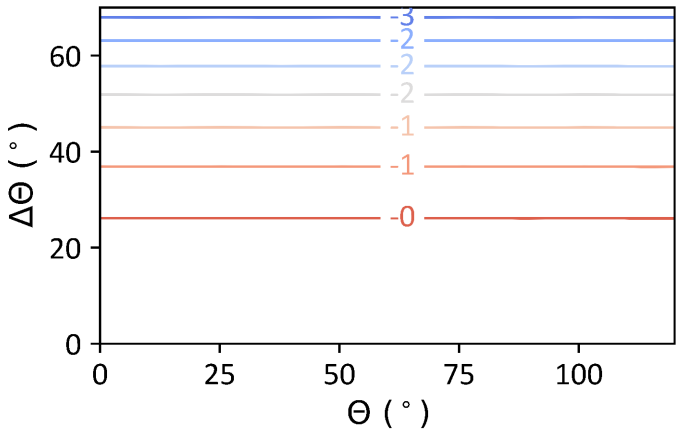

Figure A.3: Comparison between the detachment force predicted by Models 4 and 3. The curves are contours of contact percentage difference (calculated using A.16). The numbers on the contours are the percentage differences.

Appendix B

Particle removal by drops

B.1 Role of inertia

When a liquid-air interface, moving at speed v, collides with a stationary particle on a surface, the particle either remains attached to the interface or goes through it. For the particle to remain attached to the moving interface, its speed has to increase from 0 to v. This increase in speed corresponds to an increase in the kinetic energy of the particle by $(1/2)mv^2$, where m is the mass of the particle.

Here, I estimate the average force that the interface needs to exert on the particle to change its speed from 0 to v. I will call this force the inertial force, F_{inertial}.

The average force required to increase the speed of the particle from 0 to v over a distance δ is obtained by equating the work done to the initial kinetic energy of the particle. This gives

$$F_{\text{interial}} = \frac{1}{2\delta} m v^2. \tag{B.1}$$

To see how F_{inertial} compares to the maximum capillary force that the interface can exert on the particle, consider a glass particle (density $\rho = 2\,500\,\text{kg}\,\text{m}^{-3}$) of radius $100\,\mu\text{m}$ and mass $1 \times 10^{-8}\,\text{kg}$. The capillary force acting on a particle of radius R is of the order of $R\gamma$. By equating $R\gamma$ to F_{inertial}, we find that the speed at which F_{inertial} becomes comparable to the capillary force is

$$v \approx \frac{1}{R}\sqrt{\frac{3\gamma\delta}{2\pi\rho}} \approx 0.4\,\text{m}\,\text{s}^{-1}. \tag{B.2}$$

To obtain the numerical estimate, I have used $\delta \approx R$ and $\gamma = 72\,\text{mN}\,\text{m}^{-1}$ (for water).

The collision experiments presented in chapter 5 were performed at speeds that are at least two orders of magnitude smaller than $0.4\,\text{m}\,\text{s}^{-1}$. Therefore, inertial effects were negligible in the experiments.

References

[1] R. Ablett. XXV. an investigation of the angle of contact between paraffin wax and water. *Philos. Mag.*, 46(272):244–256, 1923. doi:10.1080/14786442308634243.

[2] Neil K. Adam and Gilbert Jessop. Angles of contact and polarity of solid surfaces. *J. Chem. Soc., Trans.*, 127(0):1863–1868, 1925. doi:10.1039/CT9252701863.

[3] Arthur W. Adamson and Alice P. Gast. *Physical Chemistry of Surfaces*. Wiley, 6 edition, 1997.

[4] Javed Ally, Michael Kappl, Hans-Jürgen Butt, and A. Amirfazli. Detachment force of particles from air-liquid interfaces of films and bubbles. *Langmuir*, 26(23):18135–18143, 2010. doi:10.1021/la103242e.

[5] W. B. Amos and J. G. White. How the confocal laser scanning microscope entered biological research. *Biol. Cell*, 95(6):335–342, 2003. doi:https://doi.org/10.1016/S0248-4900(03)00078-9.

[6] Surachet Aramrak, Markus Flury, and James B. Harsh. Detachment of deposited colloids by advancing and receding air–water interfaces. *Langmuir*, 27(16):9985–9993, 2011. doi:10.1021/la201840q.

[7] M. Barquins. Adherence and rolling kinetics of a rigid cylinder in contact with a natural rubber surface. *J. Adhes.*, 26(1):1–12, 1988. doi:10.1080/00218468808071271.

[8] F. E. Bartell and J. W. Shepard. The effect of surface roughness on apparent contact angles and on contact angle hysteresis. i. the system paraffin–water–air. *J. Phys. Chem.*, 57(2):211–215, 1953. doi:10.1021/j150503a017.

[9] F. E. Bartell and J. W. Shepard. Surface roughness as related to hysteresis of contact angles. II. the systems paraffin–3 molar calcium chloride solution–air and paraffin–glycerol–air. *J. Phys. Chem.*, 57(4):455–458, 1953. doi:10.1021/j150505a015.

[10] W. Barthlott and C. Neinhuis. Purity of the sacred lotus, or escape from contamination in biological surfaces. *Planta*, 202(1):1–8, 1997. doi:10.1007/s004250050096.

[11] Philipp Baumli, Maria D'Acunzi, Katharina I. Hegner, Abhinav Naga, William S. Y. Wong, Hans-Jürgen Butt, and Doris Vollmer. The challenge of lubricant-replenishment on lubricant-impregnated surfaces. *Adv. Colloid Interface Sci.*, 287:102329, 2021. doi:10.1016/j.cis.2020.102329.

[12] W. G. Beare, Frank Philip Bowden, and Thomas Martin Lowry. Physical properties of surfaces i - kinetic friction. *Philos. Trans. Royal. Soc. A*, 234(741):329–354, 1935. doi:10.1098/rsta.1935.0010.

[13] Joseph D. Berry, Michael J. Neeson, Raymond R. Dagastine, Derek Y. C. Chan, and Rico F. Tabor. Measurement of surface and interfacial tension using pendant drop tensiometry. *J. Colloid Interface Sci.*, 454:226–237, 2015. doi:10.1016/j.jcis.2015.05.012.

[14] Claire C. Berton-Carabin and Karin Schroën. Pickering emulsions for food applications: Background, trends, and challenges. *Annu. Rev. Food Sci. Technol.*, 6(1):263–297, 2015. doi:10.1146/annurev-food-081114-110822.

[15] J. Bico, J. Ashmore-Chakrabarty, G. H. McKinley, and H. A. Stone. Rolling stones: The motion of a sphere down an inclined plane coated with a thin liquid film. *Phys. Fluids*, 21(8):082103, 2009. doi:10.1063/1.3207884.

[16] T. D. Blake and J. M. Haynes. Kinetics of liquid/liquid displacement. *J. Colloid Interface Sci.*, 30(3):421–423, 1969. doi:10.1016/0021-9797(69)90411-1.

[17] Terence D. Blake. The physics of moving wetting lines. *J. Colloid Interface Sci.*, 299(1):1–13, 2006. doi:10.1016/j.jcis.2006.03.051.

[18] Ralf Blossey. Self-cleaning surfaces — virtual realities. *Nat. Mater.*, 2(5):301–306, 2003. doi:10.1038/nmat856.

[19] L. Bocquet, E. Charlaix, S. Ciliberto, and J. Crassous. Moisture-induced ageing in granular media and the kinetics of capillary condensation. *Nature*, 396(6713):735–737, 1998. doi:10.1038/25492.

[20] Giuseppe Boniello, Christophe Blanc, Denys Fedorenko, Mayssa Medfai, Nadia Ben Mbarek, Martin In, Michel Gross, Antonio Stocco, and Maurizio Nobili. Brownian diffusion of a partially wetted colloid. *Nat. Mater.*, 14(9):908–911, 2015. doi:10.1038/nmat4348.

[21] Edward Yu. Bormashenko. *Wetting of Real Surfaces*. De Gruyter, 2013.

[22] Robert Boyle. New experiments made and communicated by the honourable robert boyle esquire, about the superficial figures of fluids, especially of liquors contiguous to other liquors: likely to conduce much to the physical theory of the grand system of the world. *Philos. Trans. R. Soc.*, 11(131):775–787, 1676. doi:10.1098/rstl.1676.0050.

[23] Hans-Jürgen Butt, Rüdiger Berger, Werner Steffen, Doris Vollmer, and Stefan A. L. Weber. Adaptive wetting—adaptation in wetting. *Langmuir*, 34(38):11292–11304, 2018. doi:10.1021/acs.langmuir.8b01783.

[24] Hans-Jürgen Butt, Brunero Cappella, and Michael Kappl. Force measurements with the atomic force microscope: Technique, interpretation and applications. *Surf. Sci. Rep.*, 59(1):1–152, 2005. doi:10.1016/j.surfrep.2005.08.003.

[25] Hans-Jürgen Butt and Michael Kappl. Normal capillary forces. *Adv. Colloid Interface Sci.*, 146(1):48–60, 2009. doi:10.1016/j.cis.2008.10.002.

[26] Hans-Jürgen Butt and Michael Kappl. *Surface and Interfacial Forces*. Wiley-VCH, second edition, 2018.

[27] A. B. D. Cassie and S. Baxter. Wettability of porous surfaces. *Trans. Faraday Soc.*, 40:546–551, 1944. doi:10.1039/TF9444000546.

[28] T. T. Chau, W. J. Bruckard, P. T. L. Koh, and A. V. Nguyen. A review of factors that affect contact angle and implications for flotation practice. *Adv. Colloid Interface Sci.*, 150(2):106–115, 2009. doi:10.1016/j.cis.2009.07.003.

[29] Yves Chevalier and Marie-Alexandrine Bolzinger. Emulsions stabilized with solid nanoparticles: Pickering emulsions. *Colloids Surf. A*, 439:23–34, 2013. doi:10.1016/j.colsurfa.2013.02.054.

[30] R. G. Cox. The dynamics of the spreading of liquids on a solid surface. part 1. viscous flow. *J. Fluid Mech.*, 168:169–194, 1986. doi:10.1017/S0022112086000332.

[31] Dan Daniel, Jaakko V. I. Timonen, Ruoping Li, Seneca J. Velling, and Joanna Aizenberg. Oleoplaning droplets on lubricated surfaces. *Nat. Phys.*, 13(10):1020–1025, 2017. doi:10.1038/nphys4177.

[32] J. David Smith, Rajeev Dhiman, Sushant Anand, Ernesto Reza-Garduno, Robert E. Cohen, Gareth H. McKinley, and Kripa K. Varanasi. Droplet mobility on lubricant-impregnated surfaces. *Soft Matter*, 9(6):1772–1780, 2013. doi:10.1039/C2SM27032C.

[33] P. G. de Gennes. Wetting: statics and dynamics. *Rev. Mod. Phys.*, 57(3):827–863, 1985. doi:10.1103/RevModPhys.57.827.

[34] Robert H. Dettre and Rulon E. Johnson. Contact angle hysteresis. In *Contact Angle, Wettability, and Adhesion*, volume 43 of *Advances in Chemistry*, pages 136–144. American Chemical Society, 1964. URL: https://doi.org/10.1021/ba-1964-0043.ch008.

[35] Kilian Dietrich, Damian Renggli, Michele Zanini, Giovanni Volpe, Ivo Buttinoni, and Lucio Isa. Two-dimensional nature of the active brownian motion of catalytic microswimmers at solid and liquid interfaces. *New J. Phys.*, 19(6):065008, 2017. doi:10.1088/1367-2630/aa7126.

[36] P. Dimitrakopoulos and J. J. L. Higdon. On the gravitational displacement of three-dimensional fluid droplets from inclined solid surfaces. *J. Fluid Mech.*, 395:181–209, 1999. doi:10.1017/S0022112099005844.

[37] Athanase M. Dupré and Paul Dupré. *Théorie mécanique de la chaleur*. Gauthier-Villars, 1869. URL: http://archive.org/details/thoriemcaniqued00duprgoog.

[38] E. B. Dussan V. On the ability of drops or bubbles to stick to non-horizontal surfaces of solids. part 2. small drops or bubbles having contact angles of arbitrary size. *J. Fluid Mech.*, 151:1–20, 1985. doi:10.1017/S0022112085000842.

[39] Albert Einstein. Folgerungen aus den capillaritätserscheinungen. *Annalen der Physik*, 309(3):513–523, 1901. doi:https://doi.org/10.1002/andp.19013090306.

[40] A. I. ElSherbini and A. M. Jacobi. Liquid drops on vertical and inclined surfaces: I. an experimental study of drop geometry. *J. Colloid Interface Sci.*, 273(2):556–565, 2004. doi:10.1016/j.jcis.2003.12.067.

[41] A. I. ElSherbini and A. M. Jacobi. Retention forces and contact angles for critical liquid drops on non-horizontal surfaces. *J. Colloid Interface Sci.*, 299(2):841–849, 2006. doi:10.1016/j.jcis.2006.02.018.

[42] H. B. Eral, D. J. C. M. 't Mannetje, and J. M. Oh. Contact angle hysteresis: a review of fundamentals and applications. *Colloid Polym. Sci.*, 291(2):247–260, 2013. doi:10.1007/s00396-012-2796-6.

[43] C. W Extrand and A. N Gent. Retention of liquid drops by solid surfaces. *J. Colloid Interface Sci.*, 138(2):431–442, 1990. doi:10.1016/0021-9797(90)90225-D.

[44] Charles W. Extrand and Y. Kumagai. Liquid drops on an inclined plane: The relation between contact angles, drop shape, and retentive force. *J. Colloid Interface Sci.*, 170(2):515–521, 1995. doi:10.1006/jcis.1995.1130.

[45] Mahdi Farshchi-Tabrizi, Michael Kappl, Yajun Cheng, Jochen Gutmann, and Hans-Jürgen Butt. On the adhesion between fine particles and nanocontacts: an atomic force microscope study. *Langmuir*, 22(5):2171–2184, 2006. doi:10.1021/la052760z.

[46] Benjamin Franklin, William Brownrigg, and Farish. XLIV. of the stilling of waves by means of oil. extracted from sundry letters between benjamin franklin, LL. d. f. r. s. william brownrigg, m. d. f. r. s. and the reverend mr. farish. *Philos. Trans. R. Soc.*, 64:445–460, 1774. doi:10.1098/rstl.1774.0044.

[47] C. G. L. Furmidge. Studies at phase interfaces. i. the sliding of liquid drops on solid surfaces and a theory for spray retention. *J. Colloid Sci.*, 17(4):309–324, 1962. doi:10.1016/0095-8522(62)90011-9.

[48] Nan Gao, Florian Geyer, Dominik W. Pilat, Sanghyuk Wooh, Doris Vollmer, Hans-Jürgen Butt, and Rüdiger Berger. How drops start sliding over solid surfaces. *Nat. Phys.*, 14(2):191–196, 2018. doi:10.1038/nphys4305.

[49] Florian Geyer, Maria D'Acunzi, Azadeh Sharifi-Aghili, Alexander Saal, Nan Gao, Anke Kaltbeitzel, Tim-Frederik Sloot, Rüdiger Berger, Hans-Jürgen Butt, and Doris Vollmer. When and how self-cleaning of superhydrophobic surfaces works. *Sci. Adv.*, 6(3):eaaw9727, 2020. doi:10.1126/sciadv.aaw9727.

[50] J. W. Gibbs. *The collected works of J. Willard Gibbs. 1. Thermodynamics.* Longman and Green, 1928.

[51] A. J. Goldman, R. G. Cox, and H. Brenner. Slow viscous motion of a sphere parallel to a plane wall—II couette flow. *Chem. Eng. Sci.*, 22(4):653–660, 1967. doi:10.1016/0009-2509(67)80048-4.

[52] J. A. Greenwood, K. L. Johnson, S.-H. Choi, and M. K. Chaudhury. Investigation of adhesion hysteresis between rubber and glass using a pendulum. *J. Phys. D: Appl. Phys.*, 42(3):035301, 2008. doi:10.1088/0022-3727/42/3/035301.

[53] H. C. Hamaker. The london—van der waals attraction between spherical particles. *Physica*, 4(10):1058–1072, 1937. doi:10.1016/S0031-8914(37)80203-7.

[54] Francis Hauksbee. VIII. an experiment made at gresham-college, shewing that the seemingly spontaneous ascention of water in small tubes open at both ends is the same in vacuo as in the open air. *Philos. Trans. R. Soc.*, 25(305):2223–2224, 1706. doi:10.1098/rstl.1706.0008.

[55] Francis Hauksbee. II. several experiments touching the seeming spontaneous ascent of water. *Philos. Trans. R. Soc.*, 26(319):258–266, 1708. doi:10.1098/rstl.1708.0039.

[56] Francis Hauksbee. An account of an experiment touching the ascent of water between two glass planes, in an hyperbolick figure. *Philos. Trans. R. Soc.*, 27(336):539–540, 1712.

[57] Eugene Hecht. *Optics*. Pearson Education, fifth edition, 2017.

[58] Tabea Heckenthaler, Sumesh Sadhujan, Yakov Morgenstern, Prakash Natarajan, Muhammad Bashouti, and Yair Kaufman. Self-cleaning mechanism: Why nanotexture and hydrophobicity matter. *Langmuir*, 35(48):15526–15534, 2019. doi:10.1021/acs.langmuir.9b01874.

[59] Franziska Henrich, Daniela Fell, Dorota Truszkowska, Marcel Weirich, Manos Anyfantakis, Thi-Huong Nguyen, Manfred Wagner, Günter K. Auernhammer, and Hans-Jürgen Butt. Influence of surfactants in forced dynamic dewetting. *Soft Matter*, 12(37):7782–7791, 2016. doi:10.1039/C6SM00997B.

[60] S. Herminghaus. Dynamics of wet granular matter. *Adv. Phys.*, 54(3):221–261, 2005. doi:10.1080/00018730500167855.

[61] Robert Hooke. *An attempt for the explication of the phænomena observable in an experiment published by the Honourable Robert Boyle, Esq., in the XXXV experiment of his epistolical discourse touching the aire in confirmation of a former conjecture made by R.H.* 1661. URL: http://name.umdl.umich.edu/A44314.0001.001.

[62] William L. Hosch. Navier-stokes equation, 2020. URL: https://www.britannica.com/science/Navier-Stokes-equation.

[63] Aurélie Hourlier-Fargette, Arnaud Antkowiak, Antoine Chateauminois, and Sébastien Neukirch. Role of uncrosslinked chains in droplets dynamics on silicone elastomers. *Soft Matter*, 13(19):3484–3491, 2017. doi:10.1039/C7SM00447H.

[64] Aurélie Hourlier-Fargette, Julien Dervaux, Arnaud Antkowiak, and Sébastien Neukirch. Extraction of silicone uncrosslinked chains at

air–water–polydimethylsiloxane triple lines. *Langmuir*, 34(41):12244–12250, 2018. doi:10.1021/acs.langmuir.8b02128.

[65] Stefan Iglauer, Abdulsalam Salamah, Mohammad Sarmadivaleh, Keyu Liu, and Chi Phan. Contamination of silica surfaces: Impact on water–CO2–quartz and glass contact angle measurements. *Int. J. Greenh. Gas Control*, 22:325–328, 2014. doi:10.1016/j.ijggc.2014.01.006.

[66] Kenneth Langstreth Johnson, Kevin Kendall, A. D. Roberts, and David Tabor. Surface energy and the contact of elastic solids. *Proc. R. Soc. Lond. A.*, 324(1558):301–313, 1971. doi:10.1098/rspa.1971.0141.

[67] James Jurin. II. an account of some experiments shown before the royal society; with an enquiry into the cause of the ascent and suspension of water in capillary tubes. *Philos. Trans. R. Soc.*, 30(355):739–747, 1719. doi:10.1098/rstl.1717.0026.

[68] James Jurin. II. an account of some new experiments, relating to the action of glass tubes upon water and quicksilver. *Philos. Trans. R. Soc.*, 30(363):1083–1096, 1719. doi:10.1098/rstl.1717.0070.

[69] C. Korte and A. M. Jacobi. Condensate retention effects on the performance of plain-fin-and-tube heat exchangers: Retention data and modeling. *J. Heat Transfer*, 123(5):926–936, 2001. doi:10.1115/1.1391276.

[70] Michael J. Kreder, Dan Daniel, Adam Tetreault, Zhenle Cao, Baptiste Lemaire, Jaakko V. I. Timonen, and Joanna Aizenberg. Film dynamics and lubricant depletion by droplets moving on lubricated surfaces. *Phys. Rev. X*, 8(3):031053, 2018. doi:10.1103/PhysRevX.8.031053.

[71] A. Lafuma and D. Quéré. Slippery pre-suffused surfaces. *EPL*, 96(5):56001, 2011. doi:10.1209/0295-5075/96/56001.

[72] Dominique Langevin. *Emulsions, Microemulsions and Foams*. Soft and Biological Matter. Springer International Publishing, first edition, 2020. doi:10.1007/978-3-030-55681-5.

[73] Pierre Simon Laplace. *Traité de mécanique céleste*. L'Imprimerie de Crapelet : Chez J.B.M. Duprat, 1798. http://archive.org/details/traitdemcaniquec03lapl.

[74] L. T. Lee, E. K. Mann, D. Langevin, and B. Farnoux. Neutron reflectivity and ellipsometry studies of a polymer molecular layer spread on the water surface. *Langmuir*, 7(12):3076–3080, 1991. doi:10.1021/la00060a029.

[75] A.F.M. Leenaars and S.B.G. O'Brien. Particle removal from silicon substrates using surface tension forces. *Philips J. Res.*, (44):183–209, 1989.

[76] Richard Lucas. Ueber das zeitgesetz des kapillaren aufstiegs von flüssigkeiten. *Kolloid Z.*, 23(1):15–22, 1918. doi:10.1007/BF01461107.

[77] Jeffrey S. Marshall. Capillary torque on a rolling particle in the presence of a liquid film at small capillary numbers. *Chem. Eng. Sci.*, 108:87–93, 2014. doi:10.1016/j.ces.2014.01.003.

[78] James Clerk Maxwell. Capillary action, 1911. Encyclopedia Britannica. URL: https://en.wikisource.org/wiki/1911_Encyclop%C3%A6dia_Britannica/Capillary_Action.

[79] M. Minsky. Memoir on inventing the confocal scanning microscope. *Scanning*, 10(4):128–138, 1988. doi:https://doi.org/10.1002/sca.4950100403.

[80] Abhinav Naga, Anke Kaltbeitzel, William S. Y. Wong, Lukas Hauer, Hans-Jürgen Butt, and Doris Vollmer. How a water drop removes a particle from a hydrophobic surface. *Soft Matter*, 17(7):1746–1755, 2021. doi:10.1039/D0SM01925A.

[81] Akira Nakajima, Kazuhito Hashimoto, Toshiya Watanabe, Kennichi Takai, Goro Yamauchi, and Akira Fujishima. Transparent superhydrophobic thin films with self-cleaning properties. *Langmuir*, 16(17):7044–7047, 2000. doi:10.1021/la000155k.

[82] Jaap Noordmans, Poppo J. Wit, Henny C. Van Der Mei, and Henk J. Busscher. Detachment of polystyrene particles from collector surfaces by surface tension forces induced by air-bubble passage through a parallel plate flow chamber. *J. Adhes. Sci. Technol.*, 11(7):957–969, 1997. doi:10.1163/156856197X00525.

[83] Douglas A. Olsen, Powell A. Joyner, and Marvin D. Olson. The sliding of liquid drops on solid surfaces. *J. Phys. Chem.*, 66(5):883–886, 1962. doi:10.1021/j100811a029.

[84] F. M. Orr, L. E. Scriven, and A. P. Rivas. Pendular rings between solids: meniscus properties and capillary force. *J. Fluid Mech.*, 67(4):723–742, 1975. doi:10.1017/S0022112075000572.

[85] Ivan P. Parkin and Robert G. Palgrave. Self-cleaning coatings. *J. Mater. Chem.*, 15(17):1689–1695, 2005. doi:10.1039/B412803F.

[86] D. W. Pilat, P. Papadopoulos, D. Schäffel, D. Vollmer, R. Berger, and H.-J. Butt. Dynamic measurement of the force required to move a liquid drop on a solid surface. *Langmuir*, 28(49):16812–16820, 2012. doi:10.1021/la3041067.

[87] Olivier Pitois and Xavier Chateau. Small particle at a fluid interface: effect of contact angle hysteresis on force and work of detachment. *Langmuir*, 18(25):9751–9756, 2002. doi:10.1021/la020300p.

[88] Yves Pomeau and Emmanuel Villermaux. Two hundred years of capillarity research. *Phys. Today*, 59(3):39–44, 2006. doi:10.1063/1.2195314.

[89] Rayleigh. Surface tension. *Nature*, 43(1115):437–439, 1891. Note: This is a letter by Agnes Pockels but it was communicated by Lord Rayleigh. doi:10.1038/043437c0.

[90] Rayleigh. XXXVI. investigations in capillarity:—the size of drops.—the liberation of gas from supersaturated solutions.—colliding jets.—the tension of contaminated water-surfaces. *Philos. Mag.*, 48(293):321–337, 1899. doi:10.1080/14786449908621342.

[91] Wayne M. Saslow. A history of thermodynamics: The missing manual. *Entropy*, 22(1):77, 2020. doi:10.3390/e22010077.

[92] Philip H. Schade and Jeffrey S. Marshall. Capillary effects on a particle rolling on a plane surface in the presence of a thin liquid film. *Exp. Fluids*, 51(6):1645–1655, 2011. doi:10.1007/s00348-011-1179-y.

[93] Frank Schellenberger, Periklis Papadopoulos, Michael Kappl, Stefan A. L. Weber, Doris Vollmer, and Hans-Jürgen Butt. Detaching microparticles from a liquid surface. *Phys. Rev. Lett.*, 121(4):048002, 2018. doi:10.1103/PhysRevLett.121.048002.

[94] Frank Schellenberger, Jing Xie, Noemí Encinas, Alexandre Hardy, Markus Klapper, Periklis Papadopoulos, Hans-Jürgen Butt, and Doris Vollmer. Direct observation of drops on slippery lubricant-infused surfaces. *Soft Matter*, 11(38):7617–7626, 2015. doi:10.1039/C5SM01809A.

[95] A. D. Scheludko and D. Nikolov. Measurement of surface tension by pulling a sphere from a liquid. *Colloid Polym. Sci.*, 253(5):396–403, 1975. doi:10.1007/BF01382159.

[96] Hongquan She, David Malotky, and Manoj K. Chaudhury. Estimation of adhesion hysteresis at polymer/oxide interfaces using rolling contact mechanics. *Langmuir*, 14(11):3090–3100, 1998. doi:10.1021/la971061m.

[97] G. G. Stokes. X. on the effect of the internal friction of fluids on the motion of pendulums. In *Transactions of the Cambridge Philosophical Society*, volume 9 of *part ii*, pages 8–106. Cambridge Philosophical Society, 1851.

[98] Stefanie Strauch and Stephan Herminghaus. Wet granular matter: a truly complex fluid. *Soft Matter*, 8(32):8271–8280, 2012. doi:10.1039/C2SM25883H.

[99] Robert W. Style, Callen Hyland, Rostislav Boltyanskiy, John S. Wettlaufer, and Eric R. Dufresne. Surface tension and contact with soft elastic solids. *Nat. Commun.*, 4(1):2728, 2013. doi:10.1038/ncomms3728.

[100] Robert W. Style, Lucio Isa, and Eric R. Dufresne. Adsorption of soft particles at fluid interfaces. *Soft Matter*, 11(37):7412–7419, 2015. doi:10.1039/C5SM01743B.

[101] S P Sutera and R Skalak. The history of poiseuille's law. *Annu. Rev. Fluid Mech.*, 25(1):1–20, 1993. doi:10.1146/annurev.fl.25.010193.000245.

[102] Rafael Tadmor, Prashant Bahadur, Aisha Leh, Hartmann E. N'guessan, Rajiv Jaini, and Lan Dang. Measurement of lateral adhesion forces at the interface between a liquid drop and a substrate. *Phys. Rev. Lett.*, 103(26):266101, 2009. doi:10.1103/PhysRevLett.103.266101.

[103] Hannu Teisala, Philipp Baumli, Stefan A. L. Weber, Doris Vollmer, and Hans-Jürgen Butt. Grafting silicone at room temperature—a transparent, scratch-resistant nonstick molecular coating. *Langmuir*, 36(16):4416–4431, 2020. doi:10.1021/acs.langmuir.9b03223.

[104] O. V. Voinov. Hydrodynamics of wetting. *Fluid Dyn.*, 11(5):714–721, 1976. doi:10.1007/BF01012963.

[105] Edward W. Washburn. The dynamics of capillary flow. *Phys. Rev.*, 17(3):273–283, 1921. doi:10.1103/PhysRev.17.273.

[106] Robert N. Wenzel. Resistance of solid surfaces to wetting by water. *Ind. Eng. Chem.*, 28(8):988–994, 1936. doi:10.1021/ie50320a024.

[107] E. Wolfram and R. Faust. *Wetting, Spreading, and Adhesion*. Academic Press, 1978.

[108] Tak-Sing Wong, Sung Hoon Kang, Sindy K. Y. Tang, Elizabeth J. Smythe, Benjamin D. Hatton, Alison Grinthal, and Joanna Aizenberg. Bioinspired self-repairing slippery surfaces with pressure-stable omniphobicity. *Nature*, 477(7365):443–447, 2011. doi:10.1038/nature10447.

[109] William S. Y. Wong, Lukas Hauer, Abhinav Naga, Anke Kaltbeitzel, Philipp Baumli, Rüdiger Berger, Maria D'Acunzi, Doris Vollmer, and Hans-Jürgen Butt. Adaptive wetting of polydimethylsiloxane. *Langmuir*, 36(26):7236–7245, 2020. doi:10.1021/acs.langmuir.0c00538.

[110] Xudong Xiao and Linmao Qian. Investigation of humidity-dependent capillary force. *Langmuir*, 16(21):8153–8158, 2000. doi:10.1021/la000770o.

[111] Thomas Young. III. an essay on the cohesion of fluids. *Philos. Trans. Royal. Soc.*, 95:65–87, 1805. doi:10.1098/rstl.1805.0005.

Acknowledgements

This section has been removed in the electronic version of this thesis due to data protection laws.